UC Santa Cruz

UC Santa Cruz Electronic Theses and Dissertations

Title

Multiplexed Biosensors for Pathogen Detection

Permalink

https://escholarship.org/uc/item/5609z2rz

Author

Gopalakrishnan Meena, Gopikrishnan

Publication Date

2021

Peer reviewed|Thesis/dissertation

eScholarship.org Powered by the California Digital Library
University of California

UNIVERSITY OF CALIFORNIA
SANTA CRUZ

MULTIPLEXED BIOSENSORS FOR PATHOGEN DETECTION

A dissertation submitted in partial satisfaction
of the requirements for the degree of

DOCTOR OF PHILOSOPHY

in

ELECTRICAL AND COMPUTER ENGINEERING

by

Gopikrishnan Gopalakrishnan Meena

March 2021

The Dissertation of Gopikrishnan Gopalakrishnan Meena is approved:

Professor Holger Schmidt, Chair

Professor Marco Rolandi

Professor Ali Yanik

Quentin Williams
Interim Vice Provost and Dean of Graduate Studies

Copyright © by

Gopikrishnan Gopalakrishnan Meena

2021

Table of Content

1. Introduction----------1

2. Optical waveguides and ARROW waveguides----------7

   2.1 Symmetric slab waveguide----------7

   2.2 ARROW waveguides----------13

   2.3 Multi-Mode-Interference (MMI) waveguides----------15

   2.4 ARROW biosensor experimental setup----------20

   2.5 Optimization of ARROW waveguide performance----------21

3. Spectral multiplexing: 7x multiplexed detection of nucleic acid targets-------32

   3.1 Nucleic acid assay design----------34

   3.2 Single color tagged target identification----------35

   3.3 Multi color tagged target identification----------39

   3.4 Analysis of false signals----------40

   3.5 7x multiplexed detection----------42

4. Spatial multiplexing: Single molecule sensitive 3x multiplexed detection of antibiotic resistant bacterial plasmids----------46

   4.1 Spinning hollow disk for bacterial cell separation from blood---------48

   4.2 Monolith based microfluidic chip for target specific elution of antibiotic resistant plasmids----------50

   4.3 Spatial multiplexing with ARROW biosensor device----------53

   4.4 Detecting individual plasmids using ARROW biosensor chip---------54

   4.5 Simultaneous detection of all three antibiotic resistance plasmids--57

5. Multiplexed detection of SARS-CoV-2 RNA and antigen----------61

   5.1 Spatial-Spectral multiplexing using MMI waveguides----------63

   5.2 RNA and protein targets with bright fluorescence----------65

   5.3 Single molecule sensitive target detection and identification---------68

   5.4 Multiplexed amplification free detection of SARS-CoV-2 antigens and RNA----------71

6. Index guided liquid core waveguides for enhanced fluorescence detection-75

6.1 Device design----------77
6.2 Enhanced detection of fluorescent nanobeads----------82
6.3 Enhanced performance with buried ARROW chips----------84
7. Optofluidic sensor with integrated sample preparation----------90
7.1 Architecture of the PDMS chip and fabrication----------91
7.2 Single nucleic acid detection----------94
7.3 Dual detection of ZIKV nucleic acid and protein----------96
7.4 Differential target detection----------101
8. Conclusion----------105
9. Bibliography----------107

List of Figures

Fig 2.1 Cartoon of a symmetric slab waveguide and propagation of light in the ray model------7

Fig 2.2 Graphical solutions for eq 2.14 & 2.15----------10

Fig 2.3 a) Fundamental mode of a 5.2 μm thick slab waveguide with varying core refractive index. b) Vertical mode profile shows the penetration depth increasing when core refractive index almost matches with the cladding (n_1 = 1.45) ----------12

Fig 2.4 Schematic diagram of ARROW structure----------13

Fig 2.5 Schematic of a wide MMI waveguide that can support multiple modes----------16

Fig 2.6 a) Top down optical image of the ARROW biosensor chip. b) Zoomed in image of the optical setup with the biosensor chip coupled with fiber. c) Image of the complete experimental setup with the SC collection and excitation waveguide of the ARROW chip aligned to an APD and a power meter----------20

Fig 2.7 a) SEM cross section image of an ARROW rib waveguide. b) Mode image of the single mode waveguide. c) & d) Horizontal and vertical profile of the mode----------23

Fig 2.8 Top down fluorescent dye image of the pattern generated by an ARROW MMI waveguide in the LC waveguide----------24

Fig 2.9 a) SEM cross section image of a buried ARROW rib waveguide. b) Mode image of the waveguide excited with 556 nm wavelength. c) & d) Horizontal and vertical mode profile-----25

Fig 2.10 MMI pattern and normalized horizontal profile generated by a buried ARROW MMI waveguide----------26

Fig 2.11 a) top down field profile of the simulated MMI waveguide. b) & c) Cross-sectional field profile of the MMI waveguide output----------27

Fig 2.12 FWHM and p-v values of the MMI waveguide output for different lengths----------28

Fig 2.13 Mode image and profile of buried ARROW single mode waveguide with optimized rib height----------28

Fig 2.14 Color-coded fluorescence image of the MMI patterns and normalized horizontal intensity profile generated by an optimized buried ARROW waveguide----------29

Fig 2.15 a) SEM image of the SC-LC intersection of an ARROW biosensor. b) Optical mode position with respect to the substrate. c) Fluorescence signal from micro beads detected by ARROW waveguide with and without buried oxide layer----------30

Fig 3.1 a) Top down image of ARROW chip with MMI waveguide. b) MMI patterns generated when excited by 738 nm, 633 nm and 556 nm----------33

Fig 3.2 Sketch of the final bead-based assay with the captured target-probe complex---------35

Fig 3.3 a) E. coli detection. i) Fluorescence signal of beads with E. coli targets labeled with dark red fluorophores excited by MMI waveguide. ii) Zoomed-in signal of a single bead. iii) Bar histogram map of a correctly identified E. coli signal. b) and c) same analysis for IMP and E. aerogenes targets----------36

Fig 3.4 a) Signal from MMI waveguide excitation b) distance between adjacent spots of the pattern generated by the MMI waveguide----------37

Fig 3.5 Histogram of S(t)c values of all the detected signals from E. coli targets and b) & c) are from IMP and E. aerogenes targets----------38

Fig 3.6 A map of an E. coli target incorrectly identified as KPC because of dominant $S(t)_R$ value----------39

Fig 3.7 Intensity distribution mimicking an ideal signal produced from particle excited by MMI waveguide using 556 nm wavelength----------41

Fig 3.8 a) S(t) map of an ideal signals generated by the MMI waveguide. b) The same signals with background corrected to zeros----------42

Fig 3.9 Fluorescence signal from all seven targets flown together in the LC waveguide and excited by the three lasers simultaneously----------43

Fig 3.10 A fluorescence signal from E. coli target, below the set threshold----------44

Fig 4.1 a) Disk diffusion test: Antibiotic resistance is assessed by measuring the diffusion diameter till where the cell growth is inhibited [4]. b) Hodge test: Antibiotic resistant bacteria (1&3) allow template E.coli cells to grow closer to the antibiotic disk (Dark region corresponds to no cell growth) [5]----------47

Fig 4.2 a) Cartoon depicting the cross section of the sample separation hollow disk device showing the bowl region and the vestibule. The different steps the blood goes through when the disk is spun is shown. b) Top down photograph of the hollow disk with separated out plasma in the bowl----------50

Fig 4.3 a) Top down photograph of the microfluidic chip with monolith column. b) SEM image of the polymer monolith. c) Zoomed in image of the monolith showing its porosity. (Scales: 1cm, 500 µm, 5 µm respectively) ----------51

Fig 4.4 a) Cartoon depiction of the ARROW biosensor chip showing the interference pattern made by the MMI waveguide. b) Top down microscope image of the chip (inset: comparison with a US quarter). c) Fluorescence image of the excitation pattern of the MMI waveguide in the three LC waveguides----------53

Fig 4.5 a.i) Fluorescence signals from individual pUc19-KPC plasmids flown in Ch1. a.ii) Zooming into an event shows a signal with eleven peaks. a.iii) The S(t) map of a correctly identified KPC signal----------55

Fig 4.6 Fluorescence signal from negative controls----------56

Fig 4.7 Histogram of S(t) values of all the detected KPC events----------57

Fig 4.8 fluorescence signals from pUC19-KPC, pUC19-NDM, pUC19-VIM correctly identified----------58

Fig 4.9 Histogram distribution of the S(t)j values of all the events detected from fluorescence signal shown in fig 4.8. Events are deciphered as that of KPC, NDM or VIM based on which channel S(t) is most dominant (marked in red dashed box) ----------59

Fig 5.1 Cartoon of the SARS-CoV-2 virus [6] ----------61

Fig 5.2 a) Top down optical image of the ARROW biosensor b) Fluorescence image of the excitation pattern generated in LC1 (bottom) and LC2 (top) when excited by 556 nm and 633 nm respectively----------64

Fig 5.3 Target specific capture and fluorescent labeling of SARS-CoV-2 RNA----------65

Fig 5.4 Target specific capture of SARS-CoV-2 N protein and fluorescent tagging with bright reporter----------67

Fig 5.5 (ia) Fluorescence signal from RNA molecules tagged with nucleic acid staining dye. (ib) Zooming into an event shows a signal with eleven peaks. (ic) Autocorrelation of the signal has ten peaks which give the temporal information. (ii) Same examples from testing antigen reporters----------68

Fig 5.6 ia) Eleven peak mother wavelet function for identifying RNA signals. ib) Example of the CWT coefficients, C(u,s) from analyzing the RNA signal in Fig 5.5ib. Green dot represents the maximum value of the coefficient. ii) Same examples for analyzing antigen reporters----------71

Fig 5.7 Fluorescence signals when both antigen reporter and RNA molecules are flown through the chip with the MMI waveguide excited by both the lasers----------72

Fig 6.1 Fundamental mode electric field profile of a LC ARROW waveguide (Inset: ARROW boundary) ----------75

Fig 6.2 Schematic of the cross section of the SC and SC-LC intersections----------77

Fig 6.3 a) Simulation of fiber to SC waveguide coupling efficiency (Device geometry after fabrication is marked in red star). b) SEM image of SC waveguide cross section. c) Simulation of SC to LC waveguide coupling efficiency. d) SEM image of SC-LC intersection----------78

Fig 6.4 Refractive index of ZnI2 varying with concentration (data used from [14]) ----------79

Fig 6.5 a) Simulated mode images of LC waveguide with H2O and ZnI2 (Scale: 5 µm). b) Mode images of the same (Scale: 10 µm) ----------79

Fig 6.6 Transmission measurement along the LC waveguide----------80

Fig 6.7 Horizontal mode profile of the LC fundamental mode for varying core refractive index----------81

Fig 6.8 LC fundamental mode spread factor and confinement factor----------81

Fig 6.9 a) Fluorescence signal from individual nanobeads. b) Distribution of the bead signals from a 100 sec long fluorescence trace----------82

Fig 6.10 Serial dilution of the nanobeads and measured particle counts per unit volume. The black dashed line shows the expected particle counts per unit volume----------83

Fig 6.11 a) Cartoon of buried ARROW SC-LC cross section. b) Simulated mode image of the fundamental mode of buried ARROW LC channel----------84

Fig 6.12 Transmission measurement along the LC waveguide for an ARROW biosensor-----85

Fig 6.13 a) Fluorescence signal from individual nanobeads tested in ARROW chip. b) Distribution of the bead signals from a 100 sec long fluorescence trace----------86

Fig 6.14 a) Signal from a nanobead when excited with an MMI waveguide when the ARROW LC waveguide is filled with water (Blue) and ZnI2 salt (Red). b) Autocorrelation of these signals----------87

Fig 7.1 Top down microscope image of the PDMS chip. The waveguide is excited with a red He-Ne laser and the pneumatic valves are filled with green food dye----------91

Fig 7.2 Schematic of the fabrication process of the PDMS chip----------93

Fig 7.3 Top down optical image (left) and profilometric image (right) of the waveguide (top) and pneumatic layer (bottom) ----------93

Fig 7.4 a) Schematic of the all in one PDMS chip. b) Cross section schematic of the pneumatic valves. c) Image of the optical modes supported by the SC PDMS waveguide when excited by 633 nm and 556 nm wavelengths (Scale bar: 7 µm) ----------94

Fig 7.5 Fluorescence signal trace demonstrating detection of individual λ-DNA. First few minutes is used for tagging and incubating the DNA and then pumped to the detection part. The inset shows zoomed in, signals from individual λ-DNAs----------95

Fig 7.6 Dilution curve of the detected λ-DNA. For each know concentration of the sample, the detected number of events per unit volume is plotted----------96

Fig 7.7 Schematic for preparation of magnetic bead-based assay. (I) Targets (nucleic acids and proteins) are introduced in Inlet 1 and the reagents such as the magnetic beads with capture probe and the fluorescent probes in inlet-2. (II) Analytes are mixed and incubated in valve “no 3”. (III) After wash steps, tagged targets are pumped for optical detection----------97

Fig 7.8 Schematic view of the optical set up for dual target detection. A dichroic mirror spectrally differentiates the signals from the nucleic acids and proteins and are couple to two APDs. The excitation light is blocked by optical filter kept in front of the APDs----------99

Fig 7.9 Fluorescence signal from magnetic beads with ZIKV nucleic acids (pink) and proteins (green) detected by the two APDs. Inset: Zoomed in 2 sec trace shows individual peaks above the set threshold. The protein signal trace had a higher noise threshold (shown in the inset as black dotted line) than the nucleic acid signals----------100

Fig 7.10 Fluorescence trace from the chip when using non-zika specific nucleic and protein targets in serum. The experiment yielded no signal indicating good specificity of the assay. The green excitation generally gave higher background than the red----------100

Fig 7.11 Distribution of signals from ZIKV specific nucleic acid (top) and protein (bottom) assays in human serum. Experiments for nucleic acids were done with 2 µM and 0.02 µM starting concentration and 600 µg/mL and 6 µg/mL for proteins----------101

Fig 7.12 Target signal map for differential detection of Zika. The bar plots indicate the number of nucleic acid and protein signals for each target compared to that from zika specific targets----------102

List of Tables

Table 3.1 Assigned color combinations for each antibiotic resistant target----------34

Table 3.2 Sequences of capture probe and fluorescence probe used for each antibiotic resistant target----------34

Table 3.3 The percentage of false signals from each target----------40

Table 4.1 KPC, NDM and VIM mutations transcribed in pUC19 plasmids and the corresponding capture sequences----------52

Abstract

Multiplexed biosensor for pathogen detection

by

Gopikrishnan Gopalakrishnan Meena

Efficiently combating infectious diseases is a vital part of primary health care. The first step taken towards treating diseases is detection and identification. Disease detection has evolved to become an essential unit in both hospitals, clinical labs and now even at the point of care, to help physicians make well informed diagnosis and treatment in a timely manner. For quick response to an infection, all of these health care sectors need diagnostic tools which are sensitive enough to detect pathogens at an early stage. Integrating them with sample preparation units expedites the diagnostics process through automation, removing human errors and minimal use of clinical samples. Adding multiplexed detection capabilities to these systems makes diagnosis faster through parallel processing. It also helps obtain more information of the disease by simultaneously probing for different characteristics of the pathogen such as the type of species, mutations or even cross reactivity with other targets. Optofluidics has emerged as one of the most desired technology to incorporate all of this. This thesis focuses on several multiplexed biosensing techniques using optofluidic biosensor chips that have planar solid core (SC) and liquid core (LC) waveguides and their combination with integrated sample preparation units. Platforms using both silicon based anti-resonant-reflecting-optical-waveguide (ARROW) systems and polydimethylsiloxane (PDMS) based optical waveguide systems are described.

Multiplexed detection is executed in the ARROW biosensor platform using multi-mode-interference (MMI) waveguides which create wavelength dependent excitation patterns in the liquid core ARROW enabling fluorescence based multiplexed detection of biomolecules. The thesis describes how the signal-to-noise ratio of the ARROW biosensors is improved more than

30x using a buried oxide layer and how the design of the MMI waveguides is optimized for the buried waveguides to generate better excitation profiles for the desired spectrum, extending from 488 nm to 738 nm. The improved ARROW platform is used to demonstrate 7x multiplexed detection of an antibiotic resistant bacterial panel by combining spectral multiplexing with a three-color combinatorial labeling scheme. The ARROW biosensor platform is also used to demonstrate for the first time, simultaneous amplification-free detection of three antibiotic resistant nucleic acid biomarkers (bacterial plasmids) with single molecule sensitivity using spatial multiplexing. Finally, pertaining to the COVID-19 pandemic which started in the year 2020, spectral and spatial multiplexing techniques are combined to demonstrate the first dual detection of SARS-CoV-2 RNA and protein targets, both with single molecule sensitivity. Also presented is a novel SiO_2 based biosensor with index guided SC and LC waveguides. The optical mode of the LC waveguide is guided and tuned by using high refractive index ZnI_2 salt solution for greatly enhanced fluorescence detection. This enables sensing nanobeads with an ultra-low limit of detection down to clinically relevant attomolar range. The thesis concludes with a report on a PDMS based sensor integrating monolithically both a sample preparation unit and sensing system. The device has pneumatically activated microvalves, which is used to capture, filter and tag Zika virus specific nucleic acid and protein targets. These are detected simultaneously in the same chip using PDMS based optical waveguides for differential detection of ZIKA virus from other cross reacting species such as Dengue.

Acknowledgement

I thank my advisor Prof. Holger Schmidt for his patience and mentorship. I am very grateful for all the sincere and hard work he has put towards supporting my graduate studies, molding and developing me as good respectful student and researcher, preparing me to tackle other challenges in the next stage of my career. Collaborations are eminent for a successful research work. I thank Prof. Aaron Hawkins and his group for the fruitful discussions and tirelessly fabricating the biosensors which made my research work possible. I also acknowledge the support and feedback from my committee members Prof. Ali Yanik and Prof. Marco Rolandi.

I thank my parents and my brother for their love and continuous support. I treasure the emotional strength they give me every day. I express my gratitude to all my lab mates and friends at Santa Cruz with whom I have shared jokes, dinners and for their help in my research work. The quality time they shared with me are memorable and always made me happy. I am in debt to the climbing gym at Santa Cruz for opening a new world and community for me, where I met many great people. I also thank the bus drivers at Santa Cruz Metro for all their care and concern through out the past six years. I am excited about the new friends I continue to make in this wonderful town.

1 Introduction

Disease diagnostics is a very important first line of step needed to deliver targeted and precise medical treatments to patients. Over the past 50 years a tremendous improvement in medical technology has been achieved especially in the developed nations to help diagnose life threatening pathogens. Unfortunately, most of these techniques are very expensive, time consuming and resource hungry. Thus, health care is readily available only to people who can afford and have easy access to it. This hampers the effort to build a world with public health for all [1]. So, it is very important to develop economical point-of-care medical diagnostic tools to make health care accessible to all [2]. Moreover, in the last few decades we have seen several diseases out breaks across the world where pathogens quickly evolve to become resilient against the drugs used to fight them [3-5]. Physicians need to make quick and well-informed decisions to combat such pathogens in its early stage, before it spreads. New diagnostic tools should be built to be sensitive, precise and faster than traditional medical procedures to serve this purpose [6]. Several of these microorganisms, for example Zika and Dengue virus have comparable biological traits and cause diseases with very similar symptoms [7]. Many of them can evolve to have multiple mutations which give them resistance to the medicine, such as drug resistant bacteria [8]. All these characteristics of a pathogen also need to be considered to get a successful and confident differential diagnosis. Thus, multiplexed analysis is an essential capability that has to be addressed while developing a diagnostic system [9].

Aimed towards solving these problems, a major push in biomedical research has been towards developing chip scale biosensors [10]. These devices mainly probe biomolecules using optical waveguide systems for sensitive detection of biomolecules [11]. Easy integration with advanced silicon microfabrication techniques has made silicon photonics the most popular choice to build such sensors. Photonic chips typically employ ring resonators, Mach Zehnder interferometers or photonic crystals to directly interact with biomolecules which trigger a sensitive shift in the resonance frequency [12]. Apart from resonance-based detection,

fluorescence-based detection is also a common technique for biosensing with photonic chips. In this case the biomolecule is labeled with a fluorophore and is excited by shining light using optical waveguides. The fluorescence signal from the target is detected using a photodetector. Huge progress has been made in biotechnology on efficient labeling probes such as nano -strings, -barcodes, -quantum dots and -beads [13,14]. Ultra-sensitive diagnostic systems can be built by merging these tools with photonic chip sensors. Since the fluorophores respond in the visible spectrum of light, dielectric materials such as oxides (SiO_2, Ta_2O_5) or nitrides (Si_3N_4) are used for fabricating fluorescence based photonic biosensors. These dielectrics have much lower absorption in the visible spectrum compared to silicon. TiO_2 based photonic crystals and SiO_2 based ring resonators are a few examples of biosensors that have demonstrated enhanced detection of fluorescent probes such as molecular beacons and quantum dots [15, 16].

Medical diagnostics requires careful preparation of complex bio assays which is usually done in a clinical laboratory by a trained professional. Microfluidics is the most promising technology that can precisely handle fluids of low volume and circumvent the need for a laboratory setting and specialized technicians for sample preparation. Droplet fluidics [17], paper-based microfluidics [18], lab-on-a-disk devices [19], pneumatically actuated micro pumps [20] are the most common designs. They are used for doing careful on chip sample preparation steps such as reagent mixing, sample sorting & filtering, target amplification, thermal annealing and trapping. These techniques, especially the microvalve automata pumps have been demonstrated to be an important tool because of their ease of fabrication, wide range of fluidic handling and programable nature.

Optofluidic devices combines these two major innovations, optical waveguides and microfluidics, to help develop diagnostic platforms with increased system level integration [21, 22]. Anti-resonant-optical-waveguides (ARROWs) based biosensors are one of the most prominent optofluidic biosensor [23]. These are SiO_2 based waveguides, fabricated on a Si

substrate having alternating layers of Al_2O_3 and Ta_2O_5 thin films. The dielectric thin films are designed to act as an anti-resonant reflector, preventing leakage of light into the Si substrate. Thus, an ARROW waveguide allows for guiding light even in liquid core channels filled with low refractive index aqueous solutions. Biosensors built using ARROW waveguides use solid-core (SC) waveguides to excite and collect signals from fluorescently tagged particles flowed through an orthogonally intersecting liquid-core (LC) waveguide. These biosensors are sensitive enough to detect single nucleic acids and have been used to demonstrate detection of viral pathogens with an analytic limit of detection (LOD) in the attomolar range [24,25]. This system also has multi-mode-interference (MMI) excitation waveguides to incorporate multiplexing capabilities. The MMI waveguides generate wavelength dependent well-defined multi-spot excitation patterns in the LC waveguide. The fluorescence signal from excited targets which flow past the MMI patterns has the target information encoded. In previous works, MMI waveguides in the ARROW platform have been used to demonstrate simultaneous detection of three different influenza virus particles using spectral multiplexing [26] and six different virus particles using spatially dependent discrimination of signals [27]. This system has also been used to demonstrate velocity-based multiplexing [28]. These sensors have also been merged with arrays of programable polydimethylsiloxane (PDMS) based micro valves via hybrid integration [29]. The PDMS micro valves have been used for filtering, target specific capture, enrichment and fluorescent tagging of nucleic acids, thus integrating a sample preparation unit with the ARROW biosensor chip.

This thesis describes four major research contributions that further push the capabilities of the above mentioned optofluidic devices. The projects are focused on reaching closer to the goal of a fully functional biosensor platform for successful detection of antibiotic resistant bacterial panels and differential diagnostics of Zika and Dengue. Both of these pathogens are very relevant to the major disease outbreaks that have taken place in the past two decades [4, 30]. Chapter two will cover the basic function of an optical waveguide. First the principle of an optical

slab waveguide where guiding of light is through total internal reflection is described. A detailed description of the design of the ARROW waveguides and MMI waveguides follows. The experimental setup used to test the biosensor devices and demonstrate the detection of pathogens is described next. The chapter ends with a description of the optimization work done on the optical waveguides to build better performing single mode and MMI waveguides. Chapter three covers the work done to demonstrate the full spectral multiplexing power of MMI waveguides to distinguish 2^{M-1} targets using M excitation wavelengths. The chapter describes simultaneous detection of nucleic acids representing seven antibiotic resistant bacterial targets (three bacterial species: E. coli, E. aerogenes, K. pneumonia and four antibiotic resistance genes: VIM, NDM, KPC and IMP) with a single LC channel by combinatorially labeling the targets with three colors. Chapter four shows how sensing using MMI waveguides can be extended to amplification free, multiplexed detection of individual bacterial nucleic acids. Brief descriptions of a disk-based and polymer monolith-based sample processing devices are given which enables target specific elution of bacterial plasmids from E. coli cells spiked in whole human blood. Three different antibiotic resistant plasmids KPC, VIM and NDM are simultaneously detected with single molecule sensitivity via spatial multiplexing using the MMI waveguides. This thesis was prepared during the year 2020 when the COVID-19 outbreak started. Chapter five describes the pros and cons of the current diagnostic techniques targeting SARS-CoV-2 and the reason to develop a system capable of dual nucleic acid protein detection. The chapter describes how the ARROW biosensor platform could be a solution for this by demonstrating multiplexed amplification free detection of SARS-CoV-2 RNA and protein molecules with single molecule sensitivity. Chapter six covers work done to improve the optical performance of the biosensor by introducing a new optofluidic platform which uses LC waveguides with high index ZnI_2 salt solution as core. The chapter describes how the device geometry and LC refractive index is optimized to get high sensitivity. An eight times enhancement of signal-to-noise-ratio (SNR) and 45x increase in detection efficiency and a 100x lower LOD is achieved through this. Finally, chapter seven covers design and

implementation of an all-PDMS optofluidic platform which combines on a single chip, sample processing with in-flow optical detection of biomolecules. This device is used for fluorescent labeling of λ-DNA, immediately followed by optical detection with single molecule sensitivity. Furthermore, sample preparation of more complex analytes corresponding to Zika nucleic acids and proteins is demonstrated, followed by simultaneous optical detection of the analytes. This technique of dual assay detection is used for differential detection of Zika from structural similar flavivirus like Dengue.

2 Optical waveguides and ARROW waveguides

2.1 Symmetric slab waveguides

A slab waveguide is one of the simplest optical waveguides which guides light through total internal reflection [31]. The waveguide consists of a middle layer (called core) of higher refractive index (n_2) and thickness d, sandwiched between two identical layers (called cladding) of lower refractive index (n_1) (Fig 2.1). Since the top and bottom cladding layers are identical, the slab waveguide is symmetrical. The index profile of the waveguide is given by eq.2.1.

$$n(x) = \begin{cases} n_2, & |x| < d/2 \\ n_1, & otherwise \end{cases} \qquad 2.1$$

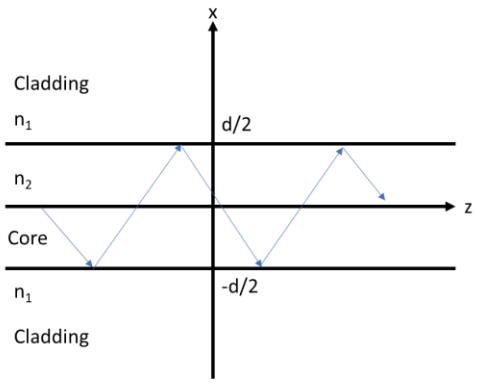


Fig 2.1 Cartoon of a symmetric slab waveguide and propagation of light in the ray model

Where d is the thickness of the core. To have guided optical modes in the core, n_2 should be greater than n_1 ($n_2 > n_1$). The electromagnetic field profiles can be solved using the Maxwell's equations. Since the layers are homogeneous, we can assume that the solutions are plane waves. The Maxwell's equations can be written as:

$$\nabla \times \overline{H} = i\omega\varepsilon_0 n^2 \overline{E}$$
$$\nabla \times \overline{E} = -i\omega\mu \overline{H} \qquad 2.2$$

Where ω is the frequency of the light. Since the slab waveguide is homogeneous along the z axis, the plane wave solutions for the wave equation can be taken as:

$$\overline{E(x,t)} = \overline{E_m(x)}\exp[i(\omega t - \beta_m z)]$$
$$\overline{H(x,t)} = \overline{H_m(x)}\exp[i(\omega t - \beta_m z)] \qquad 2.3$$

Where β_m is the propagation constant of the m^{th} mode in the z direction. By eliminating the H component from eq.2.2, we get the wave equation of the slab waveguide as:

$$\left[\frac{\partial^2}{\partial x^2} + (\frac{\omega}{c}n)^2 - \beta_m{}^2\right]\overline{E_m(x)} = 0 \qquad 2.4$$

For a guided mode confined inside the core, the field intensity $E_m(x)$, must exponentially drop to zero as $|x| \rightarrow \infty$. On the other hand, since the field is continuous, $E_m(x)$ needs to have a maximum value inside the core. Consequently, to satisfy these two conditions the quantity $(n\omega/c)^2 - \beta^2_m$ must be negative for $|x| > d/2$ and positive for $|x| < d/2$. Thus:

$$\frac{n_2\omega}{c} > \beta_m > \frac{n_1\omega}{c} \qquad 2.5$$

The modes propagating through the waveguide can be either TE (transverse electric) or TM (transverse magnetic). For simplicity lets consider only the TE mode, where the electric field is perpendicular to the plane of incidence (here xz plane). The amplitude of the guided m^{th} TE mode can then be written as:

$$E_y(x,z,t) = E_m(x)\exp[i(\omega t - \beta_m z)] \qquad 2.6$$

The electric field distribution $E_m(x)$ can be written as:

$$E_m(x) = \begin{cases} A\sin(hx) + B\cos(hx), & |x| < \frac{1}{2}d \\ C\exp(-qx), & \frac{1}{2}d < x \\ D\exp(qx), & -\frac{1}{2}d > x \end{cases} \qquad 2.7$$

The parameters h and q are related to the refractive index and propagation constant by:

$$h = \left[\left(\frac{n_2\omega}{c} \right)^2 - \beta^2 \right]^{\frac{1}{2}} \qquad 2.8$$

$$q = \left[\beta^2 - \left(\frac{n_1\omega}{c} \right)^2 \right]^{\frac{1}{2}} \qquad 2.9$$

h is the transverse component of the wavevector of the mode and 1/q is the penetration depth of the mode into the cladding layer. The electric field should also follow boundary conditions at |x| = d/2. The tangential components of the electric field ($E_y(x)$, eq 2.7) and magnetic field [$H_z = (i/\omega\mu)(\partial E_y / \partial x)$] should be continuous here (|x|=d/2). Using these two conditions we get four equations:

$$\begin{aligned} E_y(x = \frac{d^+}{2}) &= E_y(x = \frac{d^-}{2}) \\ E_y(x = -\frac{d^+}{2}) &= E_y(x = -\frac{d^-}{2}) \\ H_z(x = \frac{d^+}{2}) &= H_z(x = \frac{d^-}{2}) \\ H_z(x = -\frac{d^+}{2}) &= H_z(x = -\frac{d^-}{2}) \end{aligned} \qquad 2.10$$

Solving these equations gives us two types of mode conditions [Symmetric: A=0 (cosine) and Antisymmetric: B=0 (sine)] for the TE mode:

$$h \cdot \tan\left(\frac{hd}{2}\right) = q \qquad 2.11$$

$$h \cdot \cot\left(\frac{hd}{2}\right) = -q \qquad 2.12$$

Combining these two equations gives us the mode condition:

$$\tan(hd) = \frac{2hq}{h^2 - q^2} \qquad 2.13$$

Assuming $u = \frac{hd}{2}$ and $v = \frac{qd}{2}$, we get the conditions for the modes as:

$$\begin{aligned} v &= u \cdot \tan(u) \\ v &= -u \cdot \cot(u) \end{aligned} \qquad 2.14$$

$$u^2 + v^2 = (n_2^2 - n_1^2)\left(\frac{\pi d}{\lambda}\right)^2 = V^2 \qquad 2.15$$

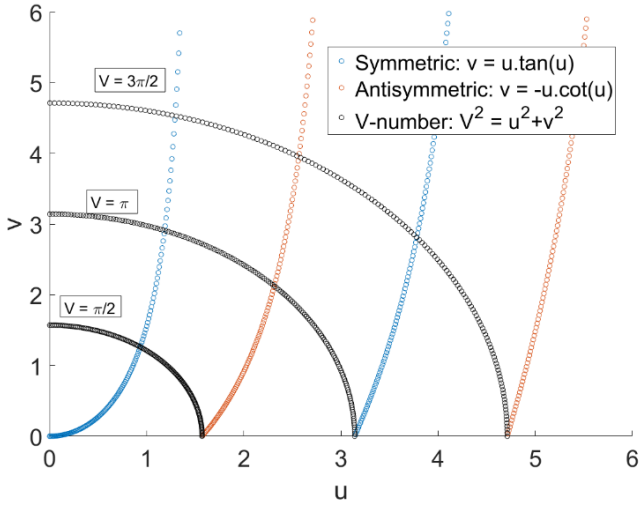


Fig 2.2 Graphical solutions for eq 2.14 & 2.15. Intersection between the V-Number plot and the mode conditions are the allowed modes that can propagate through the waveguide of thickness d.

Where V is the parameter called V-number. Fig 2.2 shows the solutions for equation 2.14. The number of symmetric and antisymmetric modes allowed in the waveguide depends on the cladding-core refractive index difference and the thickness of the slab waveguides defined by the V-number. For 0<V<π/2, there is only one intersection between the circle ($u^2 + v^2 = V^2$) and the mode conditions. Thus, only a single symmetric mode is allowed which is called the fundamental TE mode of the slab waveguide. The intersection point gives the value of u and v from which the propagation constant of the mode can be calculated. For example, assume a slab waveguide channel having high refractive index salt solution of n_2 = 1.455 surrounded by a cladding of SiO_2 of refractive index n_1 = 1.450. To propagate only a single mode through the liquid channel, the thickness of the waveguide should follow $d \le \frac{\lambda}{2\sqrt{n_2^2 - n_1^2}}$. For a wavelength of 633nm the cut off thickness for single mode condition is 2.600 μm. The cut off for having two modes (m =1,2) propagating, $d \le \frac{m \cdot \lambda}{2\sqrt{n_2^2 - n_1^2}}$, is 5.2 μm. The propagation constant of the fundamental TE mode for d = 2.6 μm is obtained from the value of 'v' intersecting with the circle at V = π/2 (v = 1.2 is the intersection point). $v = \frac{qd}{2} = \frac{d}{2}\sqrt{\beta^2 - \left(\frac{n_1 2\pi}{\lambda}\right)^2}$, from which we get $\beta = 1.453\frac{2\pi}{\lambda}$. Where 1.453 is called the effective index of refraction of the mode, n_{eff}. From fig 2.2 it is clear that as the V-number decreases, the intersection point with the mode condition also reduces. Thus, the mode propagating through the waveguide has a lower 'v' value (v = qd/2), which in turn means the mode has a higher penetration depth (1/q) into the cladding layer. The V-number is dependent on the core-cladding refractive index difference and the thickness d. Thus, by either closely matching the index of the core and cladding or by reducing the thickness of the waveguide the penetration depth can be increased. This makes the mode spread wider, covering a larger portion of the waveguide core channel. Fig 2.3(a) shows the

simulated (FIMMWAVE, PhotonD) fundamental mode of a slab waveguide with high refractive index salt solution as core. The index of the core can be tuned by changing the concentration of the salt. For a fixed thickness, as the core index is tuned closer to that of the cladding, the mode spreads more as shown by the corresponding normalized mode profile plots in fig 2.3(b). Chapter six describes how this technique is used to build optofluidic biosensors to enhance the efficiency of detecting single fluorescent particles.

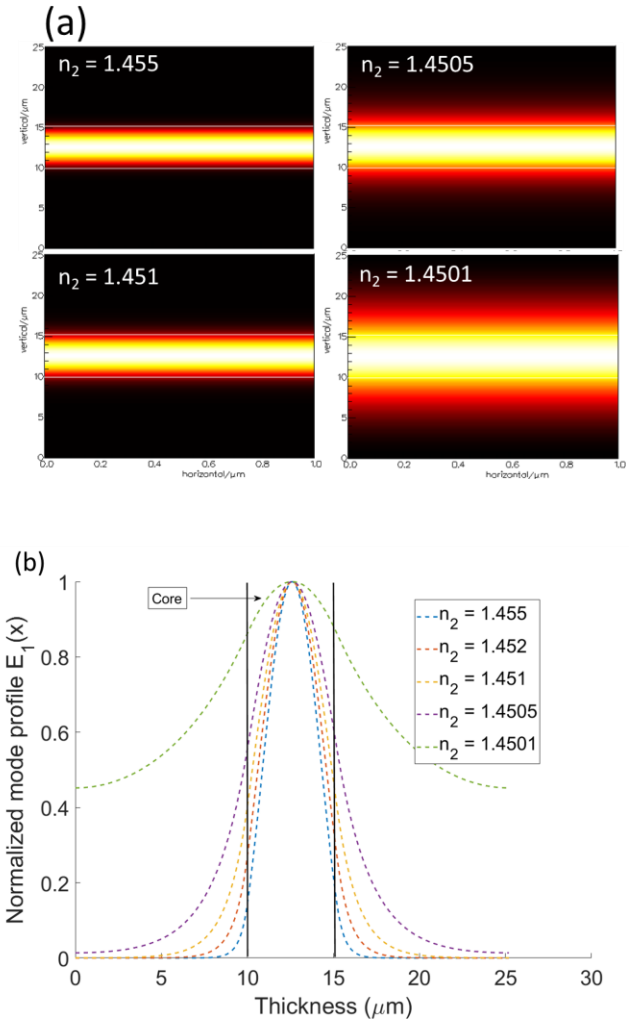


Fig 2.3 a) Fundamental mode of a 5.200 μm thick slab waveguide with varying core refractive index. b) Vertical mode profile shows the penetration depth increasing when core refractive index almost matches with the cladding (n_1 = 1.450)

2.2 ARROW waveguides

For biosensing applications, it is important to integrate fluidics and optics in a single platform. This is usually done by integrating SC optical waveguides with hollow channels. The biomolecules subtended in a water-based buffer medium are driven through the hollow channel making it a liquid channel. The light propagating through the optical waveguides intersects the liquid core (LC) channel and excites the fluorescent biomolecules. If the LC channel can also guide light, the fluorescent signals generated by the excited biomolecules can be captured and directed to a photodetector. Most optical waveguide systems are built on a Si substrate by making use of matured microfabrication techniques. Due to the low loss in visible spectrum, SiO_2 is a dielectric material that can be used for building optical waveguides for fluorescence-based sensing. Since water has a low refractive index (1.330), a LC channel build on top of a Si substrate or using SiO_2 (whose refractive indices are much larger than water, 3.800 and 1.470 respectively) cannot guide light. To circumvent this problem, LC channels can be built on top of highly efficient optical reflectors to make them behave as optical waveguides with low refractive index core. One such optical system is Anti-resonant-optical-waveguides (ARROW) [32].

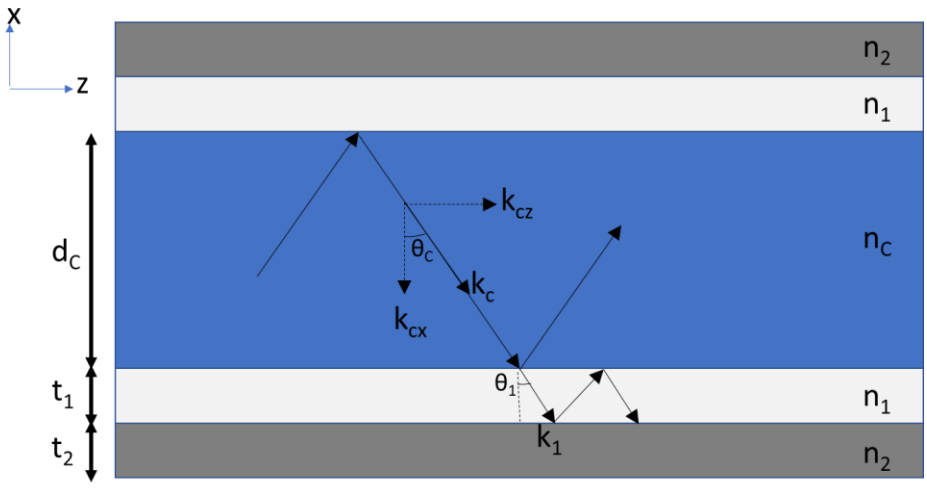


Fig 2.4 Schematic diagram of ARROW structure

An ARROW waveguide has a core of thickness d_c and low refractive index n_c. The core is sandwiched between two layers made of alternating materials with thickness t_1 and t_2 of refractive index n_1 and n_2. This is shown in fig 2.4. The top and bottom layers are designed to be a Fabry-Perot etalon in anti-resonant condition, thus functioning as a reflector. In the succeeding discussion, a geometric optics treatment is used to derive the thickness of the reflector layers. For a light ray passing through the core to be a propagating mode, the total transverse phase shift the ray acquires should be an integral multiple of 2π.

$$2d_c k_{cx} + \phi_1 + \phi_2 = 2N\pi \qquad 2.16$$

Where ϕ_1 and ϕ_2 are the phase accumulated from reflection at the top and bottom boundaries of the core and k_{cx} is the propagation constant of the mode in x direction. Since $n_c < n_1$, both these phase values are zero or π.

$$\therefore \quad 2k_{cx}d_c = 2\pi$$

$$\cos(\theta_c) = \frac{\lambda}{2n_c d_c} \qquad 2.17$$

Also using Snell's law at the boundaries, we have:

$$\sin(\theta_1) = \frac{n_c \sin(\theta_c)}{n_1} \qquad 2.18$$

Where θ_c and θ_1 are the angel of incidence of the light in the respective layers. To have the top and bottom layers behave as reflectors, the total phase shift of the light propagating in those layers need to meet the anti-resonant condition. For layer 1,

$$2t_1 k_{1x} + \psi_1 + \psi_2 = (2N-1)\pi \qquad 2.19$$

Where ψ_1 and ψ_2 are the phase shift accumulated from reflections. If the material is chosen such that $n_1 > n_c$ & n_2, then the phases due to reflection will be zero. Thus,

$$2t_1 k_{1x} = (2N-1)\pi \qquad 2.20$$

$$2t_1 k_1 \cos(\theta_1) = (2N-1)\pi \qquad 2.21$$

Using eq 2.18 and 2.17 we get the equation for t_1 as,

$$t_1 = \frac{(2N-1)\lambda}{4\sqrt{n_1^2 - n_2^2 + \frac{\lambda}{4d_c^2}}} \qquad 2.22$$

The same relation holds for the i^{th} layer of the reflector. For a LC waveguide of large core thickness (d_c = 5 µm) filled with water (n_c = 1.330) and built with SiO_2 (n_1 = 1.470) and Ta_2O_5 (n_2 = 2.100) as the reflectors, $n_1^2 - n_c^2 >> \frac{\lambda^2}{4d_c^2}$. So, for a large core and layers with dissimilar refractive index, the thickness of the anti-resonant layers can be approximated as,

$$t_i = \frac{(2N-1)\lambda}{4\sqrt{n_i^2 - n_c^2}} \qquad 2.23$$

2.3 Multi-Mode-Interference (MMI) waveguides

An MMI waveguide is very wide waveguide that can support multiple modes propagating at different propagation constant. These modes can constructively interfere with each other as they propagate along the length of the waveguide to generate well defined patterns with the self-images of the input mode. MMI waveguides are very commonly used as splitters to equally split the input optical power and route them to different parts of an optical chip. This thesis will later describe how MMI waveguides can be used for spectral and spatial multiplexed detection of biomolecules. Below a discussion of the general design of MMI waveguides is given, which is based on the work by Soldado and Pennings [33].

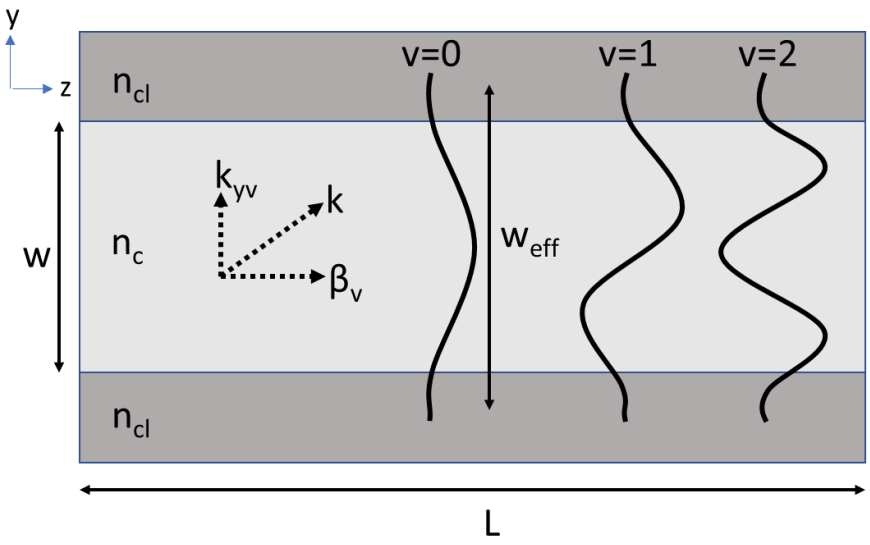


Fig 2.5 Schematic of a wide MMI waveguide that can support multiple modes

The MMI waveguide has an input single mode waveguide which expands to a wide waveguide of width w and length L (fig 2.5). When excited by wavelength λ, the number of modes propagating in the MMI waveguide is dependent on the V-number (as described in section 2.1) $V = \frac{w\pi}{\lambda}\sqrt{n_c^2 - n_{cl}^2}$, where n_c and n_{cl} are the core and cladding refractive index and is given by:

$$m \leq \frac{2V - \varphi}{\pi} \qquad 2.24$$

Φ is the phase difference acquired at the boundary of the waveguide. When the waveguide is wide enough, it can support multiple modes (v=0,1,2,3..m-1) alternating between symmetric and antisymmetric. The effective width of these modes, the width of the waveguide along with the penetration depth of the mode, is approximately the same as that of the fundamental mode and is given by the formula,

$$w_{eff} \approx w + \left(\frac{\lambda}{\pi \sqrt{n_c^2 - n_{cl}^2}} \right) \left(\frac{n_{cl}}{n_c} \right)^{2\sigma} \qquad 2.25$$

Where σ = 0 and 1 for TE and TM respectively. At a wavelength of 0.633 μm for a 75 μm wide waveguide with n_c = 1.510 and n_{cl} = 1.440, the w_{eff} is 0.450 μm on each side. In the later chapters, for quick analytical calculations we use $w_{eff} \approx w$ of the waveguide. The modes propagate with a propagation β_v in the forward direction and wavenumber k_{yv} in the transverse direction and such that,

$$k_{yv}^2 + \beta_v^2 = k_0^2 n_c^2 \qquad 2.26$$

$$\beta_v = k_0 n_c \sqrt{1 - \left(\frac{k_{yv}}{k_0 n_c} \right)^2} \approx k_0 n_c - \frac{k_{yv}^2}{2 k_0 n_c} \qquad 2.27$$

k_{yv} is related to w_{eff} by the equation $k_{yv} = \frac{(v+1)\pi}{w_{eff}}$. Using this in eq 2.27 gives us the propagation constant for each mode as,

$$\beta_v = k_0 n_c - \frac{(v+1)^2 \pi \lambda}{4 w_{eff}^2 n_c} \qquad 2.28$$

The beat length (where the modes are out of phase) for the lowest two modes is given by,

$$L_\pi = \frac{\pi}{\beta_0 - \beta_1} \approx \frac{4 n_1 w_{eff}^2}{3\lambda} \qquad 2.29$$

From eq 2.28 and 2.29 we get

$$\beta_0 - \beta_v = \frac{v(v+2)\pi}{3 L_\pi} \qquad 2.30$$

Let ψ(y,0) be the field distribution of the mode at the input of the MMI waveguide (at z = 0). This mode expands to the multiple modes $\psi_v(y)$ (orthogonal to each other) propagating in the MMI waveguide. Therefore the input mode can be written as the summation of all these field distributions,

$$\psi(y,0) = \sum_{v=0}^{m-1} c_v \psi_v(y) \qquad 2.31$$

Where c_v is the normalized integral overlap between input field and the mode v.

$$c_v = \frac{\int \psi(y,0)\psi_v(y)dy}{\sqrt{\int \psi_v^2(y)dy}} \qquad 2.32$$

Therefore, the field distribution at a length z is the superposition of the field distribution of all the modes,

$$\psi(y,z) = \sum_{v=0}^{m-1} c_v \psi_v(y) e^{i(\omega t - \beta_v z)}$$

$$\psi(y,z) = e^{i(\omega t - \beta_0 z)} \sum_{v=0}^{m-1} c_v \psi_v(y) e^{i(\beta_0 - \beta_v) z} \qquad 2.33$$

Since $\omega t - \beta_0 z$ is the time dependence of the field and is a common factor for all the fields, it is dropped from the equation. By using eq 2.30 we get,

$$\psi(y,z) = \sum_{v=0}^{m-1} c_v \psi_v(y) e^{i(\frac{v(v+2)\pi}{3L_\pi})z} \qquad 2.34$$

Thus, the mode profile at position z along the MMI waveguide depends on the factor,

$$e^{i(\frac{v(v+2)\pi}{3L_\pi})z} \qquad 2.35$$

The field profile at a distance z = L is given by,

$$\psi(y,z)=\sum_{v=0}^{m-1}c_v\psi_v(y)e^{i(\frac{v(v+2)\pi}{3L_\pi})L} \qquad 2.36$$

The input field profile is replicated if this factor (eq 2.35) is equal to 1. If the factor in eq 2.35 is equal to $(-1)^v$, then the symmetric and antisymmetric modes will be in and out of phase. This will result in direct replica (=1) and mirrored replica (=-1) of the input mode field. This condition can be obtained when,

$$L=p(3L_\pi) \text{ with p = 0,1, 2...} \qquad 2.37$$

Therefore, for odd or even p the output field results in direct self-image or mirrored images of the input field respectively. This design is used for making cascade MMI waveguides and cross couplers. At certain lengths, the output of the MMI waveguide can also be multiple replicas of the input field.

In this thesis, the MMI waveguides used for multiplexed detection is designed to have a symmetric input. The input field is generated by a single mode waveguide exciting the MMI waveguide at the center. For this case, N different self-images of the input field are obtained as the output of the MMI waveguide at distances,

$$L=\frac{3pL_\pi}{4N} \qquad 2.38$$

For p = 1 and using eq 2.29 we get,

$$NL=\frac{n_c w_{eff}^2}{\lambda} \qquad 2.39$$

Thus, the MMI waveguide can be designed such that excitation with two different wavelengths could produce two different number of replicas of the input field (eq 2.40). This design is used

in chapter three for demonstrating up to 7X multiplexed detection of nucleic acids on an ARROW platform using spectral multiplexing with an MMI waveguide intersecting a single LC waveguide.

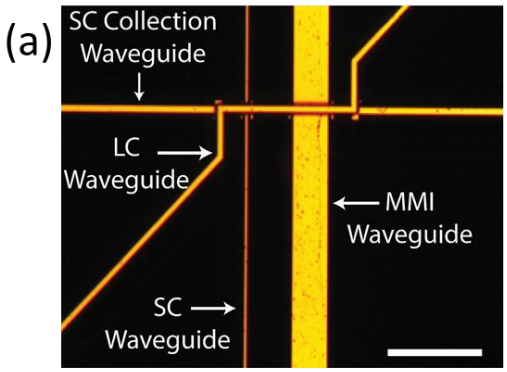
$$N_1\lambda_1 = N_2\lambda_2 = \frac{n_c w_{eff}^2}{L} \qquad 2.40$$

Similarly, the MMI waveguide can also be designed to have different number of replicas of the input field at different lengths using a single excitation wavelength (eq 2.41). This design is used in chapter four to build a biosensor with a single MMI waveguide to excite three spatially separated LC waveguides. 3X multiplexed detection of bacterial plasmids with antibiotic resistance genes is demonstrated using this spatial multiplexing technique.

$$N_1 L_1 = N_2 L_2 = \frac{n_c w_{eff}^2}{\lambda} \qquad 2.41$$

2.4 ARROW biosensor experimental setup

Fig. 2.6a shows the top down optical image of an ARROW biosensor chip. The chip has a SC excitation waveguide orthogonally intersecting a LC waveguide. Fluorescently tagged particles are flowed through the inlet of the LC waveguide and flowed to the outlet by applying a negative pressure at the outlet using a vacuum line, as shown in fig 2.6b. The chip also has a wider MMI waveguide adjacent to the SC excitation waveguide for multiplexed detection of biomolecules.



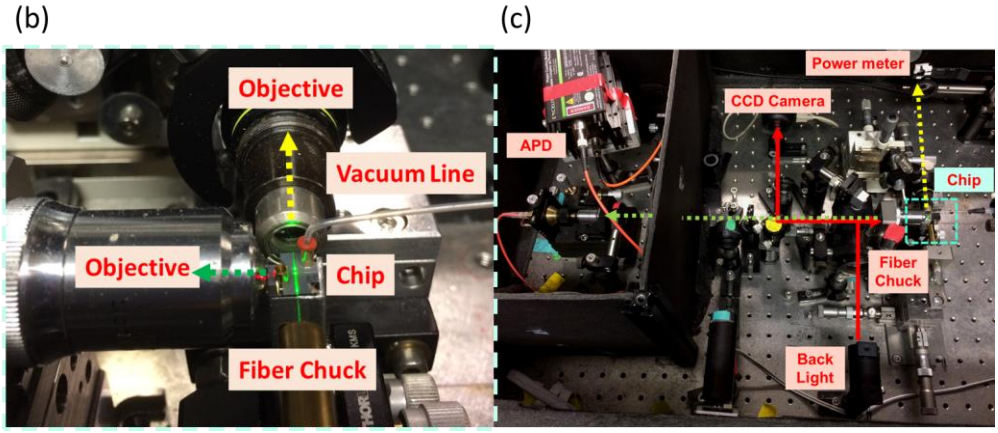


Fig 2.6 a) Top down optical image of the ARROW biosensor chip. b) Zoomed in image of the optical setup with the biosensor chip coupled with fiber. c) Image of the complete experimental setup with the SC collection and excitation waveguide of the ARROW chip aligned to an APD and a power meter.

The SC waveguide is excited with a laser source using a butt coupled fiber. When the fluorescent particles flow and reach the SC-LC intersection, they get excited by the SC waveguide. The fluorescent signal from the particle is collected by the LC waveguide, orthogonal to the SC excitation waveguide and captured by a SC collection waveguide (shown in fig 2.6a). The signals are sent to an avalanche photo detector (APD) using a 60x “collection objective” after filtering out the excitation light with a band-pass optical filter (shown in fig 2.6b and 2.6c). The transmitted excitation light coming out of the chip through the SC waveguide in the transverse direction and is collected with another objective and measured using a power meter. The fluctuations in this measurement indicates any drift in the chip and possible misalignments. The experimental setup also has a provision to illuminate the facet of the waveguides using the “collection objective” and image with a CCD camera (shown in fig 2.6c).

2.5 Optimization of ARROW waveguide performance

As mentioned in the previous section, the ARROW biosensor chip is integrated with a wider MMI waveguide to have multiplexed detection capabilities. The MMI waveguide is wide enough to support multiple modes propagating with different propagation constants. These modes interfere with each other to generate well defined spots at specific distances. These spots are

the self-image of the single mode waveguide that expands into the wider MMI waveguide. The MMI waveguide of core refractive index n_{co} is designed to intersect the LC waveguide at a specific length L. The width, w and length L, of the MMI waveguide are chosen so as to generate well defined patterns with N_c number of spots when excited with light of wavelength λ_c.

$$N_C \lambda_C = \frac{n_{co} w_{eff}^2}{L} \qquad 2.42$$

The MMI waveguide of the ARROW biosensor is designed to produce six, seven and eight spots in the LC waveguide when excited by visible wavelengths 738 nm, 633 nm, 556 nm, respectively. Targets excited by the MMI waveguide generate fluorescent signals encoded with distinct temporal patterns based on their specific fluorescent color tag. The target information is fully encoded in this time-domain signal which is demultiplexed using a signal processing algorithm. To get clear distinguishable signals from each target, it is very important to design the MMI waveguides that generate clean, distinguishable excitation spot patterns for the three wavelengths of light. This depends on the dimensions (L and w_{eff}) and also the input mode profile of the single mode waveguide which excites the MMI waveguide.

The ARROW single mode waveguide is designed to be a rib waveguide which is 6-7 μm thick and 4-5 μm wide. The waveguide has about a 3.500 μm deep rib. The detailed fabrication process of the ARROW biosensor is well documented and available from multiple sources [34]. Very briefly, the ARROW chips were fabricated on a 100 mm <100> oriented silicon wafer. A sequence of dielectric layers was sputter deposited on the substrate for optical guiding. These cladding layers consisted of Ta_2O_5 and SiO_2 (refractive index 2.107 and 1.460 respectively). The sequence of the dielectric material layers was chosen to be SiO_2/ Ta_2O_5/ SiO_2/ Ta_2O_5/ SiO_2/ Ta_2O_5/ starting from the substrate with thickness 265/102/265/102/265/102/ nm. SU8 photoresist (Microchem) was spun on top, patterned and developed to define a 5 μm x 12 μm (thickness x width) LC waveguide channel. SU8 photoresist and a thin nickel layer were used

as a mask to selectively etch a self-aligned pedestal into the wafer using a reactive inductively coupled-plasma reactive ion etcher (ICP-RIE). A single layer of 6 μm SiO_2 (refractive index 1.460) was deposited on top of the SU8 by plasma-enhanced chemical vapor deposition (PECVD). 4 μm tall ribs were etched into this SiO_2 layer using ICP-RIE to form the single mode SC waveguide, MMI waveguide and SC collection waveguides which intersect the LC waveguide at multiple points. Fluidic inlets into the LC waveguide channels were exposed with a wet etch through the top layers of SiO_2. The SU8 was then removed with a bath in H_2SO_4 : H_2O_2 solution to form the hollow core which takes several days. This is followed by a long water bath to clean the wafer and remove all the acid solution that is filled in the LC channel of the chip.

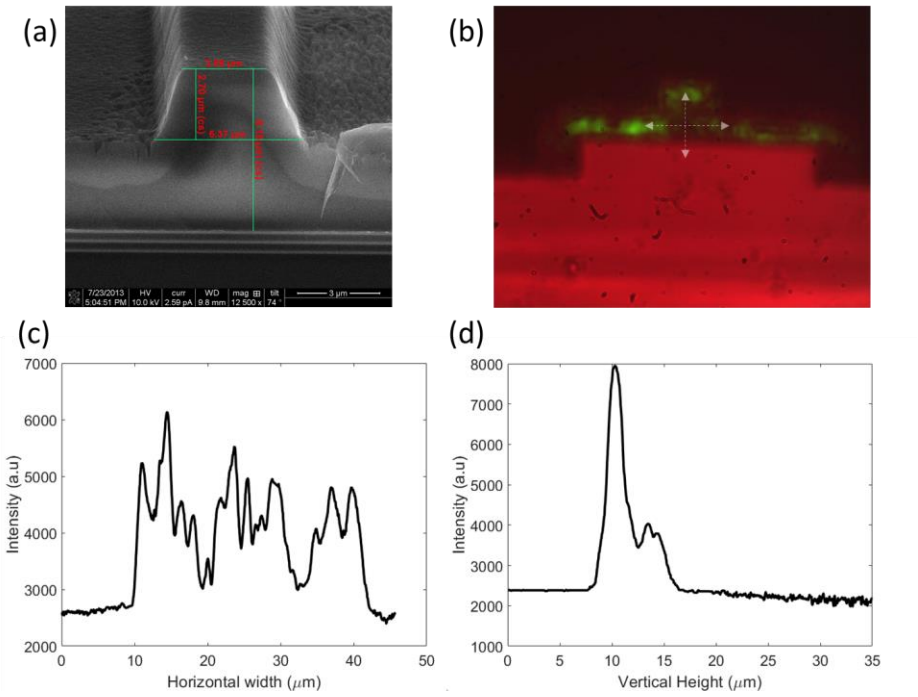


Fig 2.7 a) SEM cross section image of an ARROW rib waveguide. b) Mode image of the single mode waveguide. c) & d) Horizontal and vertical profile of the mode

It is to be noted that bulk SiO_2 deposited via PECVD is porous in nature. During long wet etch steps, water can diffuse through the SiO_2 waveguide and form an upper layer with higher refractive index. This is clearly seen as a distinct upper layer in the SEM cross section image

of the ARROW single mode waveguide (shown in fig 2.7a) [35]. Fig 2.7b shows the mode image of the single mode waveguide excited by 556 nm wavelength. The double lobed vertical profile of the mode clearly indicates propagation through the upper higher index layer. The horizontal mode profile is also poor and is spread outside the guiding region. The mode thus has a very low confinement factor of 32%. This mode profile when self-imaged by the MMI waveguide generates a very poor pattern with no distinct excitation spots in the LC waveguide. Fig 2.8 shows the top down fluorescent dye image of the excitation pattern generated by 75 µm wide MMI waveguide in the LC waveguide and the horizontal intensity distribution.

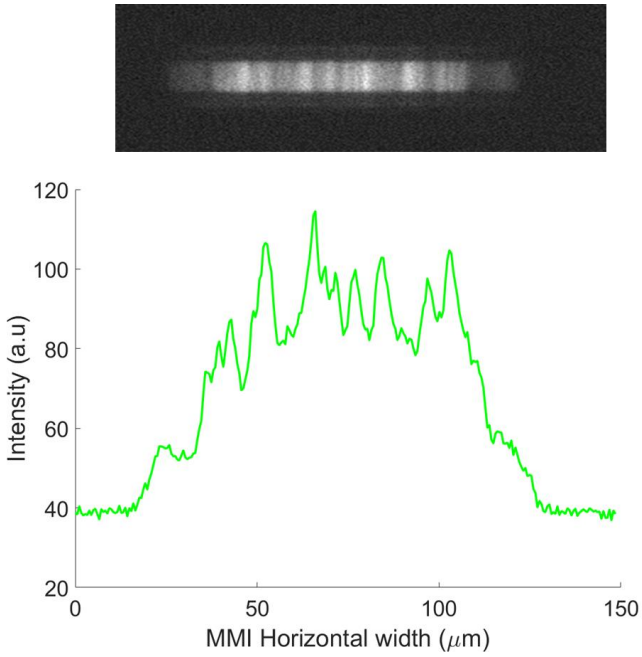


Fig 2.8 Top down fluorescent dye image of the pattern generated by an ARROW MMI waveguide in the LC waveguide

A buried waveguide design can be used to mitigate the effects caused due to water absorption by the SiO_2 waveguide. In this case, a high index SiO_2 (1.510) is deposited first using PECVD which is etched by ICP-RIE to form the core of the waveguide. Later the core is buried with a thick layer of low index SiO_2 (1.448). This low index oxide not only acts as a cladding layer for

the rib waveguide but also protects the core from any liquid absorption [36]. Fig 2.9a shows the SEM cross section image of the buried ARROW rib waveguide, the core has no distinct upper high index layer. The waveguide has a mode profile with well-defined single lobed profile. The mode is better confined within the guiding region with a confinement factor of 73% and so gives a cleaner MMI pattern. The MMI patterns can be analyzed quantitively by using a peak-to-valley (p-v) number, defined as the difference between the average peak and valley of the normalized horizontal intensity distribution of the pattern. The p-v number can have a maximum value of 1, indicating an MMI excitation pattern with well defined spots with equal intensity (peak = 1) and negligible background noise (valley = 0).

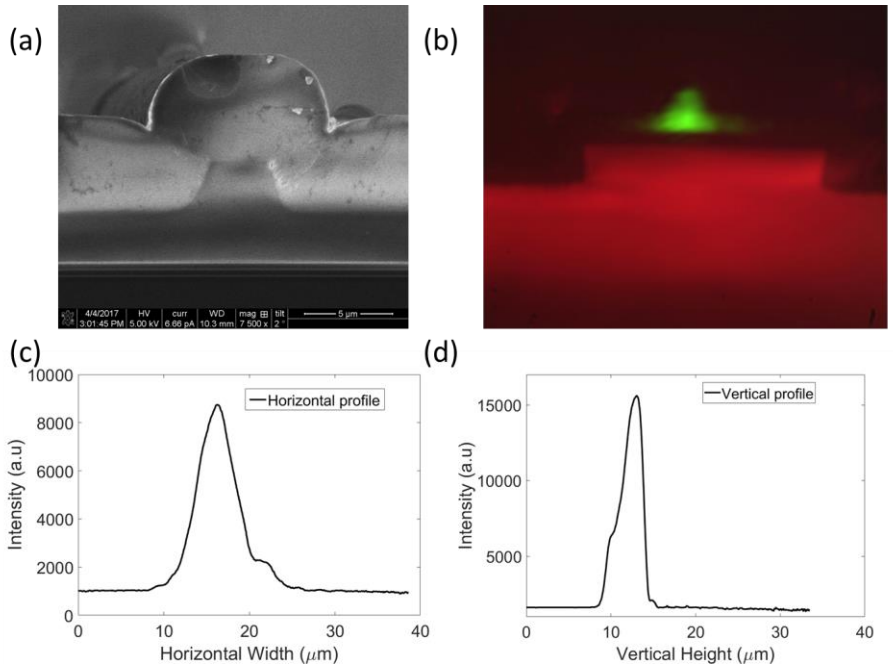


Fig 2.9 a) SEM cross section image of a buried ARROW rib waveguide. b) Mode image of the waveguide excited with 556 nm wavelength. c) & d) Horizontal and vertical mode profile

Though the single mode waveguide has a tightly confined vertical profile with FWHM of 3.000 µm, the horizontal profile is still much wider (FWHM = 4.700 µm). The MMI pattern generated by this waveguide will have broader spots with high background noise. The buried ARROW MMI waveguides generate the correct pattern with eight spots (fig 2.10) but with a large FWHM

of 7 µm and low p-v value of 0.450 at 570 nm wavelength, which is shifted by 2%, i.e. 15 nm from the design wavelength (8 spots at 556 nm excitation). The extra buried oxide layer increases the effective width of the fundamental mode of the MMI waveguide by 1.5% which results in a shift in the design wavelength by twice this value, 3%. This corresponds to a wavelength shift of 17 nm, close to the observed shift. Thus, the design wavelength of the MMI waveguide is very closely dependent on the effective width. By optimizing the rib thickness of the single mode waveguide, the mode can be further confined within the guiding region. This will further improve the MMI patterns to a much higher p-v value. The length 'L' of the 75 µm wide MMI waveguide also needs to be redesigned to generate the pattern with correct number of excitation spots at the design wavelength of 556 nm.

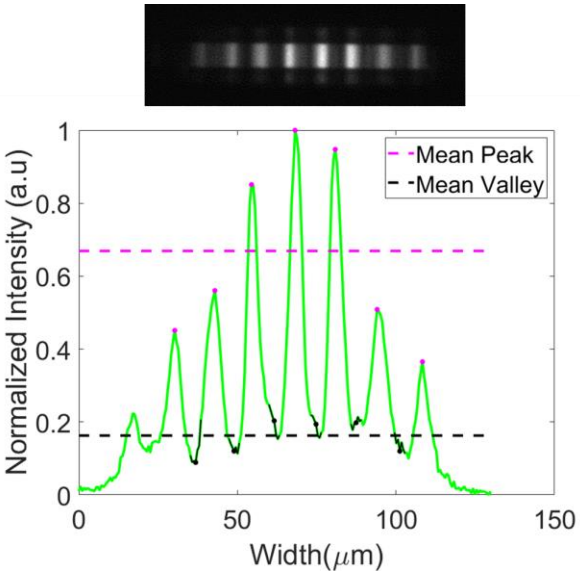


Fig 2.10 MMI pattern and normalized horizontal profile generated by a buried ARROW MMI waveguide

Simulations to design the MMI waveguide length are done using PhotonD. The device layout consists of a single mode buried ARROW waveguide exciting a wider MMI waveguide. FEM method is used to build the fundamental mode of the single mode waveguide and all the eigen modes of the MMI waveguide. An eigen-mode-expansion method (using FIMMPROP in PhotonD) is used to propagate light through the waveguide. The patterns generated by the

MMI waveguide when excited by the four designs wavelengths (488 nm, 556 nm, 633 nm & 738 nm) are characterized by the p-v value and the FWHM of the output mode profiles. A simulation scan for different MMI lengths is done. The length which generates a field profile with lowest FWHM and highest p-v value for all four wavelengths is chosen. Fig 2.11 shows the simulation process and fig 2.12 shows the FWHM and p-v value of the patterns generated by the 75 µm wide MMI waveguide for different lengths. The optimum length that generates pattern with nine, eight, seven and six spots for 488 nm, 556 nm, 633 nm and 738 nm wavelength respectively is circled as a blue shade in the plots.

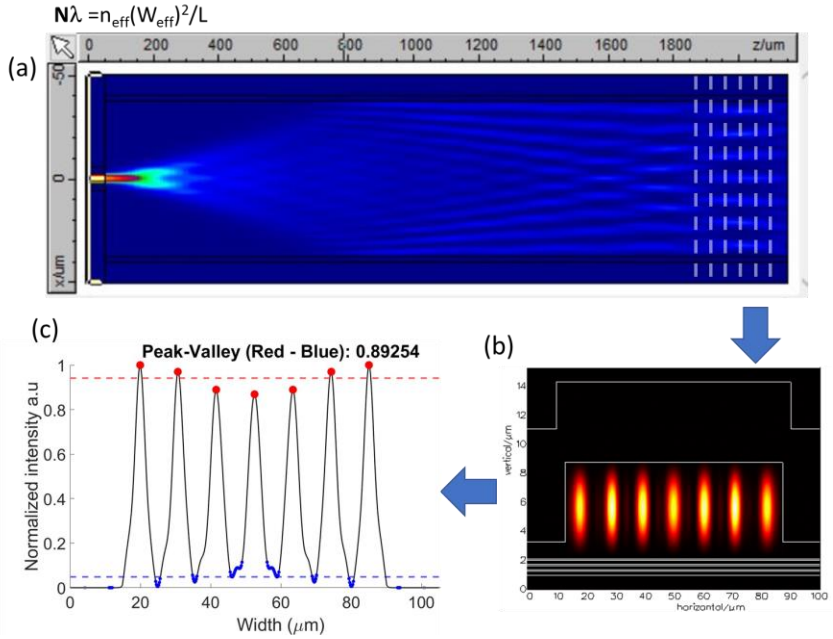


Fig 2.11 a) top down field profile of the simulated MMI waveguide. b) & c) Cross-sectional field profile of the MMI waveguide output.

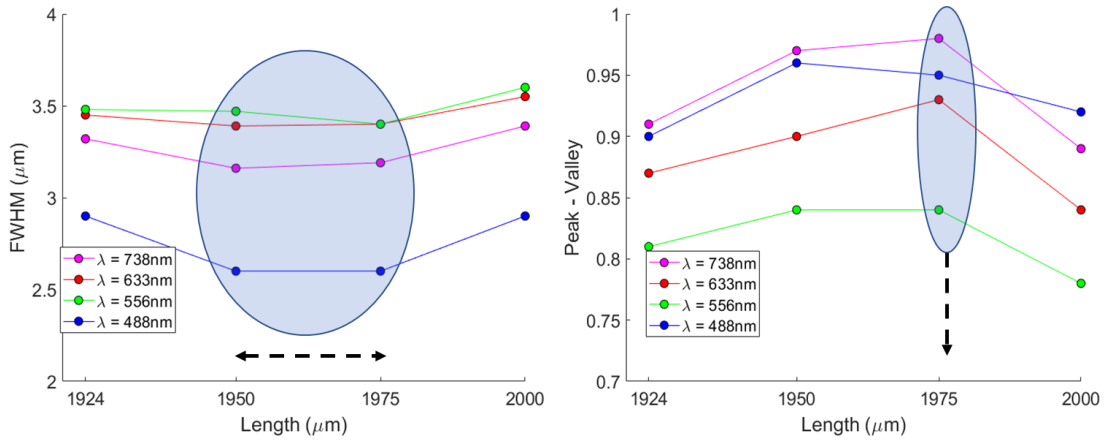


Fig 2.12 FWHM and p-v values of the MMI waveguide output for different lengths.

Fig 2.13 shows the mode image and intensity profile of a buried ARROW single mode waveguide. The waveguide has an optimized rib of 1 µm to have a very tightly confined single mode with 2.600 µm and 2.300 µm vertical and horizontal FWHM. The mode has a confinement factor of 98%.

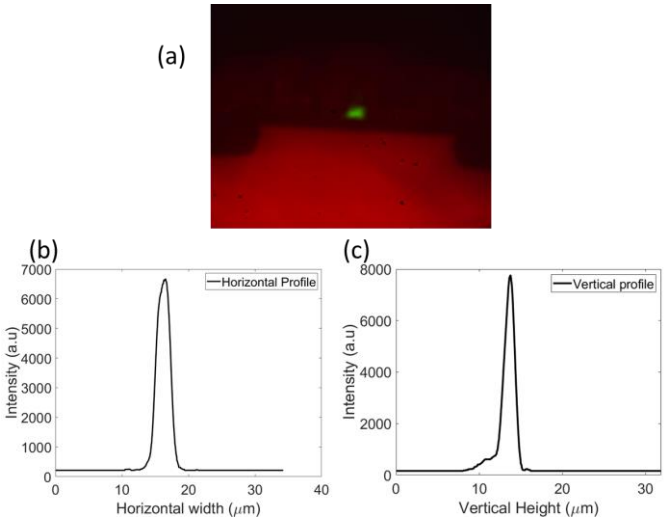


Fig 2.13 Mode image and profile of buried ARROW single mode waveguide with optimized rib height.

Using this as the input source and an optimized length of 1975 µm, the MMI waveguide generates patterns with very distinct spots in the LC waveguide with an improved p-v value of

0.7 and small horizontal FWHM of 4 µm. Fig 2.14 shows the color-coded patterns generated in the LC waveguide [37, 38].

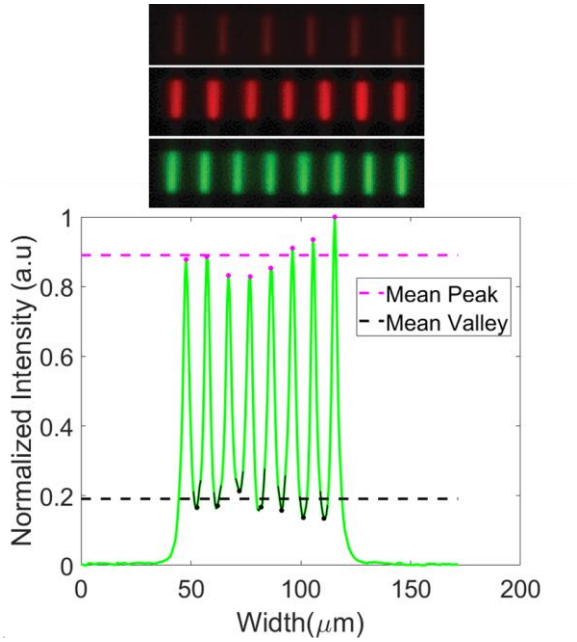


Fig 2.14 Color-coded fluorescence image of the MMI patterns and normalized horizontal intensity profile generated by an optimized buried ARROW waveguide

Apart from guiding well confined modes, the buried oxide also positions the mode to be better vertically aligned with the center of the 5 µm LC waveguide (Fig 2.15a shows the SC-LC cross section). Fig 2.15b shows the mode positions with respect to the substrate from four and three different wafer runs of ARROW waveguides with and without buried layer respectively. The modes of the buried waveguides are consistently positioned at around 3.300 µm close to the center of the LC waveguide as compared to a regular ARROW waveguide positioned at 6 µm (caused by the distinct upper layer from water absorption). This improves the SC-LC waveguide coupling efficiency. Fig 2.15c shows the comparison of fluorescence signals detected by ARROW and buried ARROW waveguide. Each individual peak above the background corresponds to a signal generated by a standard 200 nm fluorescent bead flowing past the SC-LC intersection. The signals from ARROW waveguide with the protective buried layer

generates signals with more than 30x higher signal-to-noise (SNR) ratio because of better SC-LC mode coupling [6].

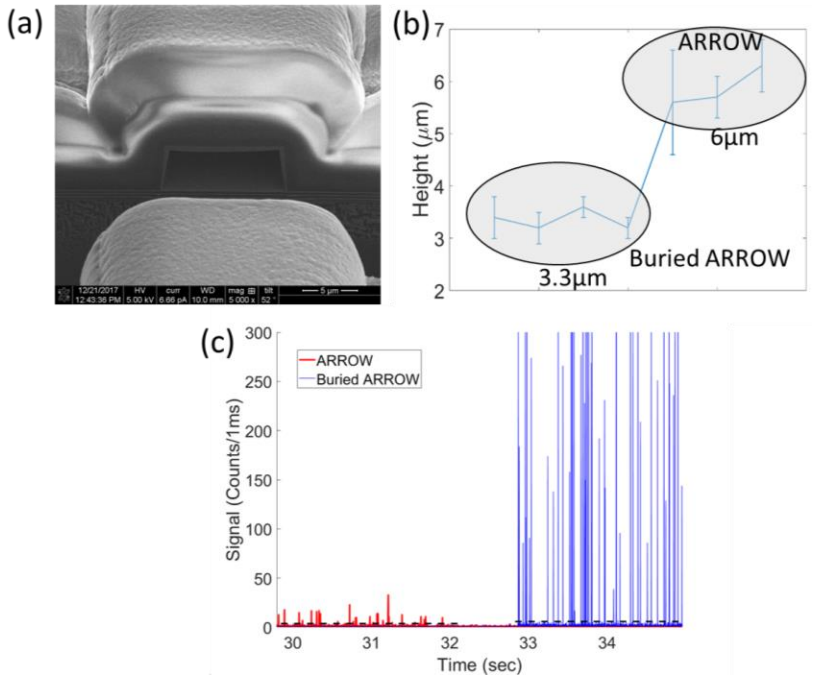


Fig 2.15 a) SEM image of the SC-LC intersection of an ARROW biosensor. b) Optical mode position with respect to the substrate. c) Fluorescence signal from micro beads detected by ARROW waveguide with and without buried oxide layer.

3 Spectral multiplexing: 7x multiplexed detection of nucleic acid targets

The next two chapters (3 and 4) describe the application of ARROW biosensor device aimed towards multiplexed detection of antibiotic resistance bacterial targets. Over the years, disease causing bacterial targets have evolved to have mutations resistant to antibiotics. They have emerged as a global threat with several epidemics involving theses pathogens already been observed in this decade. Unregulated medications have enabled disease causing bacteria to develop multiple different mutations and adapt against several classes of antibiotics. More recently a new class of mutations such as *Verona integron metallo-β lactamase* (VIM), *New Delhi metallo-β-lactamase* (NDM), *Imipenemase* (IMP) and *Klebsiella pneumoniae carbapenemase* (KPC) have emerged and spread among bacteria which give antibiotic resistance against higher level β-Lactam antibiotics such as carbapenem [39-41]. Ineffectiveness of tertiary level antibiotics against these bacteria makes it hard for physicians to fight and contain infections especially among weak patients who have gone through complicated medical treatments and are in risk of secondary infections [42]. This scenario has led to an urgent need to develop not only new antibiotics but also new technologies for rapid, sensitive and early stage diagnosis of these mutations.

This chapter talks about how the full spectral multiplexing power of MMI waveguides can be used for multiplexed detection of antibiotic resistance bacterial panel of seven different targets (three species: *E. coli, E. aerogenes and K. pneumoniae* and four antibiotic resistance genes: VIM, NDM, KPC and IMP) [43].

The ARROW biosensor chip described in chapter two integrated with an MMI waveguide is used to do spectral multiplexed detection of the targets (Fig 3.1a). The MMI waveguide of refractive index n_{co} (here 1.510) is designed to intersect the LC waveguides at a specific distance L. The width w (here 75 μm) and length L (here 1975 μm) of the MMI waveguide are chosen (design described in section 2.5) so as to generate well defined patterns with Nc number of spots when excited with light of wavelength λc (Eq. 2.42). The MMI waveguide

produces six, seven and eight spots in the LC waveguide when excited by 738 nm, 633 nm and 556 nm, respectively (Fig 3.1b). The fluorescently tagged analytes flowing through the LC waveguide is excited simultaneously by Ti:Sapphire (738 nm), HeNe (633 nm) and solid-state (556 nm) lasers. The signals generated by the targets are captured by the collection waveguide and detected using an avalanche photo detector, as described in section 2.4. The targets excited by the MMI waveguide generate fluorescence signals encoded with distinct temporal pattern based on their specific color label. Thus, target information is fully encoded in the time-domain signal which is demultiplexed using a signal processing algorithm.

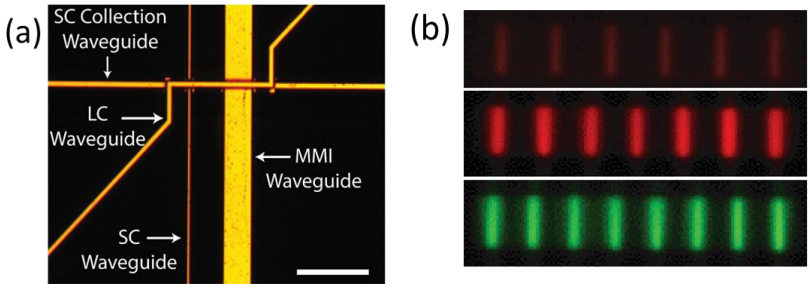


Fig 3.1 a) Top down image of ARROW chip with MMI waveguide. b) MMI patterns generated when excited by 738 nm, 633 nm and 556 nm.

Because this application involves multiplexed detection of several targets using an MMI waveguide, it is not practical to use seven different wavelengths to excite the targets. Number of excitation wavelengths are limited by available fluorescent dye laser combinations, complexity in the experimental setup design and absorption-emission spectral overlap. This bottleneck can be solved by using a combinatorial color labeling approach which will still make sure that signal from each target still has a unique spectral information encoded, provided there is no absorption-emission overlap between the different labels. Thus, using M number of wavelengths, we can now have multiplexing scaled up to 2^{M-1}. 7x multiplexed target detection of antibiotic resistant bacterial panel is done by using three different color labels Dark Red (DR), Red (R) and Green (G) corresponding to the design wavelengths 738 nm, 633 nm and

556 nm of the MMI waveguide to create seven distinguishable color combinations (DR, R, G, DR-R, R-G, G-DR, DR-R-G). Table 3.1 shows the assigned color combinations for each target.

Target	E.Coli	KPC	VIM	IMP	NDM	K.Pneu	E.Aero
Color code	DR	R	G	DR-R	R-G	G-DR	DR-G-R

Table 3.1

3.1 Nucleic acid assay design

Target	Capture Oligomer	Fluorescent probe oligomer	Color Code
E.Coli	5'AACGGGGAAACTCAGCAAGC GCACTTACAGG/3BioTEG/	/5Alex750/GCTACCAAGCCGA AAGAACTGTACAGCGAAGAGG CAGTGTAGC3'	Dark red
KPC	5'GGTGGCAGAAAAGCCAGCCA GCGGCCATGAGAGACAAGAC AGCAGAACTAGACGGCGATA /3BioTEG/	/5TYE665/CGCACAAAGTCCTG TTCGAGTTTAGCGAATGGTTCC GCGACGATGCG3'	Red
VIM	5'TCTGGTAAAGTCGGACCTCT CCGACCGGAATTTCGTTGAC TGTCG/3BioTEG/	5'TCGCCGTCAAACGACTGCGTT GCGATATGCGACCAAACACCGG CGA/3Alex546/	Green
IMP	5'GATGGATTGAGAATTAAGCC ACTCTATTCCGCCCGTGCTG TCAGCCCG/3BioTEG/	/5Alex750/TTTAAGCAGCTCAT TAGTTAATTCAGACGCATACGTG GG3' /5TYE665/ACTAGGTTATCTGGA GTGTGTCCTGGGCCTGGAT3'	Dark red - Red
NDM	5'ATGTCGAGATAGGAAGTGTG CTGCGAAACCCGGCCAGACA TTCGGTGCGA/3BioTEG/	/5Alex546/ACCGACATCCCTGA CGATCAAACCGTTGGAAGCGAC TGTCGGT3' 5'GATGCGTTGATCTCCTGCTTG ATCCAGTTGAGGATCTGGGCG CATC/3TYE665/	Red - Green
K.Pneu	/5BioTEG/GTCGCCAGGC CGCTGGCGCGCTTGGTCATA AAGTTATCGGTCTGGGCAGA3'	/5Alex546/ CGCCGCCGAATTC CGGGAACATATCGGTCCAG3' 5'CGTACAGGGCGCCAAGGTTA CGACCGTAGTC/3Alex750/	Green - Dark red
E.Aero	5'AACAACCGTATCGGTGACAA CCATGACACCGGCGTTTCCC CAGTATTCGCTGGCG/3BioTEG/	5'CCGTCTGGGCGGCATGGTATG GCGCGCTGACTCC /3Alex750/ /5Alex546/CTGGGTTACCCGA TCACTGACGATCTGGACATC /5TYE665/CGGCGCATTCAAAG CTCAGGGCGTTCAGCTGACC	Dark red - Red - Green

Table 3.2

A magnetic bead-based sandwich assay is used for capturing and labeling the nucleic acids. 10 µL of 3 µM synthetic nucleic acid strands corresponding to antibiotic resistant bacterial target was mixed with 10 µL of 10 µM of target specific fluorescent probe oligomers [IDT DNA Inc.]. The final volume for each target-probe mixture was made to 30 µL by adding 1XT50 buffer.

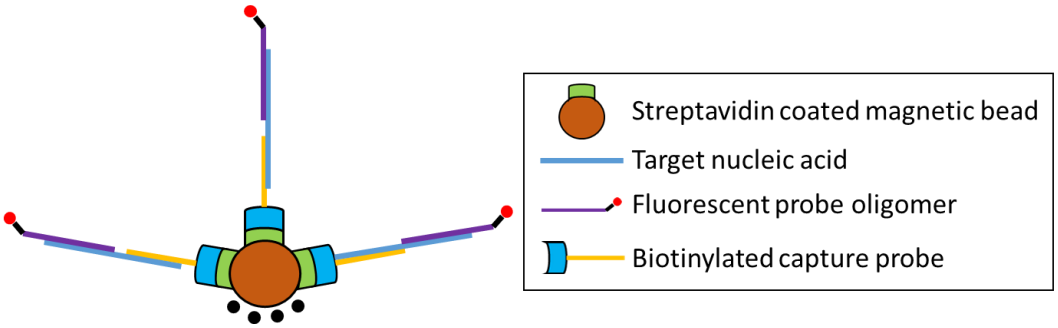


Fig 3.2 Sketch of the final bead-based assay with the captured target-probe complex

The types of fluorescent probes correspond to the assigned color combination code for the target (Fig 3.2). The target-probe mixture was heated to 95^0 C for 5 mins and incubated for 3 hrs. Streptavidin coated magnetic beads [Dynabeads^{TM}] were functionalized with target specific biotinylated capture oligomers. After incubation the hybridized target-probe structure was mixed with the functionalized magnetic bead and rotator mixed for 1 hr. Each magnetic bead has a maximum of about 10^5 binding sites. A magnet kept under the vial was used to pull down the magnetic bead assay with the captured target-probe complex. All unbound nucleic acid strands were washed off with multiple buffer exchanges and the assay was resuspended. Table 3.2 shows the sequences of capture probe and fluorescence probe used for each target.

3.2 Single color tagged target identification

The ability of the ARROW biosensor device and the signal processing algorithm to accurately detect and identify each target is first demonstrated. This is done by analyzing signals from experiments done by testing each target with the ARROW chip individually. First, targets labelled with single colors are tested. Beads with *E. coli* targets labelled with dark red fluorophores are introduced in the LC waveguide. The MMI waveguide is excited with 738 nm wavelength light. Fig 3.3a(i) shows the fluorescence signals from *E. coli* targets. The black dotted line represents the threshold for detecting a target, defined as the highest background level when the waveguide is excited by all three lasers (8 counts/10μs) but with no fluorescent targets. Zooming in on to one of the events shows a signal of the bead with six peaks which

corresponds to the excitation pattern generated by the MMI waveguide (fig 3.3a(ii)). For automated target identification, the signals from individual beads are assessed using eq 3.1

$$S(t,\delta t_C)_C = \left\{ \prod_{i=0}^{N_C-1} F(t - i \cdot \delta t_C) \right\}^{\frac{1}{N_C-1}} \qquad 3.1$$

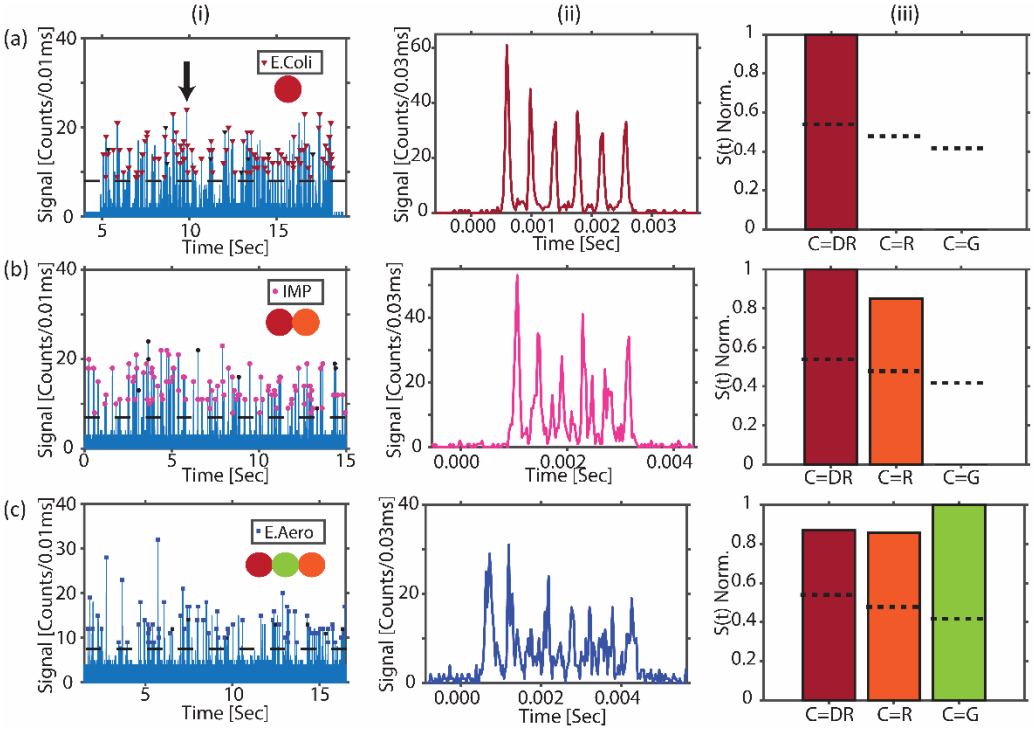


Fig 3.3 a) E. coli detection. i) Fluorescence signal of beads with E. coli targets labeled with dark red fluorophores excited by MMI waveguide. ii) Zoomed-in signal of a single bead. iii) Bar histogram map of a correctly identified E. coli signal. b) and c) same analysis for IMP and E. aerogenes targets.

F(t) is the measured fluorescence signal and N_c is the number of spots generated by the MMI waveguide for different colors. The product in eq 3.1 represents a "shift-multiply" approach to process the signal. F(t) is shifted repeatedly by the characteristic time spacing δt_c for a given pattern. If a particular spot number is present in the signal, this process will result in a large S(t) value. The total time of an event ΔT is found from the start and end of an event signal using a peak finding algorithm (fig 3.4a). The velocity of each target is calculated from the total time ΔT taken by the target to travel the 75 μm wide MMI waveguide intersection. δt_c is then

calculated using the distance between adjacent spots δX_C (fig 3.4b) generated by the MMI waveguide for the three excitation wavelengths (eq 3.2)

$$\delta t_C = \frac{\Delta T \cdot \delta x_C}{75\mu m} \qquad 3.2$$

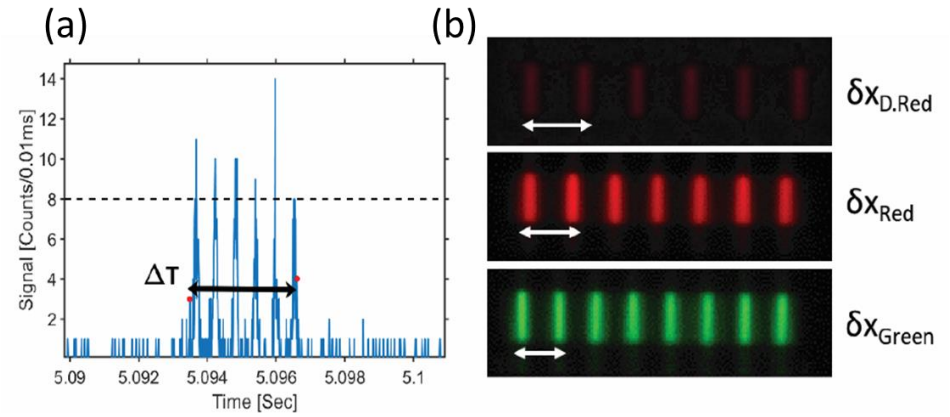


Fig 3.4 a) Signal from MMI waveguide excitation b) distance between adjacent spots of the pattern generated by the MMI waveguide

By calculating S(t)c for each N_c, a map is generated showing which color channels dominate above set thresholds. Thus, indicating the corresponding color code and uniquely identifying the target captured on the bead. Fig 3.3a(iii) shows the S(t) map of a correctly identified *E. coli* signal of fig 3.3a(ii) with S(t) dominating only in the dark red channel of the algorithm.

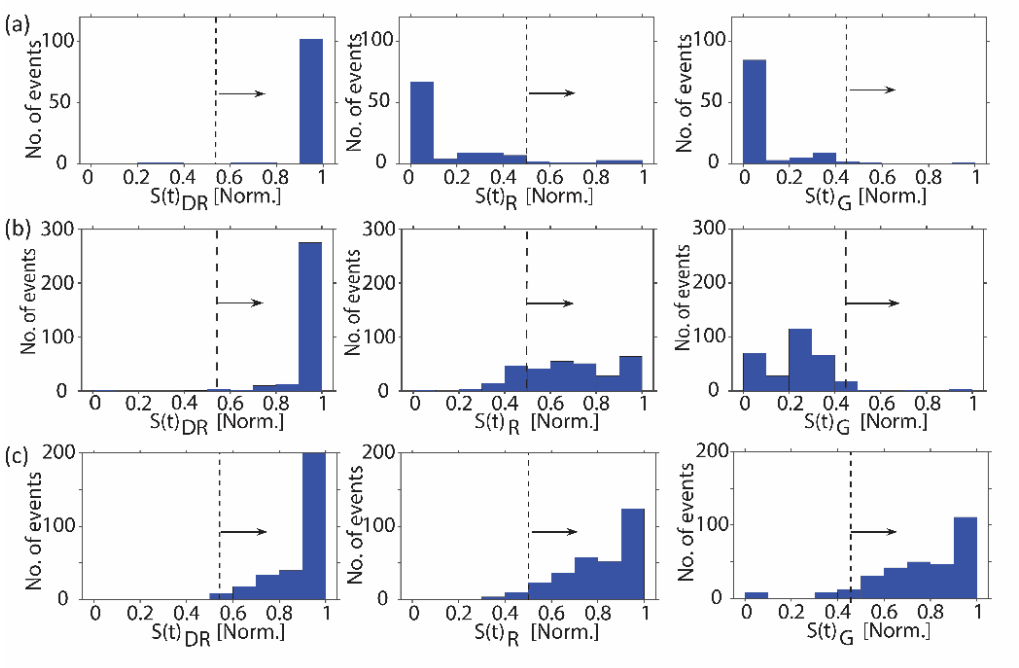


Fig 3.5 Histogram of $S(t)_c$ values of all the detected signals from E. coli targets and b) & c) are from IMP and E. aerogenes targets

Fig 3.5a shows the $S(t)_c$ values of all the detected *E. coli* signals plotted in a histogram. The dotted vertical line indicates the threshold set for each channel defined as the average $S(t)_C$ value plus one standard deviation of signals from individual experiments of all seven targets. A correct *E. coli* signal will have only $S(t)_{DR}$ above the threshold. Fig 3.6 shows the map of an E. coli target signal incorrectly identified as a red tagged target. Of all the analyzed events 91.6% of the signals had $S(t)_{DR}$ above the threshold and $S(t)_R$ and $S(t)_G$ below the threshold. A few signals marked with a black symbol in fig 3.3a(i) were the incorrectly identified fluorescence signals. Similar experiments were also done for the other two single color tagged targets (KPC and VIM), which were detected with an average accuracy of 90%.

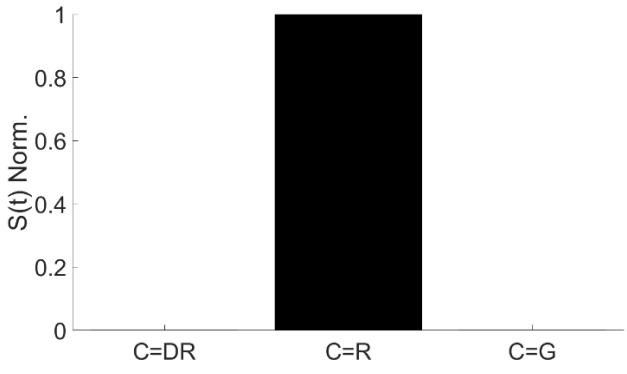


Fig 3.6 A map of an *E. coli* target incorrectly identified as KPC because of dominant $S(t)_R$ value

3.3 Multi color tagged target identification

Next, multi-color labeled targets are analyzed individually. As an example, fig 3.3b(i) shows fluorescence signals from an experiment where beads captured with IMP targets, labeled with red and dark red fluorophores are flowed through the LC waveguide and the MMI waveguide is excited simultaneously with 633 nm and 738 nm wavelength lasers. Fig 3.3b(i) depicts similar signals but by a three-color labeled target. In this case, *E. aerogenes* targets labelled with dark red, red and green fluorophores and captured on beads are introduced in the ARROW chip and detected by exciting the MMI waveguide simultaneously with all three lasers. Fig 3.3b(ii) and fig 3.3c(ii) shows the signals from individual targets. While signals from single color tagged targets can be identified by counting the number of peaks, the signals from multi-color tagged targets are the superposition of the patterns corresponding to their color codes. Eq 3.1 should be used to generate S(t) maps for these signals to get the target information. The map for a signal from IMP target shows the signal to have dominant $S(t)_R$ and $S(t)D_R$ values where a signal from an *E. aerogenes* target shows up in all three channels of the map. This is shown in fig 3.3b(iii) and 3.2c(iii). Analyzing all the events from experiments where IMP and *E. aerogenes* targets are tested, an average of 90% events were correctly identified. Similar analysis was also done on signals from testing the targets with the two other remaining color combinations, NDM with green and red tag and *K. pneumonia* with green and dark red tag. Targets were

detected at an average rate of 5.60 events/sec with an SNR of 36 (background noise of 0.39 counts/10μs) and 85% accuracy. This demonstrates the ability of the chip to rapidly detect single colored and multi colored targets with good sensitivity and reasonable accuracy.

3.4 Analysis of false signals

Target	DR	R	G	DR-R	R-G	G-DR	DR-R-G	Total
E.Col		2.8	0	3.7	0.0	0.0	1.8	8.3
KPC	3.7		1.8	1.8	0.0	0.0	1.8	9.1
→ VIM	2.0	0.6		1.7	2.0	3.4	7.8	**17.5**
IMP	6.5	0.6	0.3		0.0	0.0	3.0	10.4
→ NDM	0.5	0.0	10.5	0.0		0.5	8.0	**19.5**
→ K.Pne	4.0	0.0	0.8	1.0	1.6		6.8	**14.2**
E.Aer	1.0	0.3	2.6	3.1	1.2	1.9		10.1

Table 3.3

Table 3.3 shows the percentage of false signals from each target corresponds to which color combinations. For example, of all the signals detected from dark red tagged *E. coli* targets, 2.8% of them were identified incorrectly as red color signals, 3.7% as dark red-red and 1.8% as signals of dark red-red-green color combination (data entry in the first row of table 3.4). Thus, a total of 8.3% of all the detected signals were identified incorrectly. The table indicates that signals from targets tagged with green fluorophores were the ones which had highest percentage of signals identified falsely (namely signals VIM, NDM and *K. pneumonia* targets), with most of them detected incorrectly as signals of dark red-red-green color combination.

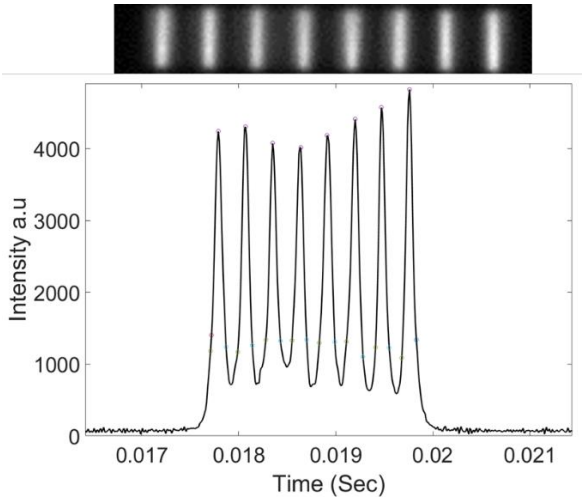


Fig 3.7 Intensity distribution mimicking an ideal signal produced from particle excited by MMI waveguide using 556 nm wavelength

Fig 3.7 shows the horizontal profile obtained from the intensity distribution of the top down optical image of the pattern generated by the MMI waveguide in the LC waveguide when excited by 556 nm laser. Using the average flow speed of the particles (34 µm/ms and a pixel to distance calibration conversion of 0.550 µm/pixel) the intensity distribution of the pattern is plotted in time scale. This would mimic an ideal signal a fluorescent particle flowing through the LC channel would produce when excited by the MMI pattern. Applying the signal processing algorithm (eq 3.1) on this signal (fig 3.8a) shows that apart from a dominant $S(t)_G$ value, the signal also has comparably high values in the red and dark red channel. This could lead to a false identification of the signal to be encoded with a color combination of dark red-red-green. As the wavelength that excites the MMI waveguide decreases, the number of spots the MMI waveguide generates increases. Thus, the excitation spots are squeezed closer together to confine them within the waveguide core. This leads to slight overlap between the spots leading to higher background noise valley. Applying eq 3.1 on this signal shows it leaking into the dark red and red channel of the algorithm. This explains, why signals from targets tagged with green fluorophores are identified with higher error. Fig 3.8b shows the same signal modified to have

zero background noise valley. The S(t) map from the modified signal shows a clear dominance in the green channel with zero leakage of the signal to the other two channels.

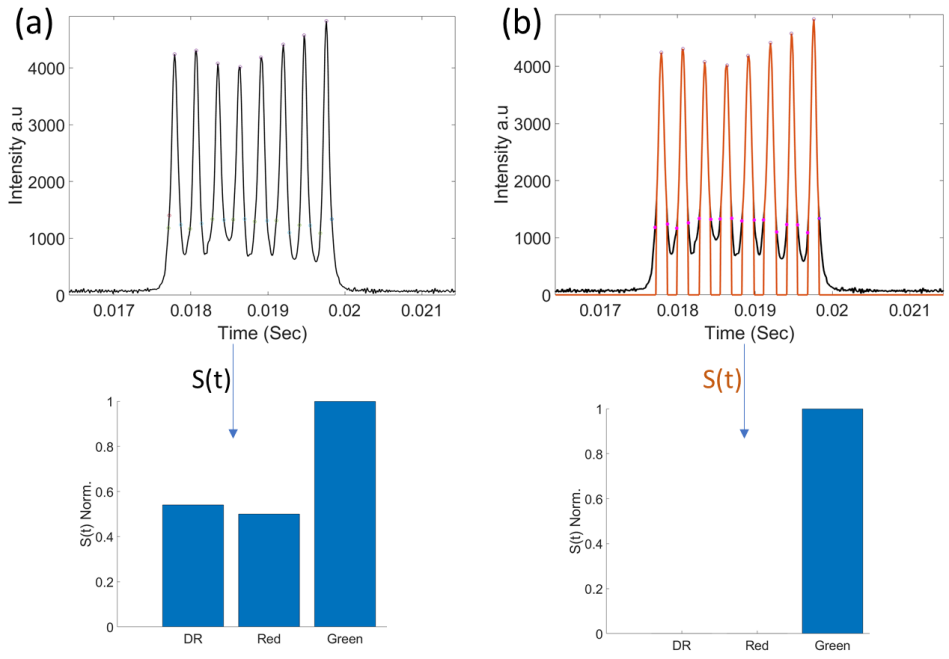


Fig 3.8 a) S(t) map of an ideal signals generated by the MMI waveguide. b) The same signals with background corrected to zeros.

3.5 7x multiplexed detection

For the full multiplexed assay, equal concentrations of all seven targets were mixed and flowed through the chip. The MMI waveguide is now simultaneously excited with 738 nm, 633 nm and 556 nm lasers. The signals from all seven targets collected by the APD are demultiplexed by processing each signal using eq 3.1 and generating the $S(t)_C$ map. Based on which colors dominate in the map, the spectral information in the signal is decoded and thus, the target it corresponds to is identified. Fig 3.9 shows the fluorescence signal trace with all seven targets simultaneously detected.

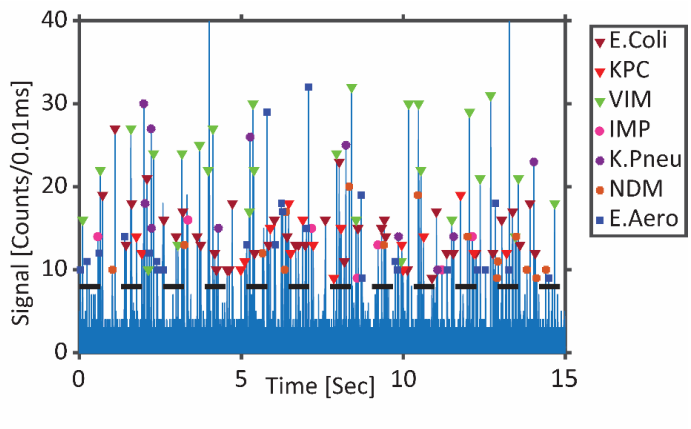


Fig 3.9 Fluorescence signal from all seven targets flown together in the LC waveguide and excited by the three lasers simultaneously.

An average of 1.8±0.7 x 10^6 beads/mL are detected which is about 70% of the expected concentration. While preparing the beads with fluorescent tagged targets, an incremental ratio of 1:10:30 (bead: target: fluorescent-probe) was used to saturate each element of the bead. However, only a fraction of the binding sites of the magnetic bead is hybridized with the target-fluorescent probe complex due to inaccuracies in concentration and steric hindrance between targets captured on the bead. The accuracy of the signal processing algorithm depends on the quality and strength of the signal. To ensure maximum precision of the signal processing algorithm, a very conservative threshold (8counts/10µs) was used to pick only signals above the highest background photon count. Thus, some signals with lower signal strength are visible below this threshold, but are not counted (shown in fig 3.10). This accounts for the difference in detected and expected concentration of the beads in the above experiment. In the future, other signal decomposition techniques such as wavelet transformation can be used to extract low intensity signals close to the background level [44,45].

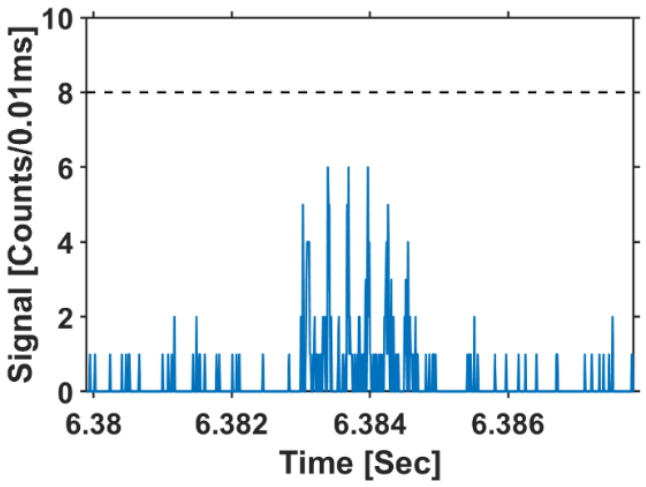


Fig 3.10 A fluorescence signal from *E. coli* target, below the set threshold.

4 Spatial multiplexing: Single molecule sensitive 3x multiplexed detection of antibiotic resistant bacterial plasmids

Apart from spectral multiplexing, MMI waveguides can also be used for spatial multiplexed detection. This is achieved by designing the MMI waveguide to generate different number of replicas of the field of its input excitation waveguide at different lengths. This chapter describes how the spatial multiplexing capability of the MMI waveguide can be employed for simultaneous detection of multiple antibiotic resistant bacterial plasmids with single molecule sensitivity.

The current recommended tests by the Clinical Laboratory and Standards Institute (CLSI) for detection of antibiotic resistant bacteria are mainly phenotypic in nature or using molecular based diagnostic techniques [46,47]. Disk diffusion test and Hodge test are the main examples of phenotypic tests (Fig 4.1). In these tests, the bacterial cells are cultured in a growth medium plate. The growth medium is laced with a particular antibiotic against which the bacteria's resistance is to be tested. In the case of disk diffusion method, the bacterial cells are grown in an agar plate [48,49]. A filter paper disk coated with a specific concentration of the antibiotic is kept on the surface of the agar plate. As the antibiotic radially diffuses through the agar plate, a concentration gradient of the antibiotic is created (logarithmically decreasing in outward direction). The bacteria that is not inhibited by the antibiotic will continue to grow till the area where the concentration of the antibiotic is inhibitory. Thus, a growth zone around the disk is formed. Quantitative assessment of the resistance of the bacteria is done by measuring the zone diameters and compare the results with previous studies. The Hodge test also involves a similar technique, where streaks of the test bacteria (that is to be tested for resistance) are drawn on a growth medium, around the above mentioned antibiotic laden disk [50,51]. The growth medium also has a dummy-bacteria sample such as *E. coli* all over the surface. Based on whether the test bacterial strain can produce enzymes that inhibit the antibiotic and allow more growth of the *E. coli* towards the disk a characteristic cloverleaf-like indentation is

observed. Assessment of antibiotic resistance of the test bacteria is made by observation of the clover-leaf pattern.

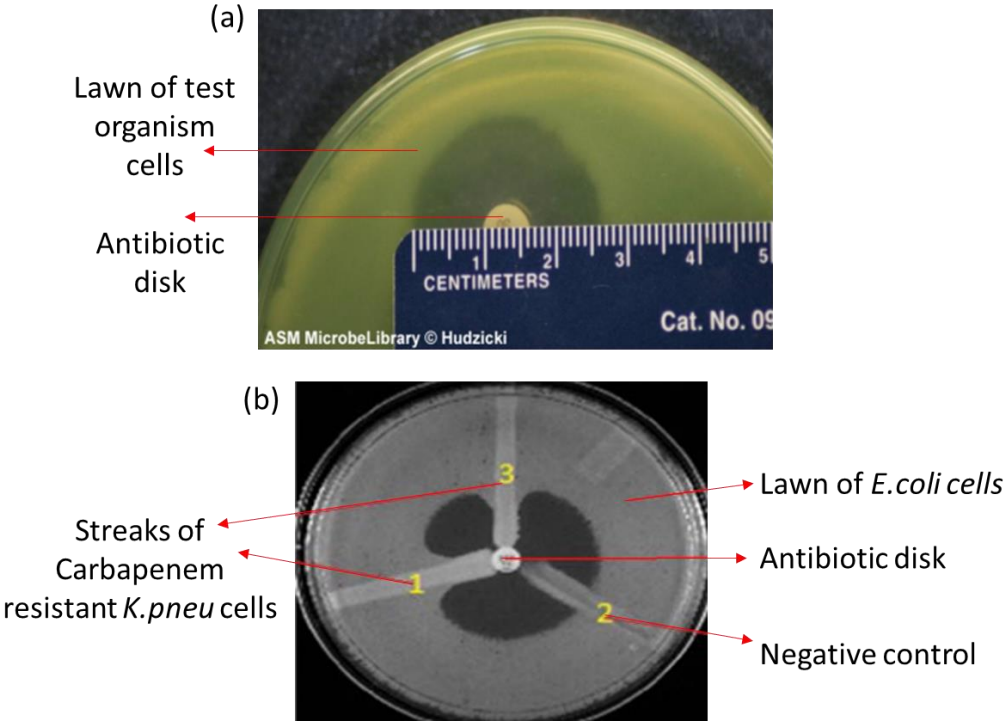


Fig 4.1 a) Disk diffusion test: Antibiotic resistance is assessed by measuring the diffusion diameter till where the cell growth is inhibited [49]. b) Hodge test: Antibiotic resistant bacteria (1&3) allow template *E.coli* cells to grow closer to the antibiotic disk (Dark region corresponds to no cell growth) [50].

Since screening of antibiotic resistance using phenotypic tests is done by overnight incubation of cells and measuring the growth patterns, these tests are time consuming and neither highly specific nor sensitive [52,53]. They have known to be not reliable when it comes to testing bacteria that show strain-to-strain growth rate variability and also give false positive results for bacterial species with carbapenem resistance [48,54]. Molecular based diagnostic tests such as direct gene sequencing or PCR give far more accurate and sensitive results [55-57]. But these methods rely on target amplification and require laborious sample preparation steps to avoid false results due to contamination from blood or serum. As mentioned in the introductory chapter, microfluidics has been used to build chip scale devices which can perform such complex tasks. A few examples of such devices that have demonstrated exceptionally precise

handling of fluids and combining reagents are droplet microfluidics [58] and micro actuator-based sample processing chips [59]. But they all rely on an external sensing device, mainly a top down optical image-analysis based detection scheme. Also due to emergence of multiple genes coding for resistance against an antibiotic, it is important to develop detection platforms that can perform multiplexed measurements.

The ultimate goal of a diagnostic system towards detection of antibiotic resistance, is to perform the task via a complete sample-to-answer measurement in a short period of time. Here, two sample processing instruments are described which allows target specific extraction of three different carbapenem antibiotic resistant bacterial plasmids (KPC, NDM and VIM) from *E. coli* cells spiked in whole human blood. A spinning hollow disk is used to separate bacterial cells from whole human blood [60,61]. A microfluidic chip with monolithic column is used to target specifically extract the bacterial plasmids having the antibiotic resistance mutations [62,63]. The sample processing units are complimented with the ARROW based biosensor chip [64]. The MMI waveguides in the biosensor chip enables amplification free detection of these plasmids simultaneously using spatial multiplexing [65]. Each component of this system is chosen to minimize the analysis time with a goal of keeping the sample extraction and detection time less than 2 hours.

4.1 Spinning hollow disk for bacterial cell separation from whole blood

Sample preparation in a clinical setting usually starts by separating potential antibiotic resistant bacterial cells from whole human blood. This is a very critical step to be done before extracting the DNA from the bacterial cells. This reduces contamination from non-specific targets such as human DNA and blood cells while doing target specific plasmid extraction and molecular based diagnostic tests. Bacterial cells and blood cells have contrasting sedimentation coefficients due to their differences in density and size. The sample separation hollow disk device uses quick application of centrifugal force to separate these particles by their contrasting sedimentation velocities. The hollow disk device and related experiments were developed and done by Pitt's

group from BYU [60]. The disk is 12 cm in diameter and can separate bacteria from 7 mL of whole blood per run. The disk spins around a central axis, has a bowl-shaped surface which slopes downwards to the center of the disk and has an annular fluid collection vestibule at the edge (Fig 4.2a). The vestibule has an upper chamber bounded with a partial lid and a trough below this chamber. The trough is separated from the bowl by a retaining weir. 7 mL of blood spiked with $5x10^6$ CFU/mL of *E. coli* DH5α cells containing pUC19-KPC plasmids (pUC19 template plasmids transcribed with KPC mutation) and 1.5 mL of buffer is placed in the bowl and rapidly spun. The sample is pushed radially out and thrown into the vestibule, spreading it over a larger surface area, spreading the blood into a very thin layer (about 2.5 mm thick and 9 mm wide) which is much smaller than the length that blood cells must travel during centrifugation techniques using test tubes. This enables quick separation of the cells with a run time of 2 mins. The large discoidal blood cells, which have a higher sedimentation coefficient (24–27 times larger), sediment to the back wall of the vestibule much faster than the rod-shaped and smaller bacterial cells, thus forming a dense cell pack. The plasma is pushed out towards the central axis of the disk as the blood cells pack at the wall, creating a two-layer system. The smaller bacterial cells get caught with the flow of the plasma and migrate towards the center of the disk. At the time when 99% of the blood cells have reached the cell pack at the wall, about 20% of the bacteria are also trapped in the cell pack and are not recoverable. The disk is then decelerated carefully to avoid mixing of the clear plasma with the blood cell pack. The dimensions of the trough and thickness of the weir were designed so that when the disk comes to a stop, the blood cell pack falls down into the trough and is held back by the weir whereas the plasma with the bacterial cells flow over the weir into the bowl region (Fig 4.2b).

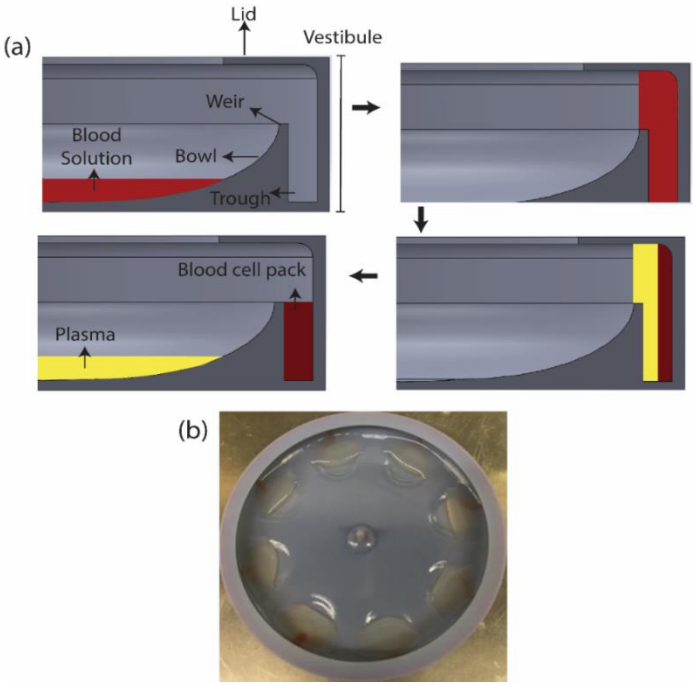


Fig 4.2 a) Cartoon depicting the cross section of the sample separation hollow disk device showing the bowl region and the vestibule. The different steps the blood goes through when the disk is spun is shown. b) Top down photograph of the hollow disk with separated out plasma in the bowl.

4 mL of plasma with an average of 5.25×10^6 CFU/mL of bacteria which corresponds to 60% recovery is obtained after separation. Any remaining blood cells are lysed and the DNA from the cells are extracted using standard magnetic bead-based extraction protocols. 50 µL of 0.12 ng/µL of DNA is recovered after the whole procedure. The recovered bacterial DNA is sonicated to randomly break the circular plasmids.

4.3 Monolith based microfluidic chip for target specific elution of antibiotic resistant plasmids

Molecular based diagnostic tests achieve accurate test results with less false negatives by incorporating target specificity. One of the most common way this is done on a chip scale device is by surface functionalizing a part of the chip to capture a specific target. This is achieved here using a polypropylene based microfluidic sample processing device which has a DNA-functionalized porous monolith polymerized inside the channel (Fig 4.3a). The monolith-

based chip and the sample extraction experiments were done by Woolley's group from BYU [62], but can also be done off chip using magnetic beads. The microfluidic chip is made using hot embossing to transfer (500µm x 500µm) microfluidic channels using a CNC machined aluminum master on a 2 mm thick polypropylene sheet. A porous monolith column is polymerized inside a part of the microfluidic channel by UV curing an acrylate-based polymerization mixture (Fig 4.3b).

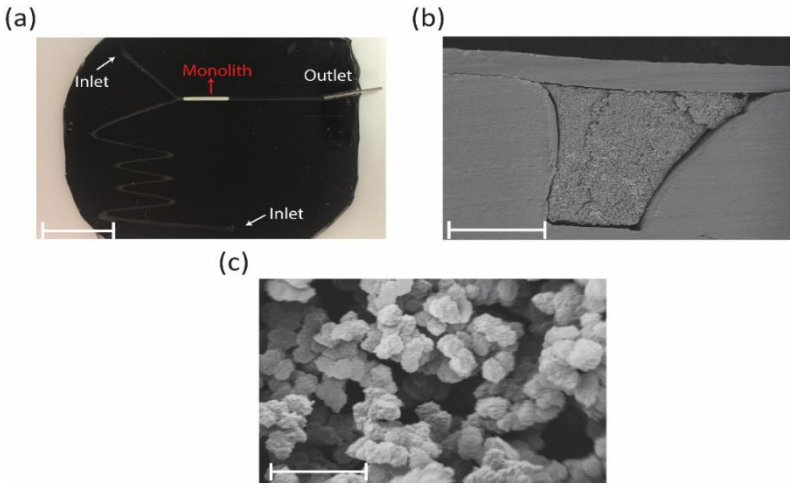


Fig 4.3 a) Top down photograph of the microfluidic chip with monolith column. b) SEM image of the polymer monolith. c) Zoomed in image of the monolith showing its porosity. (Scales: 1cm, 500 µm, 5 µm respectively)

The fragmented DNA extracted from *E. coli* cells using the spinning hollow disk is flown through one of the inlets of the microfluidic. A heater kept below the serpentine channel of the chip denatures the DNA. The next part of the chip, the monolith column, is DNA-functionalized with commercially synthesized acrydite-modified capture-oligonucleotides. The sequence of the capture-oligonucleotides is designed to be complementary to the particular resistance mutation transcribed on the pUC19 plasmid (for example pUC19-KPC) (Capture sequences for each plasmid is shown in table 4.1). The large contact surface area of the monolith enables sequence-specific capturing and elution of antibiotic-resistance plasmids with short incubation times. Measurements from the SEM data indicate an average nodule size of 1.2 ± 0.2 µm and pore size of 2.0 ± 0.4 µm (Fig 4.3c). This ensures that the denatured target DNA follows a

tortuous path through the monolith with more contact surface area, increasing the likelihood of capture via hybridization. This is absent in other microfluidic chips which uses functionalized flat substrates or particles to capture targets, requiring them to have hour long incubation time periods. The monolith goes through multiple rinse cycles to wash off any unbound non-specific DNA targets. The captured antibiotic resistant plasmids are then released thermally and eluted at the outlet of the chip in fractions of 35 µL. Elution of captured plasmids are confirmed via qPCR. C_t values of the two "rinse aliquots" preceding the subsequent two "elution aliquots" are compared. The mean difference in C_t values before and after elution was 2.3. In qPCR, C_t values have an inverse, logarithmic relationship to DNA concentration. For captured plasmid fractions, C_t values are lower than the pre-elution numbers, indicating a higher concentration of the target DNA sequence during elution than before, which is consistent with specific DNA capture and enrichment. The remaining of the thermally released plasmids are fluorescently tagged with 1 µM POPO-3 nucleic acid staining dye. The staining dye has high affinity to nucleic acids and becomes fluorescently activated up on binding with the plasmids. Each plasmid is size based tagged with multitude of such fluorophores thus emitting bright fluorescent signals when excited with a light source. Three separate sample processing chips are fabricated to selectively capture and elute pUC19-KPC, pUC19-NDM and pUC19-VIM plasmid fragments.

KPC, NDM & VIM sequences:

1. KPC-3 (CDC antibiotic resistance isolate bank reference number 0112):

   ATAGCGGCAGATCAAGACGACAGAACACTTAATGGTGTAATTTCTATAGACGTAGCAGCGCCTTGGTAAGCGATTTGAGCTTGCCTTGAAAC

2. NDM-1 (CDC antibiotic resistance isolate bank reference number 0118):

   CGTCGTGTGAAGGATAGAGCTGTACGGCCCAAAGCCCCGTCAGCGAAGGTTGCCAAACTAGCAGTCCCTAC

3. VIM-1 (CDC antibiotic resistance isolate bank reference number 0135):

   AGCCYCTCCAGGCYCAAATGGTCTTTAATGGTGTAATTTCTATAGACGTCACAAACCAGCGTATAGCGTTGCGTCAGCAAACT

KPC, NDM, VIM Capture sequences:

KPC: 5'-TATCGCCGTCTAGTTCTGCTGTCTTG-3'; Tm = 68 ºC

VIM: 5'-TCGGAGAGGTCCGACTTTACCAGA-3'; Tm = 67 ºC

NDM: 5'-GCAGCACACTTCCTATCTCGACAT-3'; Tm = 65 ºC

Table 4.1 KPC, NDM and VIM mutations transcribed in pUC19 plasmids and the corresponding capture sequences

4.3 Spatial multiplexing with ARROW biosensor device

The antibiotic resistant plasmids extracted from the sample processing units are detected using the ARROW biosensor platform. For detecting pUC19-KPC, pUC19-NDM and pUC19-VIM simultaneously, the MMI waveguide's ability to generate different number of replicas of the input field at different lengths (given by eq 4.1) using a single excitation wavelength is utilized. To use this feature, a single MMI waveguide in the ARROW platform is designed to intersect three different LC waveguides named as channel 1, channel 2 and channel 3 (Ch1, Ch2, Ch3). The inlets of the three LC waveguides start at separate positions and merge together to a common outlet after intersecting the MMI waveguide (fig 4.4a).

$$N_j L_j = \frac{n_c w_{eff}^2}{\lambda} \qquad (4.1)$$

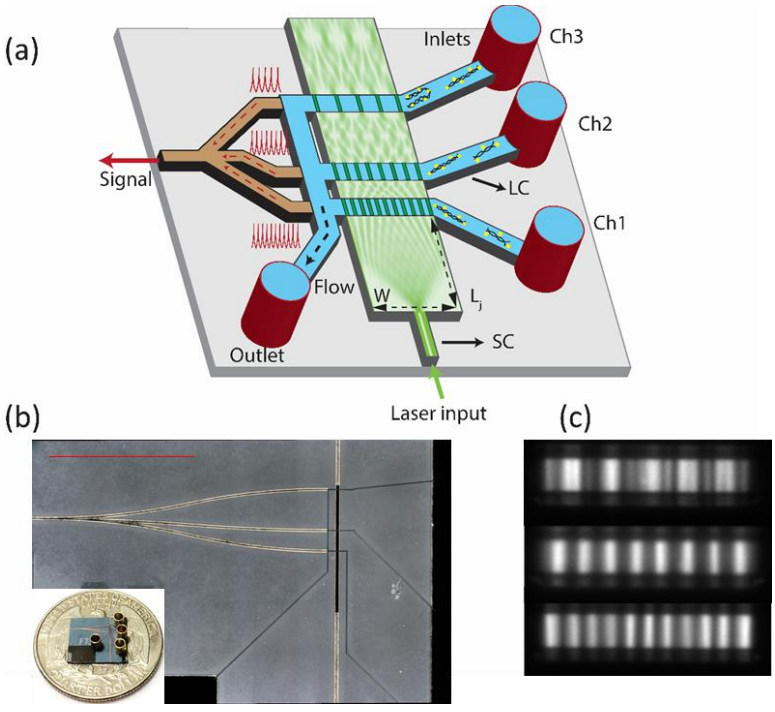


Fig 4.4 a) Cartoon depiction of the ARROW biosensor chip showing the interference pattern made by the MMI waveguide. b) Top down microscope image of the chip, scale bar: 5mm (inset: comparison with a US quarter). c) Fluorescence image of the excitation pattern of the MMI waveguide in the three LC waveguides.

The positions of the LC waveguides are designed to intersect the MMI waveguide at specific lengths (L_1, L_2, L_3) such that the LC channels get excited by the corresponding spot patterns generated by the MMI waveguide. Here, MMI waveguide of refractive index n_c = 1.460 and width w = 75 µm intersects the LC channels at L_1 = 1676 µm, L_2 = 2243 µm and L_3 = 3350 µm to generate eleven, eight and five spots when excited by a 556 nm light source. Fig 4.4b shows the spot patterns produced by the MMI waveguide in Ch1, Ch2 and Ch3 (bottom to top). 4 µL of plasmids tagged with nucleic acid staining dye is flown in the three LC waveguides. The signals from the samples flowing through each of the three LC waveguides are separately collected by three collection SC waveguides and sent to a single avalanche photo detector (APD) using a single output waveguide via a 3x1 Y-coupler waveguide geometry. A band pass filter kept outside the chip, before the APD, blocks any scattered excitation light source. Similar to the application described in chapter three, based on the channel in which the target is flowing, the specific interference patterns generated by the MMI at the different lengths L_1, L_2 and L_3 is encoded in the time domain fluorescence signal. The “shift and multiply” algorithm described in the previous chapter is used to decompose the signals and decipher them. This allows detection of three different targets flowing in the three separate channels of the chip simultaneously.

4.4 Detecting individual plasmids using ARROW biosensor chip

Antibiotic resistant plasmids eluted using the monoliths are fluorescently labeled with nucleic acid staining dye. The dye molecule non-specifically binds with the DNA. The dye gets fluorescently activated upon binding with the nucleic acid. The larger the size of the DNA the more dyes are tagged on to it, thus emitting bright fluorescence signals when excited by the ARROW waveguide. pUC19-KPC plasmids are assigned to Ch1, pUC19-NDM to Ch2 and pUC19-VIM to Ch3. To test the ability of the ARROW biosensor to accurately detect antibiotic resistant plasmids with single molecule sensitivity, each type of plasmid is tested individually by exciting with the MMI waveguide.

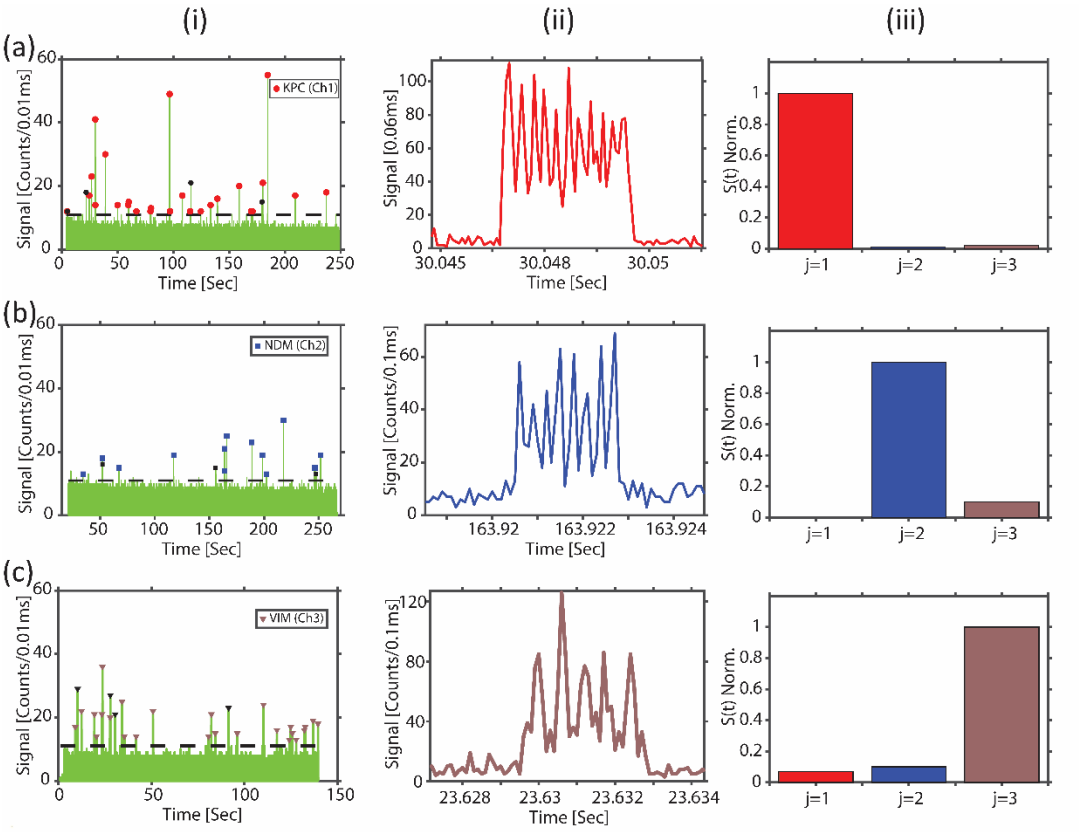


Fig 4.5 a.i) Fluorescence signals from individual pUc19-KPC plasmids flown in Ch1. a.ii) Zooming into an event shows a signal with eleven peaks. a.iii) The S(t) map of a correctly identified KPC signal

pUC19-KPC plasmids tagged with POPO-3 dye is flown in Ch1 and buffer with the dye in the other two channels. The MMI waveguide excites the KPC plasmids and generates signals from individual plasmids with eleven peaks. The fluorescence signal from individual KPC plasmids is shown in Fig 4.5ai. Negative controls were done by running non-complementary plasmid targets in a monolith microfluidic chip (Ex: VIM plasmids run in monolith chip functionalized with KPC capture probes, KPC plasmids run in monolith chip functionalized with NDM capture probes and NDM plasmids run in monolith chip functionalized with VIM capture probes). No fluorescence signal is observed from the negative control experiment (Fig 4.6). The

background threshold for the signal was set as 11 counts/10μs which was the highest signal from the negative controls. Photon counts above this set threshold in fig 4.5ai are defined as signals from individual KPC plasmids. Zooming into one of such events shows a signal with eleven peaks, corresponding to the excitation pattern of the MMI waveguide in Ch1. A signal processing algorithm (eq 4.2) is used to identify all the plasmid signals. F(t) is the time domain fluorescence signal of a single plasmid which is shifted in time domain by a characteristic time δt_j and multiplied N_j number of times (N_j: number of spots in the excitation pattern of the MMI). δt_j is the time taken by the plasmid to travel between two adjacent excitation spots. A map of the S(t) values at the three channels is made for each detected event. If a particular spot number matches with the pattern of the fluorescence signal, the algorithm gives rise to an enhanced S(t) value in the channel corresponding to that pattern. The S(t) value is normalized with σ, defined as the average background fluctuation, to account for any undesirable signal enhancement.

$$S(t,\delta t_j)_j = \left\{ \prod_{i=0}^{N_j-1} \frac{F(t - i\cdot\delta t_j)}{\sigma} \right\} \qquad 4.2$$

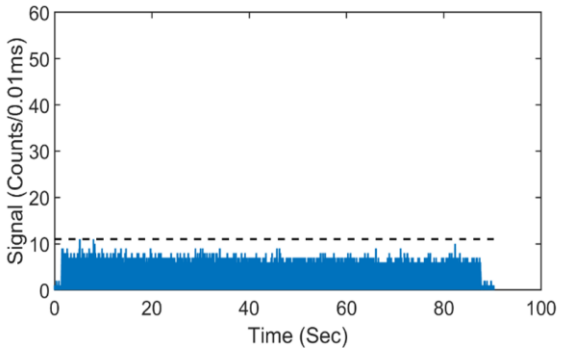


Fig 4.6 Fluorescence signal from negative controls

The fluorescence signal is correctly identified based on which channel S(t) value dominates. Fig 4.5aii shows the S(t) values of a correctly identified pUC19-KPC plasmid. The signal has highest S(t) value in channel one with N_1 = 11. Analyzing all the events from the fluorescence

trace of KPC plasmids shows that, most of the events are distributed with very high S(t) value in channel one (marked in red dotted box in fig 4.7) and low values in the other two. Similar single-plex experiments done with pUC19-NDM and pUC19-VIM plasmids generated signals from NDM with eight peaks and VIM signals with five peaks corresponding to the MMI pattern generated in the respective channels (fig 4.5b & 4.5c). The signals were identified with and average accuracy of 87%. Signals from all the three channels were detected with similar efficiency with an average SNR of 12.2.

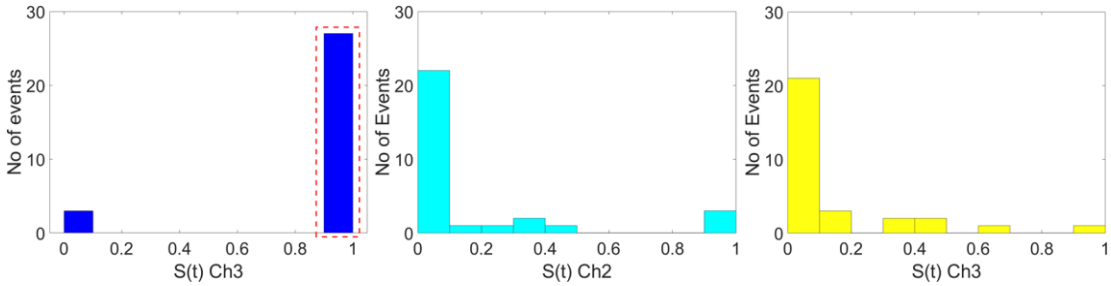


Fig 4.7 Histogram of S(t) values of all the detected KPC events

4.5 Simultaneous detection of all three antibiotic resistance plasmids

Fluorescently tagged pUC19-KPC, pUC19-NDM and pUC19-VIM plasmids are simultaneously flown through Ch1, Ch2 and Ch3 respectively. When excited by the MMI waveguide, the targets generate signals with eleven, eight and five peaks based on which channel they are flowing. Signals from all the three different targets are collected by the 3x1 Y-coupler collection waveguide and detected by the APD. Fig 4.8 shows these signals correctly identified using eq 4.2. This allows multiplexed detection of the three plasmids without decomposing them using off-chip signal decomposition elements. The events with dominant $S(t)_1$ value is from KPC targets, as shown in the S(t) distribution in fig 4.9. Signals dominant in Ch2 and Ch3 are from NDM and VIM targets respectively.

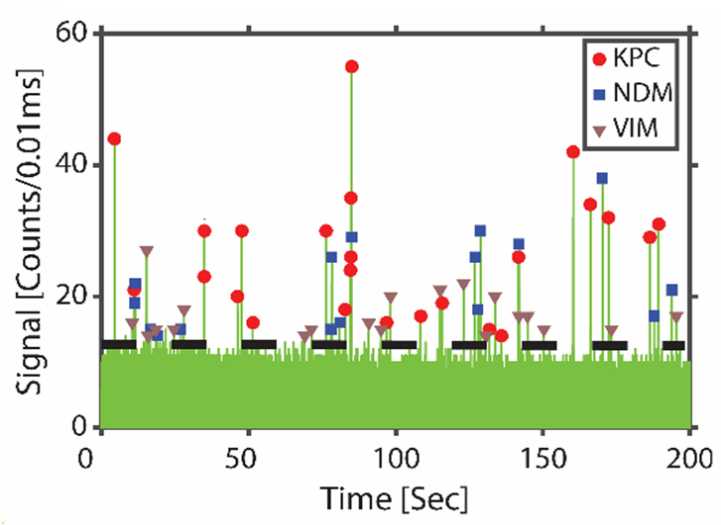


Fig 4.8 fluorescence signals from pUC19-KPC, pUC19-NDM, pUC19-VIM correctly identified

The plasmids were detected at a rate of 17 events/min with an average signal strength of 20±7 photon counts/10µs. The targets while flowing through the LC channel have a broad distribution in their cross-sectional position. The ones positioned in the middle of the LC channel are more efficiently excited by the excitation spots of the MMI waveguide and the signal generated by them are well coupled to the LC core waveguide optical mode. Whereas the ones positioned near the corners are excluded as the optical mode overlaps less. This along with the distribution in the particle's velocity accounts for the fluctuations in the fluorescent signals. Nevertheless, signals were detected by the chip with an average SNR of 13, with a maximum of 37. Thus, enabling rapid detection and identification of targets within eight minutes. Using the dimensions of the excitation volume (height x width: 2.45 µm x 12 µm) and the average speed of the particles (described in chapter 3), an average of 2.0 ± 0.6 x 10^6 copies/mL of KPC and VIM plasmids and 9.0 ± 2.0 x 10^5 copies/mL of NDM plasmids were detected. The ARROW sensor is sensitive enough to directly count individual plasmids. Thus, the concentrations estimated from the fluorescence signals can be used for quantitative analysis of the targets. This has been demonstrated before for single-plex detection of Ebola RNA with over six logs of dynamic range.

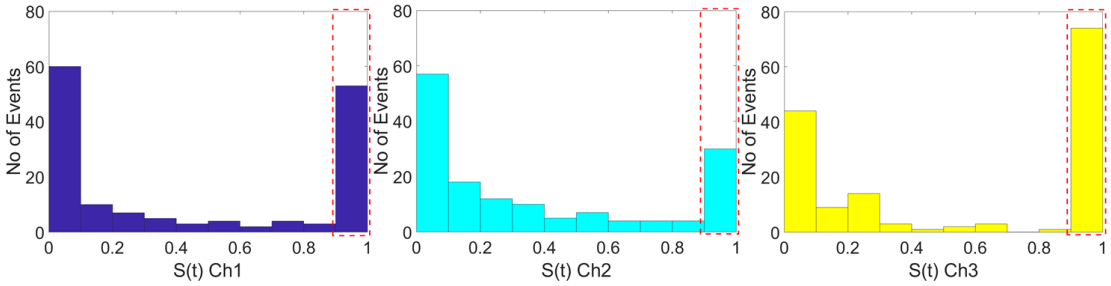


Fig 4.9 Histogram distribution of the $S(t)_j$ values of all the events detected from fluorescence signal shown in fig 4.8. Events are deciphered as that of KPC, NDM or VIM based on which channel S(t) is most dominant (marked in red dashed box)

Thus, by combining the two sample preparation elements with the sensitive ARROW biosensor, amplification free multiplexed detection of three antibiotic resistant plasmids with single molecule sensitivity is achieved for the first time. The two sample preparation units enable target extraction from template *E. coli* cells spiked in whole human blood thus enabling to mimic clinical scenarios. The full sample-to-answer system took about 80 minutes to analyze three targets, with 40 minutes for cell separation, 30 minutes for monolith capture and elution of the plasmids and 8 minutes for optical readout. The optical performance of the ARROW sensor can be even further improved by enhancing the coupling between the signals of the sparsely distributed targets and the optical mode of the LC waveguide. This can be done either by fluid flow manipulations to focus the particle trajectory to the middle of the LC waveguide or by tuning the LC optical mode to spread and cover all of the LC cross-section more evenly which is described in the next chapter.

5 Multiplexed detection of SARS-CoV-2 RNA and antigen

Starting from December 2019, the world saw the rapid spread of the highly infectious sever acute respiratory syndrome coronavirus 2 (SARS-CoV-2). This caused the severe respiratory illness called Coronavirus-19 disease (COVID-19). Patients with COVID-19 show a very wide range of symptoms very similar to that of common cold or flu caused by influenza virus which makes symptom-based differential diagnosis hard [66]. The SARS-CoV-2 virus is a highly infectious pathogen that can destroy lung tissues and create inflamed air sacs filled with fluids, making it fatally hard to breathe [67,68]. SARS-CoV-2 has spread all over the world affecting more than 40 million people and as of November 2020, 1.2 million people have died due to COVID-19 disease, creating a global pandemic [69]. The virus is highly transmissible and spreads mainly through direct contact and droplets. Rapid testing implemented at a scale never seen before is essential to help health care providers tackle this pandemic [70]. The SARS-CoV-2 binds and fuses to the human cell membrane using its spike surface glycoprotein [71]. This allows the virus entry into the host cell and inject the viral RNA. The host cell is used to replicate the viral RNA. The RNA is translated to create the different viral proteins called antigens of which the RNA packaging nucleocapsid (N) protein is most profusely produced. New virus is formed using these proteins and released into the patient's body. When the virus starts infecting the body, the immune system responds naturally by creating proteins called antibodies. The antibodies are designed to bind to the surface proteins of the pathogens and disable them.

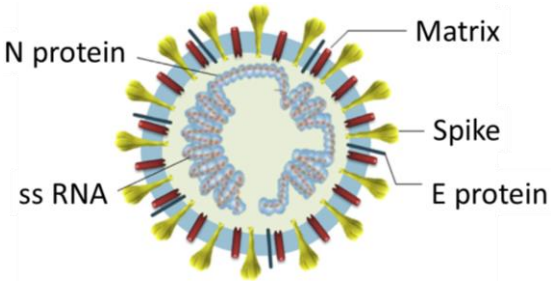


Fig 5.1 Cartoon of the SARS-CoV-2 virus [6]

Molecular diagnostics based on sensing either the viral RNA, antigen or antibody give the most sensitive detection of SARS-CoV-2 [72, 73]. Enormous resources are being invested by multiple major health care companies in developing and mass-producing SARS-CoV-2 specific diagnostic kits [74, 75]. Enzyme linked immunosorbent assay (ELISA) and Chemiluminescence enzyme immunoassays (CLIA) are examples of methods which use antigens for COVID-19 confirmation [76]. Several easy to use kits are now available in the market which use these immunoassays. They are fast and cheap serological tests, giving results within minutes and so are the preferred method for preliminary diagnosis. Immunoassays come with the cost of high limit of detection (LoD) of about 100pg/mL (10^8-10^9 copies/mL) and show low sensitivity [77]. Therefore, even when the patient presents the symptoms the test is prone to give false negative results with low concentration samples [78, 79]. Target specific amplification based, nucleic acid detection using reverse transcription polymerase chain reaction (RT-PCR) is considered as the gold standard test for SARS-CoV-2. RT-PCR target specifically amplifies even a small load of viral RNA through multiple reaction cycles to make them detectable. Several RT-PCR laboratory test kits are now available that show LoD as low as 10^2 genome copies/mL [80]. But they have long run time of more than an hour and involve complicated steps, require expensive tools, laboratories and trained technicians. The first initial days after the onset of the symptoms in a patient is when the virus load is high and at the peak of infection [81, 82]. The patient's body at this stage will have significant amount of SARS-CoV-2 specific viral RNA and antigens. Therefore, a combination of immunoassay based rapid antigen testing with confirmation of especially the negative results with nucleic acid-based testing is vital for early stage COVID-19 screening and quarantining [83, 84]. A multiplexed biosensing system capable of dual protein-nucleic acid detection would be ideal for this.

Because of the limitations of the current molecular diagnostic tests [85], a massive effort is put forth to either make PCR systems more portable and rapid or develop novel chip scale biosensors using other probing techniques, both electrical and optical. An example of a lab-on-

chip device aimed towards developing portable PCR units is the disk based “COVIDNudget” in which a sample kept in the middle is processed with PCR reagents kept in circumferentially distanced chambers [86]. Abbott’s ID Now is another commercially available widely used table top PCR based COVID-19 test [87]. On chip electrical sensing of SARS-CoV-2 has been demonstrated using antibody-based surface functionalized graphene field-effect-transistors [88] and by rapid sequencing using nanopores [89]. Reports have also been made on optical sensing of SARS-CoV-2 nucleic acids using surface plasmon resonance [90] and proteins using lateral flow immunoassays with fluorescence reporters [91, 92]. But none of the current methods can perform a multiplexed dual protein-nucleic acid detection.

This chapter describes how the ARROW biosensor platform integrated with MMI waveguides can be used to perform multiplexed dual protein-nucleic acid detection. A similar strategy as described in chapter 3 and 4 but now combining both spatial and spectral multiplexing technique are combined to simultaneously detect with single molecule sensitivity, SARS-CoV-2 RNA and protein spiked in nasopharyngeal (NP) swab. Amplification free single molecule sensitive detection of nucleic acids is achieved by tagging the target specifically eluted RNA molecules with multitudes of nucleic acid staining dye. While a novel target specific bright fluorescent reporter technique is used to tag individual antigens with a long template DNA having multiple fluorophores enabling single molecule sensitive detection of proteins as well.

5.1 Spatial-Spectral multiplexing using MMI waveguides

Chapter 3 and 4 describes how the MMI waveguides can be used to do spectral multiplexing and spatial multiplexing. For dual detection of proteins and nucleic acid, an ARROW device similar to that described in chapter 4 is used. A single MMI waveguide intersects two LC waveguides (LC_1 & LC_2) at specific distances L_1 and L_2. By carefully choosing the lengths, an MMI waveguide of width W and refractive index n_c can be designed to generate patterns with specific number of spots on the two LC channels for different excitation wavelengths. Equation 5.1 gives a rough analytical expression for the MMI waveguide design,

$$N_j L_j = \frac{n_c w_{eff}^2}{\lambda_j} \qquad 5.1$$

For the current application, the MMI waveguide of width 75 µm (W_{eff} = 75.2 µm) and refractive index 1.46 is used. The MMI waveguide is designed to intersect the first LC channel at length L_1 = 1676 µm to generate a pattern with eleven spots when excited at around 556 nm wavelength and intersect the second LC channel at L_2 = 2243 µm to produce a pattern with seven spots at 633 nm wavelength. The MMI waveguide lengths were designed using PhotonD simulations to account for the effective width W_{eff}. Fig 5.2a shows the optical image of the chip and the excitation patterns (Fig 5.2b).

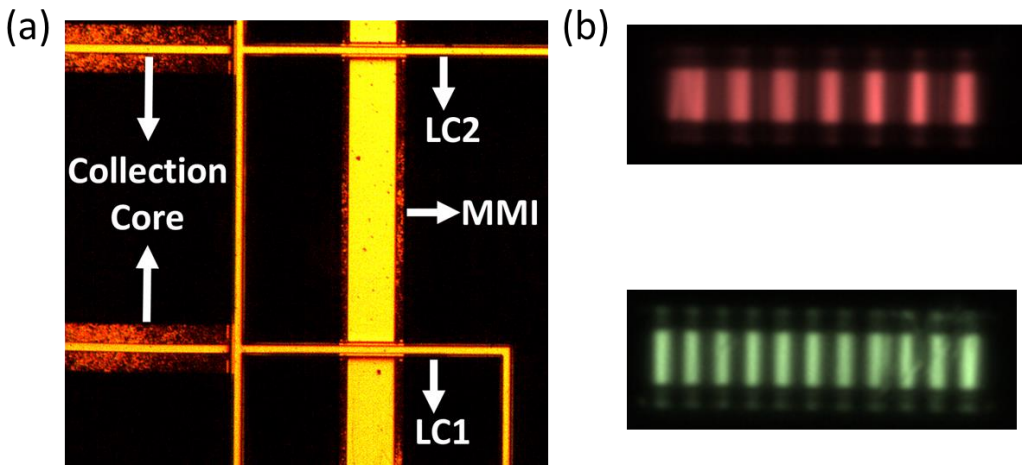


Fig 5.2 a) Top down optical image of the ARROW biosensor b) Fluorescence image of the excitation pattern generated in LC_1 (bottom) and LC_2 (top) when excited by 556 nm and 633 nm respectively

Green fluorescent tagged targets are introduced in LC_1 and red tagged targets in LC_2. The MMI waveguide is butt coupled to both He-Ne laser (633 nm) and a solid-state laser (556 nm). Targets get excited by the MMI waveguide and generate fluorescence signals which have the spectral and spatial information encoded based on the channel in which the target flows. The fluorescence signals from the LC channels are collected by two separate “collection” SC waveguides which taper into a single output. The signals from the output is detected with an

APD as time tagged photon counts. The signals with eleven photon spikes are those from LC_1 excited by 633 nm wavelength and those with seven spikes are from LC_2.

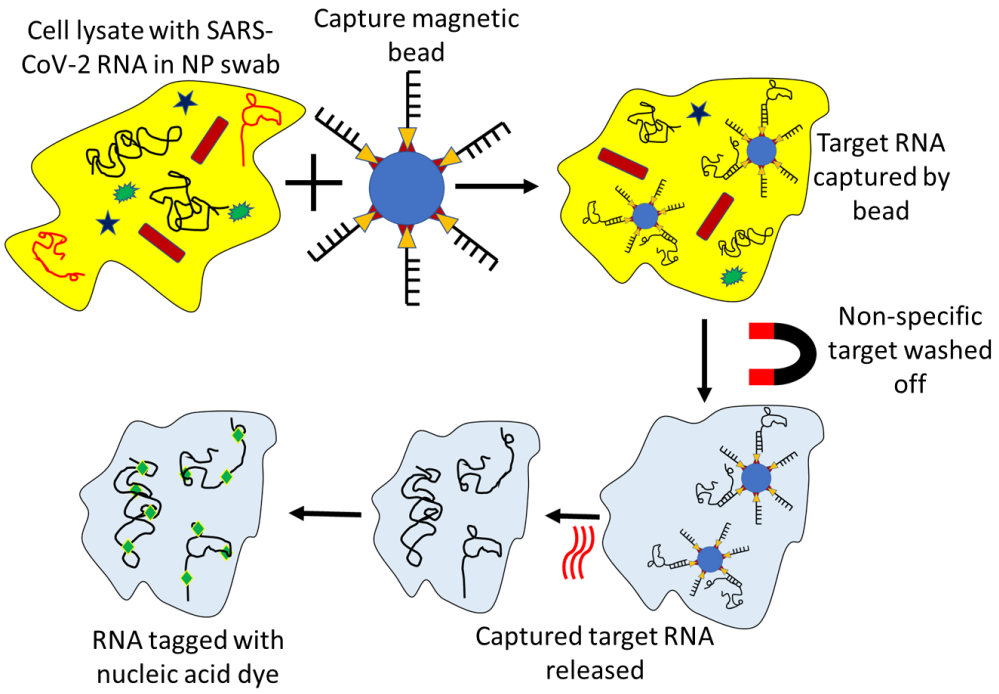


Fig 5.3 Target specific capture and fluorescent labeling of SARS-CoV-2 RNA

5.2 RNA and protein targets with bright fluorescence

Nucleic acid targets: Heat inoculated cell lysate of Vero E6 cells infected with SARS-CoV-2 (BEI resource: NR-52286) is mixed with RNA shield (Zymo research) in one to one volume ratio. This cell lysate is spiked in negative NP swab (also mixed with RNA shield) to give a final stock RNA concentration of $3x10^8$ genomic copies/mL. SARS-CoV-2 RNA is target specifically captured from this using streptavidin coated magnetic beads. The magnetic beads are functionalized with biotinylated capture oligonucleotides specific to SARS-CoV-2 RNA region encoding the nucleocapsid (N) protein (MT246667.1, nt 28286 - 28340). 30 µL of the above-mentioned cell lysate in NP swab is heated to 80^0C for 5 mins to uncoil the RNA. 2 µL of functionalized magnetic beads ($4x10^9$ beads/mL) is mixed to this and incubated for more than

an hour. The beads with the RNA are pulled down with a magnet and all the unbound targets, cell lysate and NP swab are washed of by multiple buffer exchanges. The beads are resuspended in 10 µL of nuclease free and RNase free buffer and heated to 80^0C to release the captured RNA. Using a magnet, the released target RNA is eluted and tagged with 1 µM of POPO-3 nucleic acid staining dye. The dye upon binding to nucleic acids becomes fluorescent and bright enough for on-chip detection [24]. Fig 5.3 describes RNA sample preparation.

Protein targets (Courtesy of A.M. Stambaugh): Assay preparation for SARS-CoV-2 N antigen, capture mechanism is similar to that for target specific elution of nucleic acids (Fig 5.3). Magnetic beads functionalized with SARS-CoV-2 N protein specific antibodies are used to target specifically captures the target antigen. To functionalize the beads, 5 µL of magnetic beads ($9x10^9$ beads/mL) is incubated with 5 µg (≈5x molar excess) of biotinylated capture anti-SARS-CoV-2 N Protein antibody (HM1054, East Coast Bio). After washing off unbound antibodies, the magnetic beads with the capture antibody is subtended in 5 µL 1xPBS buffer. 2 µg (≈5x molar excess) DCBO-labeled anti-SARS-CoV-2 N protein antibodies (HM1055, East Coast Bio.) and 1 µg of target (SARS-CoV-2 N protein model, East Coast Bio.) antigens spiked in 50 µL of NP swab are added to the bead-pulldown complex and incubated at 37 ^{0}C for two hours. The DCBO-labelled antibody tags the target antigen and the complex gets captured by the functionalized bead.

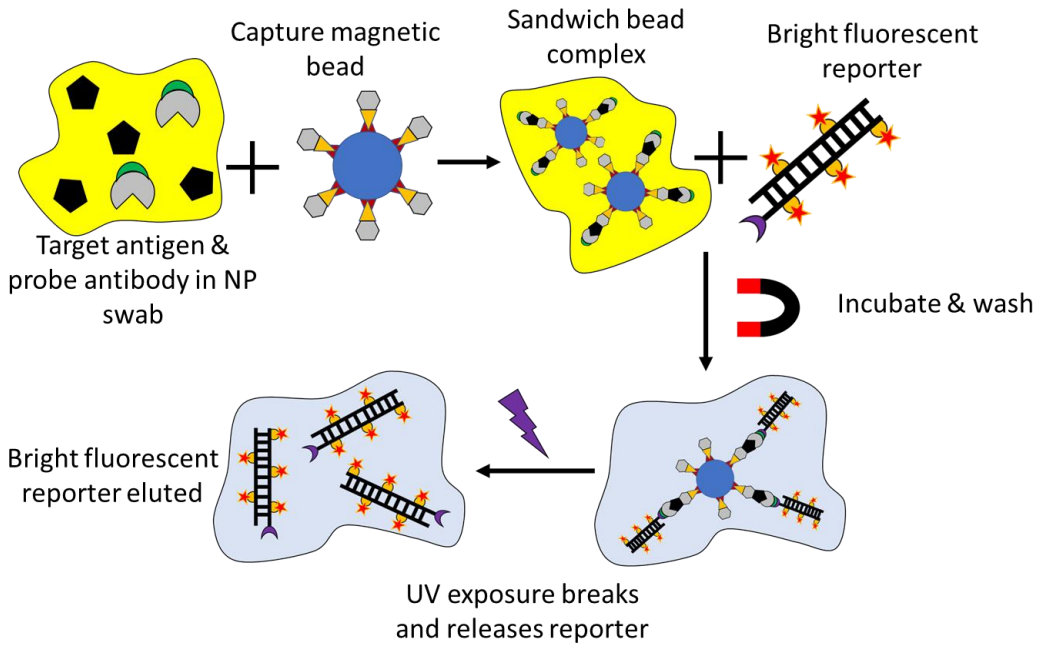


Fig 5.4 Target specific capture of SARS-CoV-2 N protein and fluorescent tagging with bright reporter

To enable detection of the antigens with single molecule sensitivity, a template DNA tagged with multiple fluorophores is used as the bright fluorescence reporter. 1kbp of pUC-19 PCR product is made with photocleavable azide forward primer (IDT) and 50% biotinylated-dUTP. To act as a probe, the DNA is then functionalized with Cy-5 (excitation: 633 nm) labelled monovalent streptavidin (mSA, Howarth Lab, Oxford University) so that there are ~250mSA/1kbp and up to 750 dye per probe. About 100 nM of this reporter probe is added to the above assay and incubated. The photocleavable azide of the reporter probe reacts and hybridizes with the DCBO-labeled antibody-antigen complex on the magnetic bead thus effectively tagging each of the captured antigen. This capture assay is washed to remove the NP swab and any unbound reporter probes and resuspended in 50 µL of 1xPBS. An aliquot of this (5 µL) is subjected to UV-B (311 nm) light for 45 seconds to cleave the reporter probes from the beads complex at the photocleavable azide junction. The beads are pulled down with a magnet and the cleaved reporter probes are eluted and diluted (1:10). Assuming 100% capture and labeling efficiency by the beads, this would correspond to a nominal concentration

of 6.4ng/mL of target antigen. Detection of the eluted bright fluorescent reports effectively corresponds to sensing the individual target antigens.

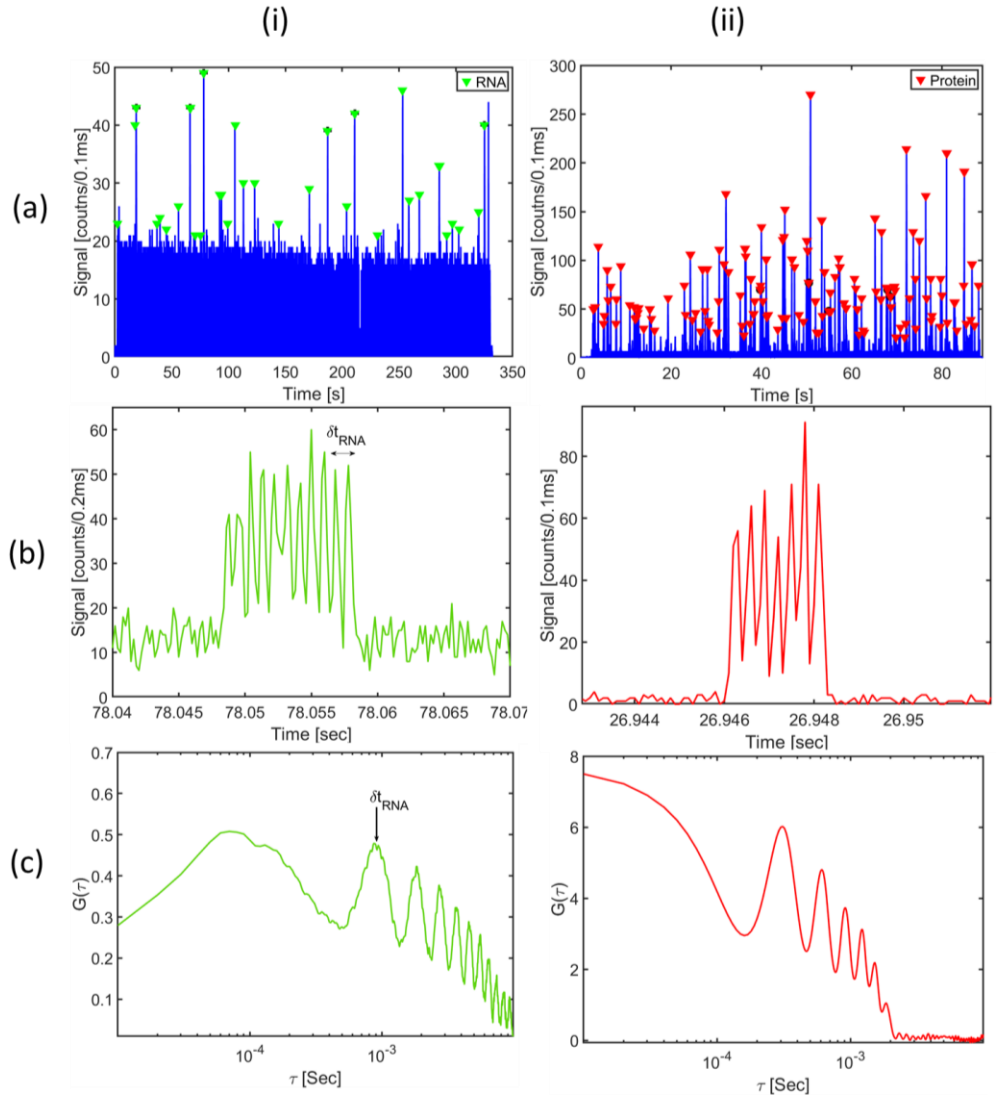


Fig 5.5 (ia) Fluorescence signal from RNA molecules tagged with nucleic acid staining dye. (ib) Zooming into an event shows a signal with eleven peaks. (ic) Autocorrelation of the signal has ten peaks which give the temporal information. (ii) Same examples from testing antigen reporters.

5.3 Single molecule sensitive target detection and identification

Fluorescently labeled SARS-CoV-2 RNA molecules and the bright reporters which represent the antigen SARS-CoV-2 N protein are detected using the ARROW biosensor with the two LC

channels. Experiments to test the accuracy and sensitivity of the device are done first. Accordingly, green fluorescently tagged RNA molecules are flown through LC_1 and buffer through LC_2. The MMI waveguide is coupled with the green laser to excite the molecules. Fig 5.5ia shows the florescence signals from individual RNA molecules detected by the APD as they flow through the MMI waveguide excitation region. A burst of photon counts above the background corresponds to a signal from an RNA. Zooming into one of the events shows a signal with eleven peaks (Fig 5.5ib) corresponding to the excitation pattern generated by the MMI waveguide in LC_1, which could be identified with a simple peak counting algorithm. An autocorrelation of the individual signal gives a clean function with corresponding ten peaks which gives the characteristic time Δt the molecules takes to flow past adjacent excitation spots (Fig 5.5ic). This could be used to obtain the flow velocity of the targets. The molecules flowing past the excitation region has a broad distribution in their velocity and the cross-sectional position with respect to the MMI waveguide. This results in fluctuations in the signal intensity and the temporal width (Δt) of the fluorescence signals. Due to this some of the signals could be very close to the noise background. Noise background from the chip which varies for different excitation wavelengths, is due to the photoluminescence of the waveguide (which is higher for blue spectrum of light) and the intrinsic fluorescence of the unbound nucleic acid staining dye molecules. For efficient signal detection and identification, the fluorescence trace is processed using the standard continuous wavelet transform-CWT method (Eq 5.2).

$$C(u,s) = \left\langle f, \psi_{u,s} \right\rangle = \int_{-\infty}^{+\infty} f(t) \frac{1}{\sqrt{s}} \psi^* \left(\frac{t-u}{s} \right) dt \qquad 5.2$$

$$\int_{-\infty}^{+\infty} \psi(u)\, du = 0 \qquad 5.3$$

Here f(t) is the time domain fluorescence signal trace and ψ(u,s) is the mother wavelet function dependent on time variable ‘u’ and scaling factor ‘s’ such that ψ(u,s) follows eq 5.3. The

fluorescence signal is correlated with the mother wavelet which is dilated (scaling factor - s) and translated (in time - u) to give the CWT coefficient C(u,s), visualized as a 2D map. The scaling factor stretches or compress the mother wavelet in time domain to give highest correlation with the multi spot temporal fluorescence signal and so can be replaced by Δt in the current application. Here, for accurate correlation with the eleven peak fluorescence signals from the RNA molecules, a matched mother wavelet function comprising of summation of elven gaussians scaled and separated by Δt (acts as the scaling factor - s) and margined by negatively skewed peaks (to satisfy eq 5.3) is used. Fig 5.7ia shows the mother wavelet function used for analyzing the eleven peak fluorescence signals from RNA and Fig 5.7ib shows an example 2D map of the CWT coefficient C(u, Δt) when correlated with a signal. The maxima in the 2D map indicates the presence of the correct signal. Similar to the experiment with RNA molecules, the bright fluorescence reporters corresponding to the antigen is flown through LC_2 and buffer in LC_1 with the MMI waveguide excited with 633 nm laser. Fig 5.5iia shows the fluorescence trace from the APD. Zooming into one of the events (Fig 5.5iib) show a signal from the reporters with seven peaks and an autocorrelation generates six peaks (Fig 5.5iic). Signals from the antigen reporters have lower background due to lower photoluminescence form the waveguides at red wavelength and because unbound fluorescence probes are removed from the elute during sample preparation wash steps. For analyzing the signals from the antigen reporters using CWT, a matched mother wavelet function with seven peaks is used (Fig 5.7iia). Fig 5.7iib shows the example of the 2D map of the CWT coefficient when applied to a signal from the antigen reporter.

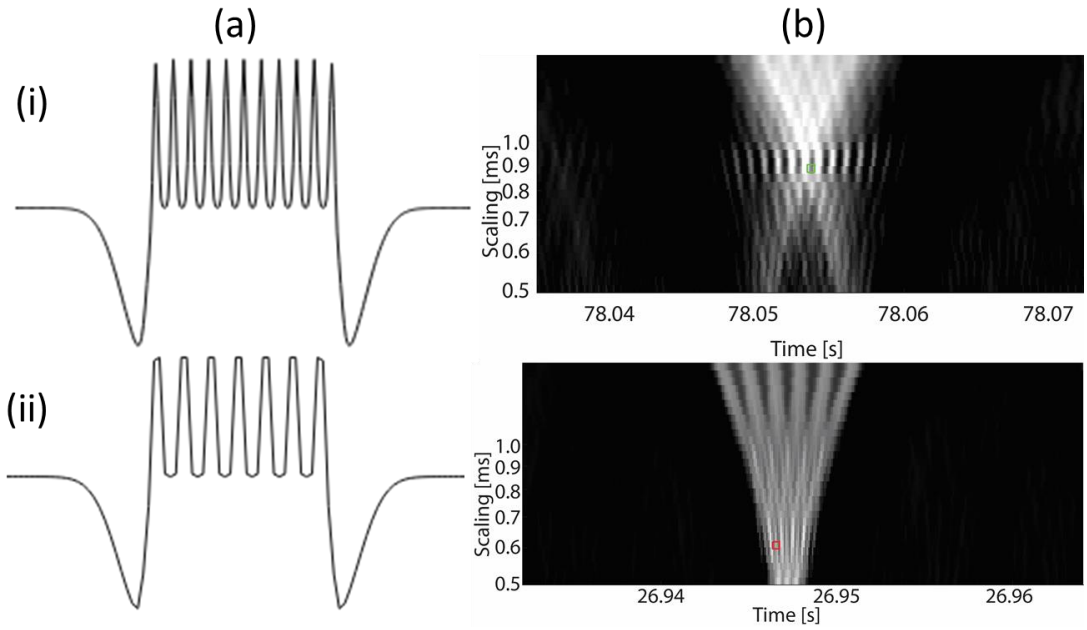


Fig 5.6 ia) Eleven peak mother wavelet function for identifying RNA signals. ib) Example of the CWT coefficients, C(u,s) from analyzing the RNA signal in Fig 5.5ib. Green dot represents the maximum value of the coefficient. ii) Same examples for analyzing antigen reporters

The fluorescence trace of each target set is processed with both wavelets. Analyzing the fluorescence trace from the experiment with RNA, showed events detected at a rate of ≈ 0.1events/sec with more than 84% correctly identified as signals with eleven peaks from RNA molecules. Signals from the experiments with antigen reporters were detected with a higher rate of ≈ 3events/sec with 98% correctly identified. Thus, enabling rapid detection and identification of targets with single molecule sensitivity and good accuracy.

5.4 Multiplexed amplification free detection of SARS-CoV-2 antigens and RNA

For multiplexed detection of nucleic acid and protein targets, fluorescently tagged RNA molecules and the antigen reporters are flown simultaneously in LC_1 and LC_2 respectively. The MMI waveguide is excited with both the green and red laser simultaneously. Similar to the experiments in chapter 4, the signals from the two channels are collected through the collection core waveguides and coupled to the APD. Signals corresponding to individual RNA and protein molecules with eleven and seven peaks respectively are detected. Signals were detected and

identified by processing the fluorescence trace using CWT with both wavelet functions. Using the dimensions of the excitation volume (height x width: 2.45 µm x 12 µm) and the average speed of the particles obtained from the autocorrelation of the signals, an estimate of $3x10^5$ copies/mL of SARS-CoV-2 RNA and $2.64x10^6$ particles/mL (0.2pg/mL) of SARS-CoV-2 N antigens are detected. This demonstrates, for the first time, multiplexed detection of SARS-CoV-2 nucleic acids and proteins spiked in NP swabs, circumventing the need for amplification steps such as PCR and represents a significant contribution towards exploring new techniques for quick and accurate detection of COVID-19. This is enabled by detecting events with single molecule sensitivity at rapid rates of over an event per second. RNA molecules are more fragile and susceptible to degradation as compared to the fluorescently tagged template pUC19 DNA (which acts as the reporter for proteins). This along with the variability in the binding of the nucleic acid staining dye could account for lower event counts from the nucleic acid sample compared to the antigen reporter. These differences can be mitigated in the future by using more stable reporters such as surface functionalized quantum dots or nanobeads for both the targets.

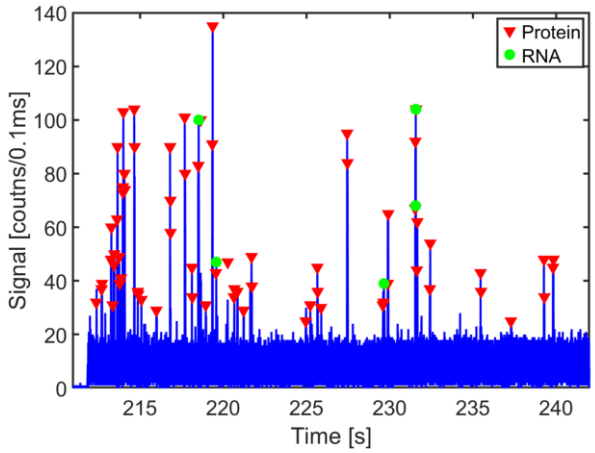


Fig 5.7 Fluorescence signals when both antigen reporter and RNA molecules are flown through the chip with the MMI waveguide excited by both the lasers.

From analyzing the signals above a set background threshold (27 counts/0.1ms - highest photon count from testing blank samples) the average signal strength was 51 counts/0.1ms

and had an average SNR of 5.7 (defined as average signal strength: average background noise). Though most of the detected signals had a good SNR and the events irrespective of signal strength were detected using CWT, the estimated concentrations of the analytes are several orders lower than the starting concentration. This is mostly due to the magnetic bead based capture assay. Since large size molecules are being captured on the bead, only a fraction of the analytes can be target specifically extracted from the NP swab samples due to steric hindrances. Extracted samples on the beads could also be partially lost during the successive wash and release cycles the assay under goes. This can be overcome by using sample preconcentration methods such as PDMS based sample enrichment units or more sensitive detection methods like nanopores and optical trap assisted detection rate enhancements [93].

6 Index guided liquid core waveguides for enhanced fluorescence detection

One of the major goals of a biosensor which is developed for diagnostic applications, is to be able to detect pathogens at clinical concentrations. The concentration of nucleic acids in a patient's body, especially during early stage of development of the disease is in the range of 10^{-15} – 10^{-18} M (10^{5} – 10^{2} copies/mL) [94, 95]. The ability of a device to measure such low concentrations depends on the sensitivity of the sensor. This chapter discuses an approach to enhance the detection capability of the biosensor by tuning the optical performance of the LC waveguide, using high refractive index liquids.

The main principle behind the function of the ARROW platform as a biosensor is its ability to guide light both in low index SC waveguide (SiO_2 as core) and a low index LC waveguide (water as core) on a high index Si substrate. This enables the sensor to excite using the SC waveguide, fluorescently tagged particles flowing through the orthogonally intersecting LC waveguide, and also collect the signals using the LC waveguide. Chapter 3 and 4 discussed the ability of the device to detect pathogens with single molecule sensitivity and do up to 7x multiplexed target sensing using MMI waveguides. Previous works mentioned in the introductory chapter have demonstrated the ability of the device to sense low target concentration via integration with PDMS based sample enrichment systems. Despite the excellent performance, these sensors still have the challenge to detect low intensity signals due to the inherent properties of the ARROW design [96]. The anti-resonant boundary condition of the waveguides makes the field intensity of the optical mode zero at the walls of the LC waveguide which have the anti-resonant-reflective layer (Fig 6.1).

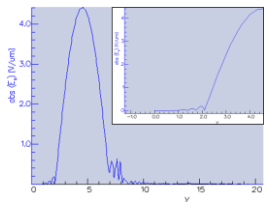


Fig 6.1 Fundamental mode electric field profile of a LC ARROW waveguide (Inset: ARROW boundary).

This lowers the efficiency of the coupling of fluorescence signals from particles broadly distributed near the walls of the LC waveguide with the tightly confined optical mode. This along with the finite propagation loss of the LC waveguide limits the performance of the ARROW based biosensors in terms of SNR and the number of particles detected. One way to address this challenge is to implement hydrodynamic flow focusing designs using surface micromachining techniques to keep particles to the center of the LC waveguide and better overlap them with the optical mode [97, 98]. However, while this approach improves performance, it dramatically increases the fluidic complexity of the device and is not practical for a point-of-care applications.

Apart from using anti-resonant-reflecting layers, guiding of light in the LC channel can also be achieved by using solutions with high refractive index as the core instead of water. Ionic liquids [99] and choline [100] derived ionic liquids are organic solutions with refractive index higher than SiO_2 and in which nucleic acids are stable [101]. However, these solutions have very high viscosity, one or two orders of magnitude more than water and so cannot be used for the current application [102, 103]. High refractive index salt solutions such as sodium or zinc iodides have been used in many applications such as in laser cavities, immersion lithography, ink jet printing and particle image velocimetry [104, 105]. These solutions are transparent and their viscosity is very close to water. Although they are not compatible with nucleic acids, solid state fluorescent probes such as polystyrene nanobeads or quantum dots are stable in these solutions [106]. With high refractive index liquid as the core, the LC channels can support index guided optical modes. To demonstrate this, a SiO_2 based optofluidic biosensor having a similar geometry as the ARROW biosensor is used. The sensor has an index guided SC waveguide that excites fluorescent particles flowing in a LC channel having high refractive index ZnI_2 salt solution. The core refractive index of the LC waveguide is easily tuned by changing the salt concentration [107, 108] to optimize the optical mode for enhanced collection of signals from the fluorescent particles broadly distributed in the LC channel while still maintaining a good

confinement factor. The chapter demonstrates that tuning the optical property rather than optimizing the fluidic properties of the chip enables to effortlessly push the LOD of the device.

6.1 Device design

The sensor has an overall layout similar to the previously described ARROW biosensor. A SC waveguide excites fluorescently tagged particles flowing in an orthogonally intersecting LC waveguide. The signals are collected by the LC waveguide and sent to an APD using the "collection" SC waveguide.

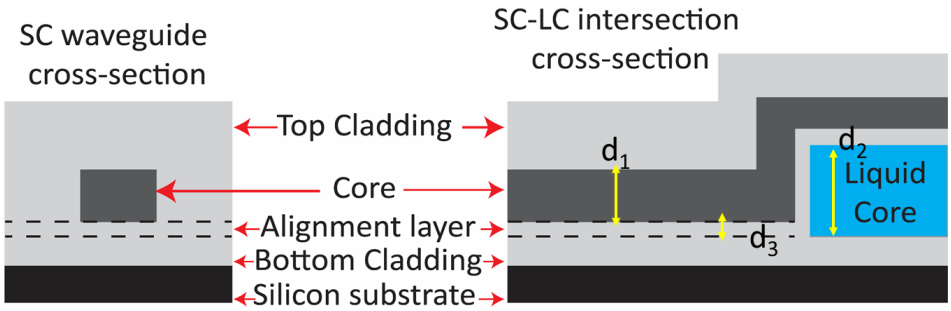


Fig 6.2 Schematic of the cross section of the SC and SC-LC intersections

Fig 6.2 shows the cross section of the SC waveguide and the SC-LC intersection. The SC waveguide has a high refractive index SiO_2 core (1.508) surrounded by a cladding SiO_2 of lower refractive index (1.451). The thickness of the core (d_1) is designed to have 70% or more coupling efficiency with the single mode F-SV fiber used to excite the waveguide. Fig 6.3a shows the simulated coupling efficiency for a range of thickness. Fig 6.3b is the SEM cross sectional image of the SC waveguide with thickness 2.4 µm. The bottom of the SC waveguide has two layers of cladding material (Fig 6.2). The first "bottom cladding" layer is common for both SC and LC waveguides and prevents leakage of light into the Si substrate. The second layer (marked as the dashed line) allows to align the SC waveguide in position with the LC waveguide and also acts as the cladding material for the other three sides of the LC waveguide. The thickness of the LC waveguide and the "alignment layer" are also designed to have at least 70% or more coupling efficiency with the fundamental mode of the SC waveguide (Fig 6.3c).

This ensures that the fluorescent particles flowing in the LC waveguide are efficiently excited by the SC waveguide. Fig 6.3d shows the SEM image of the SC-LC intersection cross section.

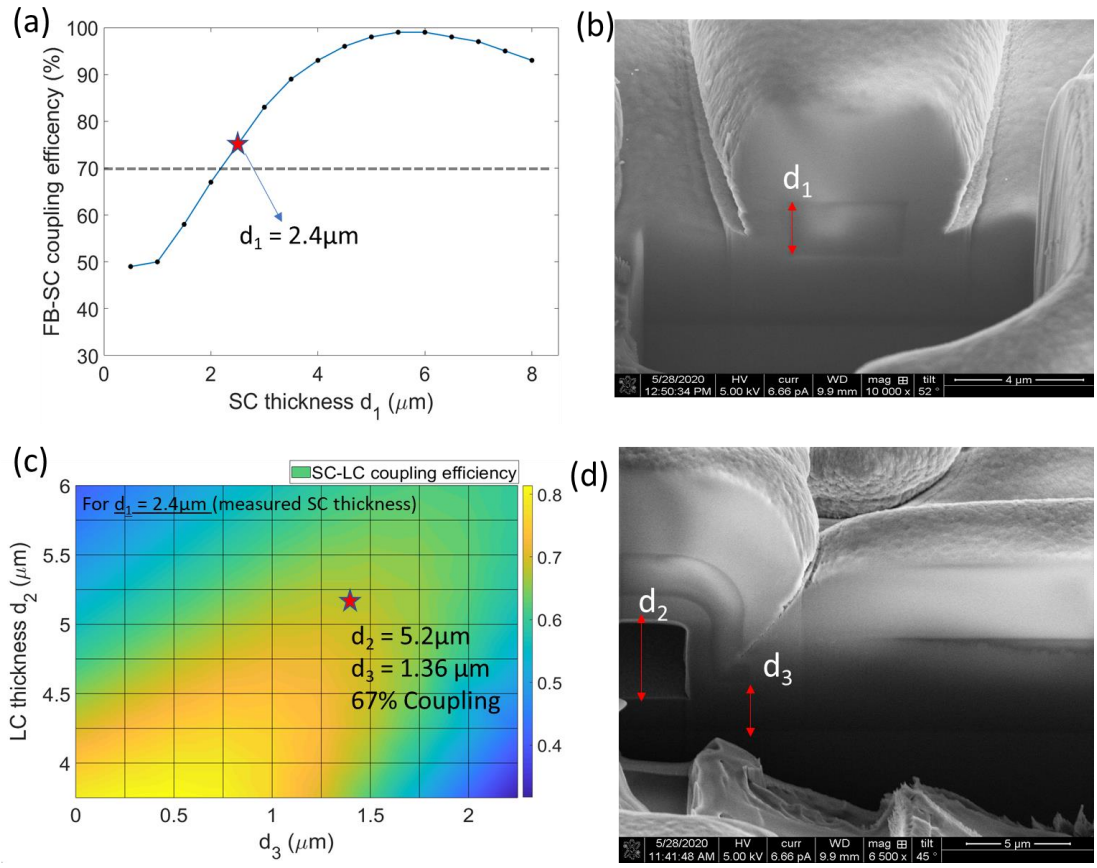


Fig 6.3 a) Simulation of fiber to SC waveguide coupling efficiency (Device geometry after fabrication is marked in red star). b) SEM image of SC waveguide cross section. c) Simulation of SC to LC waveguide coupling efficiency. d) SEM image of SC-LC intersection.

To have high detection sensitivity it is important to send the fluorescence signals from the particles to the APD efficiently by coupling into a waveguide mode and guide it off the chip with minimal loss. The index of ZnI_2 solution ranges from 1.4 to 1.6 by varying the salt concentration in water (Fig 6.4). By filing the LC channel with refractive index higher than the cladding (1.451), an index guided optical mode via total internal reflection can be supported. Fig 6.5a shows the simulated fundamental mode of the LC waveguide when filled with H_2O and ZnI_2. The waveguide supports a leaky mode with field radiating out of the core when filled with water. But

generates a well confined index guided mode when having high refractive index ZnI_2.This is confirmed by taking mode images of the LC waveguide excited at 633 nm wavelength when filled with H_2O and ZnI_2 (Fig 6.5b). The LC waveguide was fabricated to be 12 µm wide and so supports multiple modes rather than only a fundamental mode. When filled with water, the leakage of light into the cladding layer is evident. The index guided mode when filled with ZnI_2 has 28% more confinement factor (Percentage of energy density of the mode confined inside the core of the waveguide, measured from mode image in terms of pixel intensity).

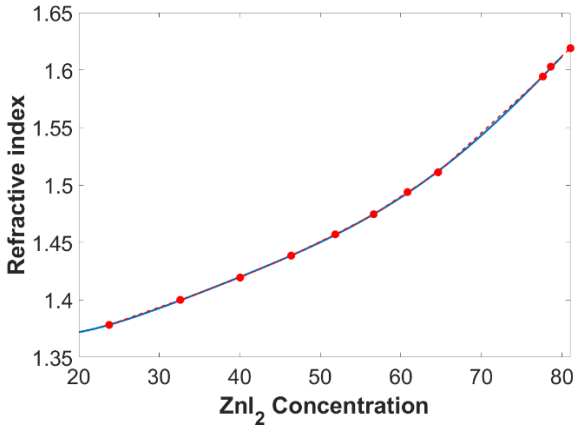


Fig 6.4 Refractive index of ZnI_2 varying with concentration (data used from [107])

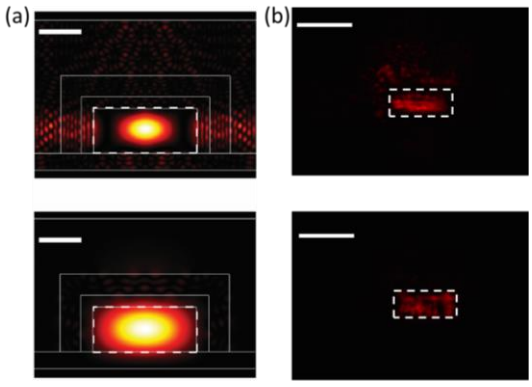


Fig 6.5 a) Simulated mode images of LC waveguide with H_2O and ZnI_2 (Scale: 5 µm). b) Mode images of the same (Scale: 10 µm)

Transmission measurements along the liquid channel show a 9.4x increase at 633 nm when filled with ZnI_2 solution compared to water (Fig 6.6). This demonstrates improved light guiding which permits the LC waveguide to guide the fluorescence signals from the particles to the APD with minimal loss thus improving the signal-to-noise-ratio (SNR) of the signals.

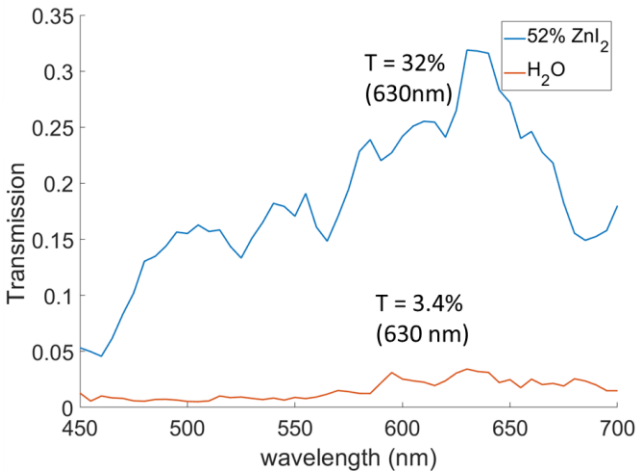


Fig 6.6 Transmission measurement along the LC waveguide

The LC waveguide core index needs to be optimized to efficiently collect the fluorescent signals from all the excited particles to the optical mode. Since particles are broadly distributed all over the LC cross section, the optical mode has to cover the whole of the LC cross section to couple in the signals. When filled with water, the mode overlaps only with the particles near the middle of the channel and the ones located at the corners are excluded. When the core refractive index is nearly matched with the cladding index, the electric field is more uniformly distributed all the way up to the channel walls (Fig 6.5a). This maximizes the LC cross section area the mode field covers and overlaps the mode with particles even at the edges of the LC. To quantify how well the mode field covers the LC cross section, a “Spread Factor” is defined as the ratio between the mode field intensity at the boundary of the LC and the highest mode intensity value (Fig 6.7). As the refractive index of the core approaches that of the cladding, the spread factor increases but the mode becomes less confined. Both parameters are important and need to be maximized for good coupling and collection of the fluorescence signals.

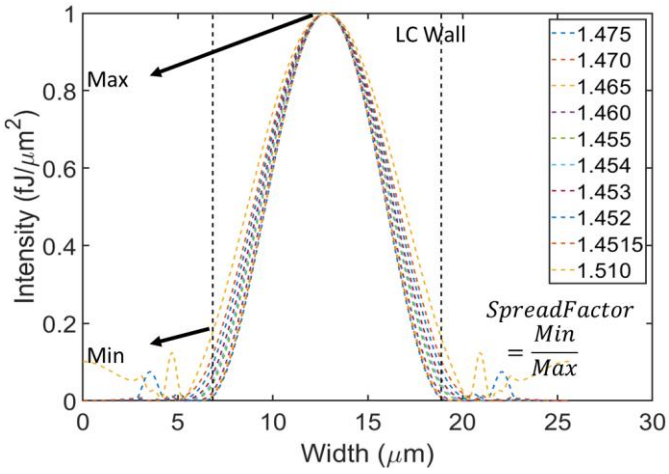


Fig 6.7 Horizontal mode profile of the LC fundamental mode for varying core refractive index.

Fig 6.8 shows the variation of both spread factor and the confinement fact with change in ZnI_2 salt concentration. ZnI_2 solution of optimum refractive index range of 1.454 - 1.455 is chosen (51% - 52% of salt concentration, marked in arrows in Fig 6.8). This increases the spread factor by 33x as compared to the leaky mode with water. Assuming the particles are evenly spread across the LC cross section, the broad LC optical mode with large spread factor when filled with ZnI_2 brings 47% more particles within the mode field diameter ($1/e^2$ value). Similarly, a 38% increase in confinement factor is also observed from the simulations, close to the experimental results obtained from mode image measurements.

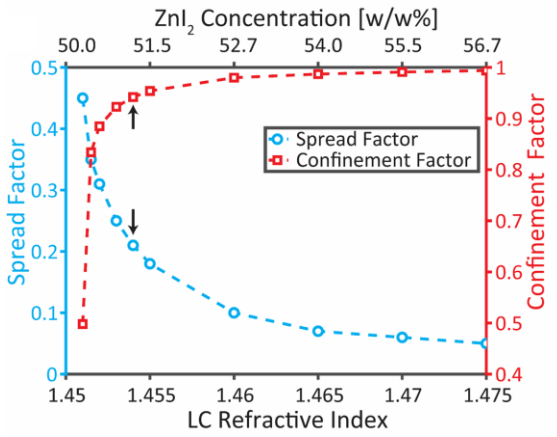


Fig 6.8 LC fundamental mode spread factor and confinement factor

6.2 Enhanced detection of fluorescent nanobeads

For fluorescence detection, 800fM of fluorescent nanobeads in ZnI_2 salt solution is flowed through the LC waveguide. The beads coated with streptavidin are ≈ 20 nm in diameter and fluoresce at 633 nm. The SC waveguide is excited with a He-Ne laser. The signals generated by the nanobeads collected using the APD are shown in Fig 6.9a. The black dotted line at 5 counts/100 µs is the background threshold. Events detected when the waveguide is filled with ZnI_2 solution clearly shows much better collection of signals, both with respect to the signal intensity and number of events compared to the same experiment done with water. An 8x increase in SNR is observed which is in good agreement with the improvement seen in the LC waveguide transmission measurements.

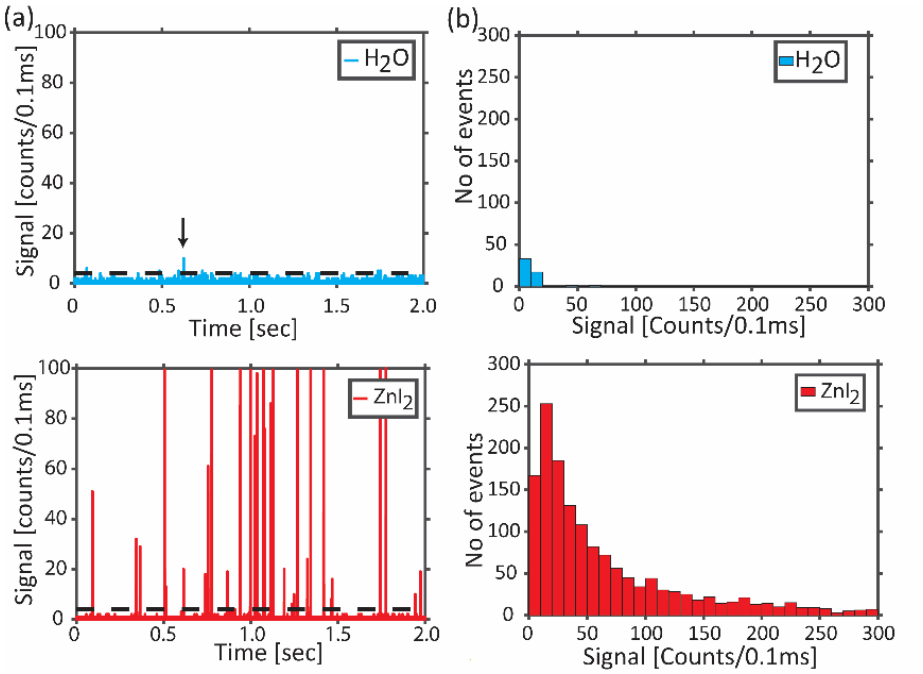


Fig 6.9 a) Fluorescence signal from individual nanobeads. b) Distribution of the bead signals from a 100 sec long fluorescence trace

Fig 6.9b shows the histogram distribution of the signals detected in both the experiments. The variations in the signal strength are due to the broad distribution of the position of the nanobeads in the LC cross section. In the case of ZnI_2, the optical mode fills the channel cross

section very well and so the signals from the beads that are located even near the wall gets coupled into the mode. On the other hand, when the LC is filled with water, the mode has a field with much lower spread factor and couples in only the signals of the beads from the center. During a 100 sec long experiment, 95 and 1,535 nanobeads are detected when using water and ZnI_2 in the LC channel, respectively. Since ZnI_2 has about two times higher viscosity than water, the beads flow with lower velocity. To make an unbiased comparison, the improvement of the signal capture rate needs to be compared based on the total sample volume tested. Using the dimensions of the excitation volume (Width = 12 µm, height = 2.2 µm, length = 2.7 µm) and the average time duration of the signals, a concentration of 7.5×10^6 particles/mL is estimated to be detected from the signals with water and 1.1×10^8 particles/mL is detected with ZnI_2. Thus, over an order of magnitude in improvement is seen which would enable detection of concentration of particles at sub-femtomolar scale.

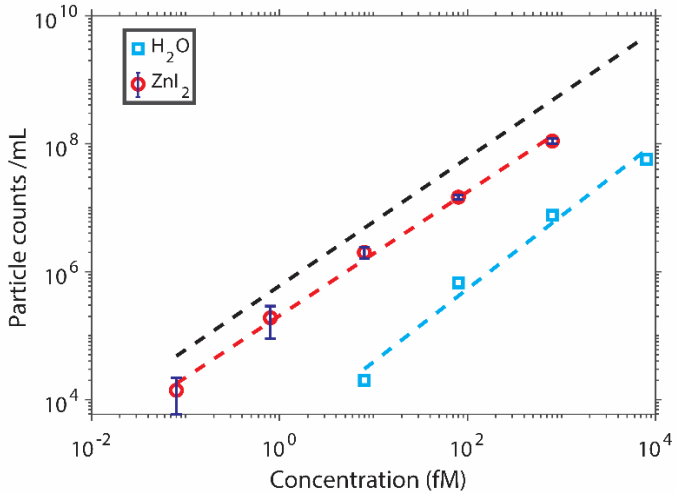


Fig 6.10 Serial dilution of the nanobeads and measured particle counts per unit volume. The black dashed line shows the expected particle counts per unit volume.

Fig 6.10 shows the number of particles detected per unit volume by the chip from six orders of dilutions of the nanobeads. The black dashed line shows the expected particle count rates at each concentration. When the LC is filled with water, very few beads, two orders of magnitude lower than expected counts are detected. This results in a LoD of around 8fM. By enhancing

the sensitivity of the device using ZnI_2 solution, an average of 45x increase in the particle counts per unit volume is seen. The measured count rates are closer to the expected values. This enables to bring the LoD of the device lower by two orders of magnitude reaching 80 aM. At such ultra-low concentrations, the sensitivity of the device is limited by the amount of sample volume flowed through the chip [109].

6.3 Enhanced performance with buried ARROW chips

Fluorescence signal enhancement using ZnI_2 salt solution can be achieved with buried ARROW sensors too. Fig 6.11a shows the cartoon of the SC-LC cross section of the buried ARROW device. Since the LC channel is surrounded by SiO_2 of high refractive index (1.51), a higher concentration of 65% ZnI_2 solution is used to achieve guiding of light via total internal reflection. Fig 6.11b shows the simulated fundamental mode in the LC waveguide with water and ZnI_2. The reflecting layers at the bottom of the LC channel follow the anti-resonant condition and so pushes the mode slightly higher. When the LC is filled with ZnI_2 solution to partially match core refractive index with the surrounding cladding, a guided mode extending to the top, left and right boundaries is supported. However, due to the ARROW layers the mode fails to fully cover the bottom section.

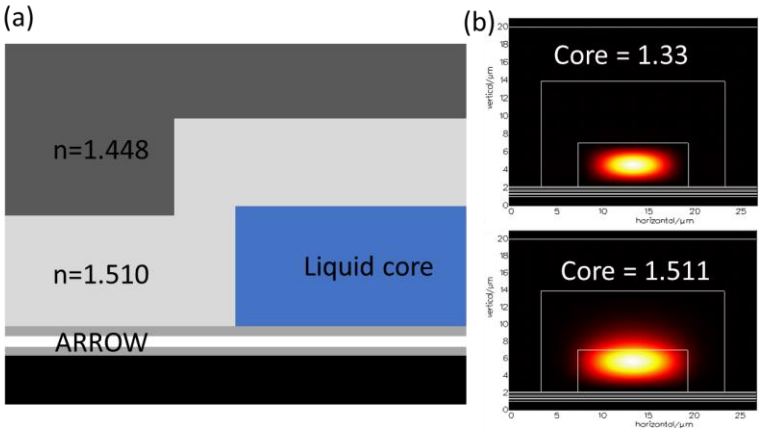


Fig 6.11 a) Cartoon of buried ARROW SC-LC cross section. b) Simulated mode image of the fundamental mode of buried ARROW LC channel

Due to the reflecting layers in the buried ARROW chip, satisfactory guiding of light is already achieved just with water as the core. On the other hand, the sensor without the ARROW layers described in section 5.2 has poor guiding of light when the LC is filled with water because the mode is leaky. This is evident in the LC transmission measurements. Since to begin with, the LC waveguide in the ARROW sensor guides light reasonably when filled with water, only a 3x improvement is seen when water is substituted with ZnI_2 (Fig 6.12). Compared to this, a much higher improvement, a factor of ≈10x is seen with the sensor without the ARROW layers.

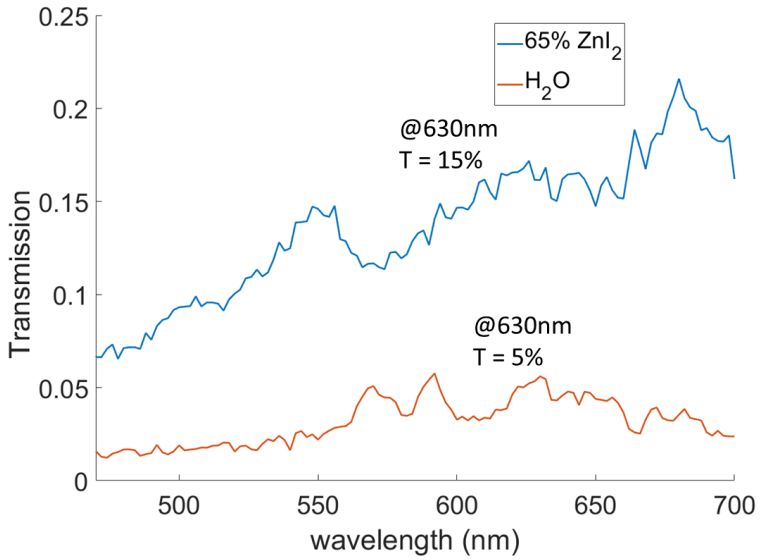


Fig 6.12 Transmission measurement along the LC waveguide for an ARROW biosensor

Experiments on detecting the nanobeads with a buried ARROW chip (similar to section 5.2) using ZnI_2 in the LC channel is shown in Fig 6.13a. A 2x increase in SNR is observed which is in correlation with the results from transmission measurements. More importantly, the number of detected events increased significantly (30x improvement) since the mode supported in the ZnI_2 solution covers the three ends of the LC waveguide and collects the signals from the broadly distributed particles.

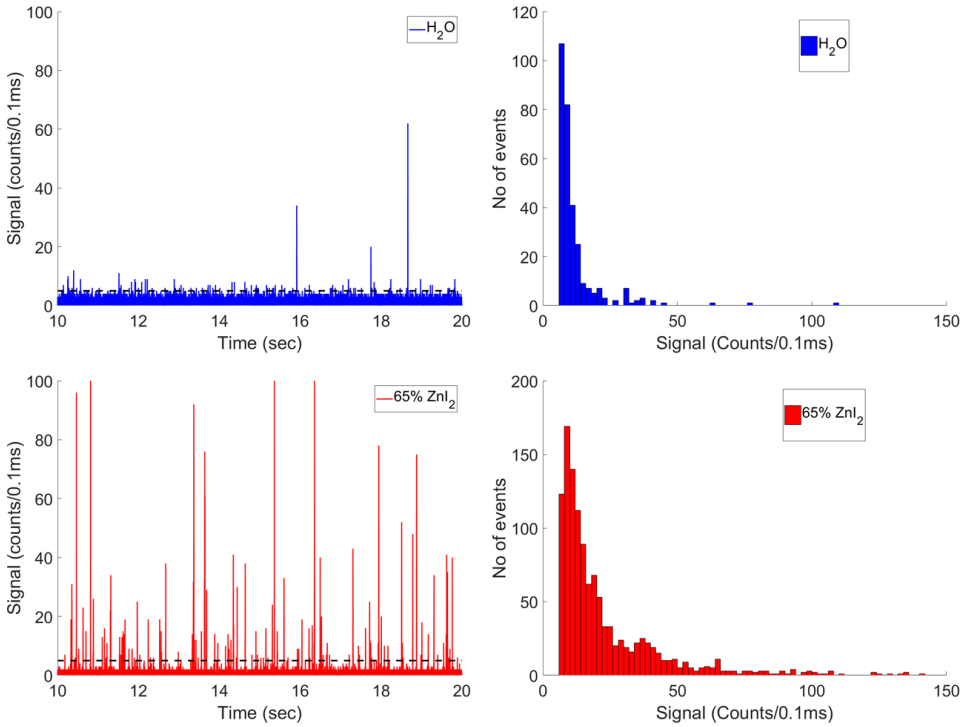


Fig 6.13 a) Fluorescence signal from individual nanobeads tested in ARROW chip. b) Distribution of the bead signals from a 100 sec long fluorescence trace

Signal enhancement using high index salt solution can also be used for improved detection using MMI waveguides. Signals from the beads excited with an MMI waveguide when collected using the ZnI_2 solution give much cleaner events, enabling off chip signal processing such as autocorrelation (Fig 6.14a). For example, clear 7 peak signals from the nanobeads are detected when excited by the MMI waveguide at 633 nm wavelength. An autocorrelation on the signal gives the expected 6 peaks from which the δt information can be extracted (Fig 6.14b).

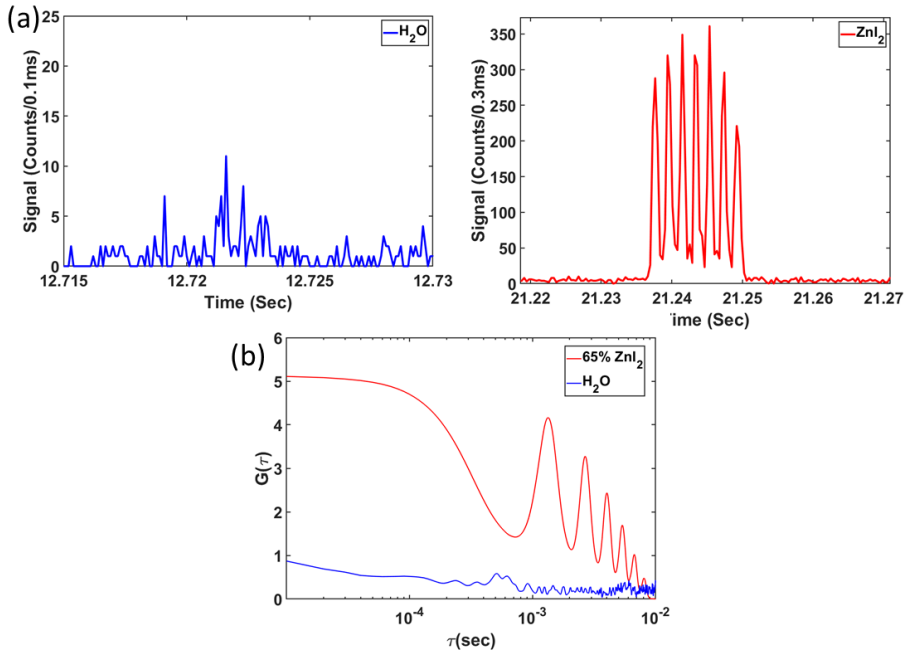


Fig 6.14 a) Signal from a nanobead when excited with an MMI waveguide when the ARROW LC waveguide is filled with water (Blue) and ZnI_2 salt (Red). b) Autocorrelation of these signals

Thus, by using high index ZnI_2 solution, both types of SiO_2 based biosensors (with ARROW and without ARROW) show enhanced fluorescence detection. This is achieved by tuning the LC refractive index to support an index guided optical mode that effectively collects signals from particles distributed across the LC cross section. Through optimizing the optical performance of the device, eight times increase in SNR and a 100x improved LOD in the attomolar range are reached. Biosensors in diagnostic applications generally use direct detection of fluorescently tagged DNA or protein molecules which are not compatible with ZnI_2 salt solutions. However, surface functionalized water-soluble solid-state probes such as quantum dots (Qdot probes, Thermofisher) [110] and nanobeads [111] can be used as the reporter instead of the biomolecule itself. Using stable buffer solutions, nucleic acid and proteins could be selectively labeled with target specifically functionalized solid-state probes such as the nanobeads and then captured on to magnetic beads (Dynabeads, Thermofisher). After elution of this final assay, buffer exchange steps by pulling down the magnetic beads can

be used to replace the solvent with the high index salt solution. The probes may get released from the magnetic bead due to the solvent change or can be thermally or optically released and detected using the biosensor. Therefore, the ability of the device demonstrated in this chapter to detect ultra-low concentrations of such fluorescent probes is directly applicable to diagnostic assays [112] and points towards development of a highly sensitive, portable and accurate diagnostic platform.

7 Optofluidic sensor with integrated sample preparation

The previous chapters of in this thesis described Si based optofluidic chips with multiplexed biosensing applications. The demand for developing such tools comes from the ever-pressing need to simultaneously analyze multiple biomarkers such as nucleic acids and proteins. This has been relevant for scenarios like cancer companion diagnostics [113] and more recently for accurate screening of COVID-19 infection [114]. Another example is infections caused by Zika virus (ZIKV) whose protein biomarkers exhibit cross reactivity with other flaviviruses like dengue [115, 116]. This makes analysing diagnostic results from the preferred tests such as enzyme linked immunosorbent assays (ELISA) difficult to interpret, since tests can yield false positives [117]. Thus, additional confirmatory tests based on nucleic acids are required. Zika RNAs have very high specificity and are detected early on (first 1-2 weeks) but require concurrent serological tests for fast diagnosis of acute infection [118]. Therefore, a multi-target analysis system is required for reliable and confident testing of such infections.

The previous chapters described various methods using optofluidic devices to do multiplexed detection of pathogens using fluorescence. But preparation of the assays and fluorescent tagging of the biomolecules where done off chip (Chapter 3) or using microfluidic systems that are not compatible with each other (Chapter 4). Sample preparation is a crucial element that needs to be miniaturized to reduce the processing time and also circumvent the need for trained technicians and special laboratory settings. In this respect, PDMS based pneumatically actuated microvalve automata have proved to be an important tool, not only because of their ease of fabrication and wide-ranging fluid handling capabilities but also because they can be programmed to enable flexible and complex operation [119, 120]. Several demonstrations have been made via hybrid integration to combine PDMS microvalve automata with SiO_2 based ARROW chips to integrate sample processing with optical detection [9, 121]. But, integration of two separate chips made from materials incompatible with each other makes device handling

cumbersome, calls for separate optimizations of device design and fabrication procedures and increases the possibility of sample contamination.

As a solution to this problem, this chapter discuss the design and implementation of an all-PDMS platform which combines, on a single chip, sample processing and in-flow optical detection of biomolecule targets. An array of programable and pneumatically controlled micro valves are used for sample preparation. By using different precursor ratios to get high and low refractive index PDMS, PDMS based optical waveguides are monolithically integrated with the automatons to enable optical detection [122]. First fluorescent labeling and detection of λ-DNA with single molecule sensitivity is demonstrated using this system. Further, the programmability and flexibility of the device to handle more complex analytes is demonstrated by simultaneous capturing, fluorescent labeling and detection of ZIKV nucleic acid and protein targets from human serum. This dual assay allows for successful differentiation of Zika targets from structurally similar flaviviruses like dengue, thus paving the way for a fully integrated chip for disease diagnostics.

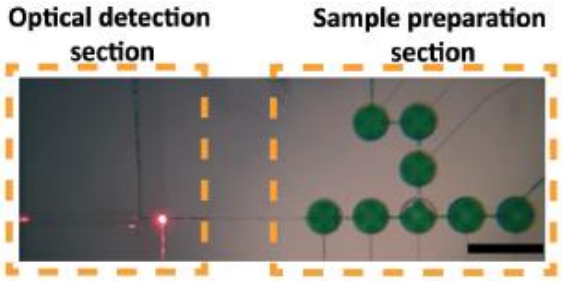


Fig 7.1 Top down microscope image of the PDMS chip, scale bar: 1 mm. The waveguide is excited with a red He-Ne laser and the pneumatic valves are filled with green food dye

7.1 Architecture of the PDMS chip and fabrication

The device consists of two primary sections, one consisting of a series of pneumatic valves for on chip sample preparation and the other consisting of an optical detection (Fig 7.1). The detection part follows a similar architecture as the ARROW biosensor chips. A combination of orthogonally intersecting SC and LC waveguides are used for excitation and collection of

fluorescently tagged biomolecules. Here the LC has a leaky optical mode and so is very lossy unlike the ARROWs [122]. This compensated for by keeping the length of the LC channel very short. The chip is fabricated through a three-layer PDMS architecture. The central layer which has a higher refractive index allows for defining SC optical waveguide. The optofluidic chip is fabricated in two parts using soft lithography. This is described in Fig 7.2. Two separate masters – one consisting of the optical waveguides and the fluidic channels (≈ 6 μm thick), and the other consisting of the pneumatic valves (≈ 18-20 μm thick) – are fabricated with standard photolithography processes using negative photoresist SU-8 2005 (Microchem) and SU-8 2025 (Microchem), respectively, and were subsequently silanized (Fig 7.3). A 1:5 (curing agent: base polymer) PDMS (Sylgard) mixture is then spun onto the first master at 5000 RPM for 25 minutes and cured at 60 °C for two hours. After the bake, a 1:10 (curing agent: base polymer) PDMS mixture is spun on top of this at 1000 RPM for five minutes and cured overnight at 60 ^{0}C. The 1:5 PDMS layer which has higher refractive index of 1.425 acts as the core and the 1:10 mixture with lower refractive index of 1.420 is the cladding. These also serve as the lifting gate membrane for the pneumatic valves that connect fluidic lines. In parallel to this process, a 1:10 PDMS mixture is also cast on the second master which will be used as the pneumatic chambers to lift and close the pneumatic membrane.

After curing at 60 ^{0}C for two hours, the PDMS layer is peeled off from the second master and ports are punched for the pneumatic line connections. The two PDMS layers are then treated in oxygen plasma to activate the necessary surfaces and are quickly bonded together after carefully aligning the pneumatic chambers on top of the lifting valve membranes on the first master. The PDMS is again baked in 60 ^{0}C for two hours to enhance the bonding between the two layers. This bonded structure having the optical waveguide and the lifting valves with the pneumatic chamber on top, is peeled off from the first master. Ports are punched to have access to the fluidic lines. Finally, after another step of plasma activation a 1:10 PDMS

substrate is bonded on the bottom of the structure which seals the fluidic lines, the pneumatic vales and act as the bottom cladding layer for the waveguides.

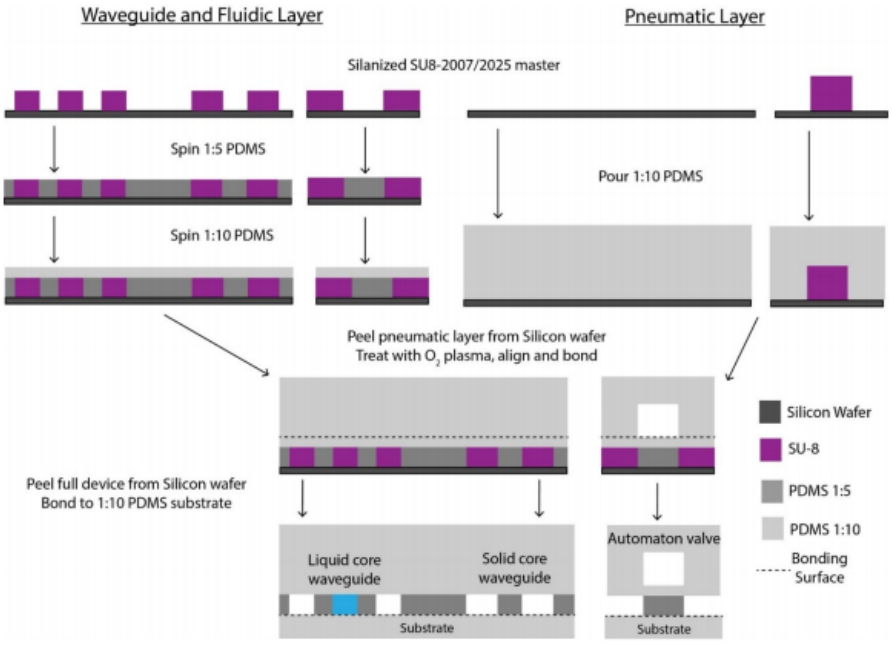


Fig 7.2 Schematic of the fabrication process of the PDMS chip.

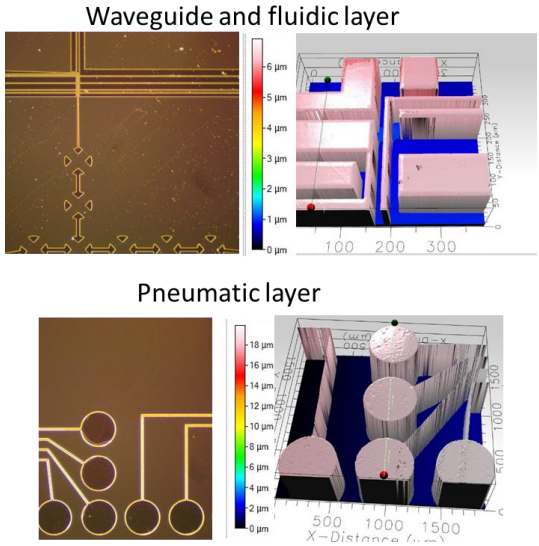


Fig 7.3 Top down optical image (left) and profilometric image (right) of the waveguide (top) and pneumatic layer (bottom)

Fig 7.4a shows the schematic of the device. Each valve (0.5 mm in diameter [W_V] and 18 – 20 µm thick [H_V]) in the sample preparation section is connected via 50 µm wide fluidic channels. The channel height is measured to be 5 - 7 µm throughout the device (Fig 7.3), yielding a valve volume of approximately 1.3 nL. The valves are opened and closed by applying negative or positive pressure respectively (Fig 7.4b). The liquid channel which connects the pneumatic valve "no 1" to the optical detection is tapered to minimize backflow. Fluid access was provided to the two separate channels by punching the ports as mentioned above at inlets 1, 2, and the outlet. The channels are brought together to meet at the center, for mixing and sample preparation, before being pumped to the optical section for detection. The liquid channel tapers down to 15 µm as it intersects with the solid-core optical waveguides. The optical waveguides are about 8 - 9 µm wide and has the same thickness as the fluid lines (5 – 7 µm). Fig 7.4c shows the image of the optical mode supported in the SC waveguide. The modes have a horizontal and vertical FWHM of 7 µm and 8 µm respectively. The thin pedestal on top of the SC waveguide makes the optical mode have higher vertical FWHM. After the intersection with the SC waveguide, the liquid channel expands again as it approaches the outlet.

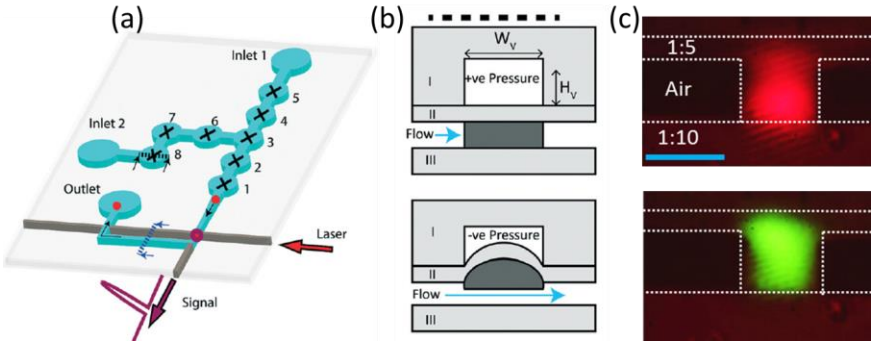


Fig 7.4 a) Schematic of the all in one PDMS chip. b) Cross section schematic of the pneumatic valves. c) Image of the optical modes supported by the SC PDMS waveguide when excited by 633 nm and 556 nm wavelengths (Scale bar: 7 µm)

7.2 Single nucleic acid detection

Here, the sensitivity and the optical limit of detection of the all in one PDMS chip is investigated by fluorescently tagging and detecting individual λ-DNA. Inlet-1 is filled with 1x concentration

of SYBR Gold intercalating dye (Thermofisher) and inlet-2 is filled with λ-DNA in 1x TE buffer. The intercalating dye becomes fluorescent upon binding with nucleic acids. The automaton is programmed to actuate the valves such that analytes from both inlets are brought to the intersecting center valve “no 3”. The fluids are then mixed by moving them between valves 3, 4 and 6. The mixed sample is incubated in the center valve for 2-3 mins. Multitudes of SYBR Gold intercalating dye tags each 40 kbp long λ-DNA during the incubation time, which makes them fluorescent. After incubation, the stained DNA is pumped to the optical detection part of the device. The SC waveguide is butt coupled with a fiber and excited by 488 nm argon laser. The micron scale dimensions of the waveguide create a sub-picolitter excitation volume in the LC channel. The fluorescence signal is detected off chip using an APD.

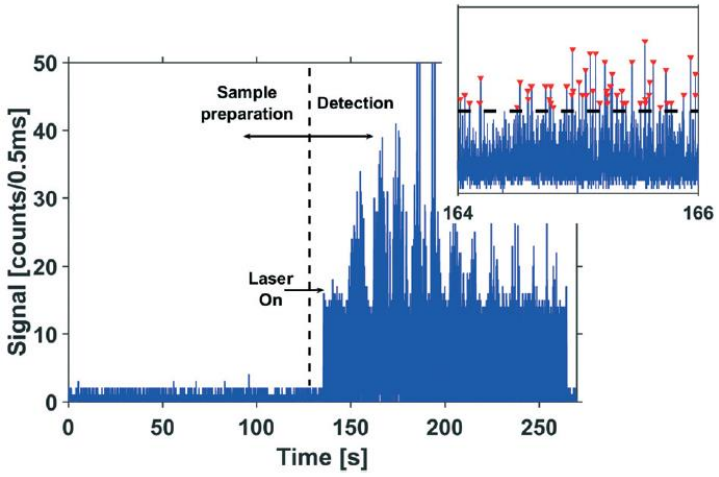


Fig 7.5 Fluorescence signal trace demonstrating detection of individual λ-DNA. First few minutes is used for tagging and incubating the DNA and then pumped to the detection part. The inset shows zoomed in, signals from individual λ-DNAs.

The automaton is programmed to repeat the mixing cycle followed by 10 times pumping the DNA–dye complex through the optical region. Fig 7.5 shows the fluorescence signal trace of one such complete sample preparation and detection cycle for a λ-DNA concentration of 25 pg/μL. The background threshold is determined by the highest photon count signal before the pumping of the tagged DNA starts, and individual peaks from single nucleic acids above this threshold are counted (Fig. 6.5 inset, each spike in photon count is a detected event). This

demonstrates single molecule detection sensitivity on this dual-purpose chip. In order to assess the detection limit, serial dilution of λ-DNA with concentration varying from 250 – 2.5 pg/µL (800 – 8 fM, which covers the concentrations of viral infectious diseases) was introduced in the inlet-2 and detected using the chip (Fig 7.6). Fig 7.6 shows the detected number of events per unit volume from samples of known concentrations. Assuming full length DNA, approximately 60% of the total DNA expected from the sample is detected. Since the concentrations of the targets are in the digital regime where individual DNA molecules are counted, the count rate scaled expectedly with the known concentrations. Here, the starting sample volume (~5 nL, determined by the size of a single microvalve) being pushed through the optical region dictates the detection limit rather than the sensitivity of the optical detection. At the lowest concentration of 2.5 pg/µL, the experiment which is performed in triplicates showed an average detection rate of 5 events/nL of sample flow as compared to a rate of one event per 100 nL of flow for a blank.

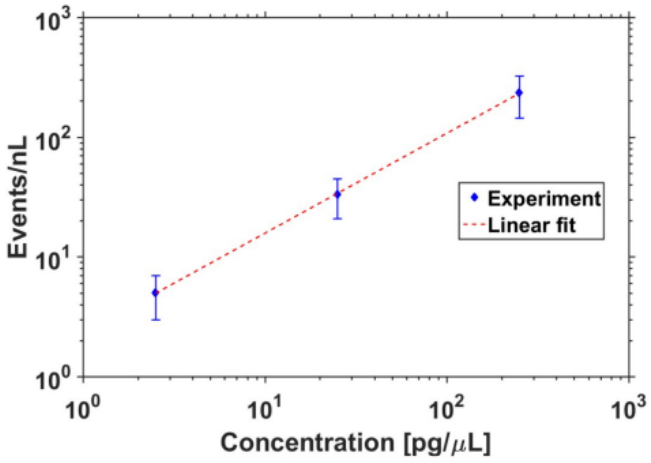


Fig 7.6 Dilution curve of the detected λ-DNA. For each know concentration of the sample, the detected number of events per unit volume is plotted.

7.3 Dual detection of ZIKV nucleic acid and protein

The chip is also used to demonstrate the preparation and detection of a dual target, nucleic acid and protein assay for ZIKV detection. The pneumatic valves can be programmed for dynamic sample preparation by performing tasks such as sample distribution, mixing, thermal

annealing, fluorescent labelling, and washing. Here a magnetic bead-based assay complex similar to the one described in chapter 3, is prepared completely on chip, immediately followed by optical detection. This process is compatible with both nucleic acids and proteins and is used to simultaneously capture and detect them from human serum.

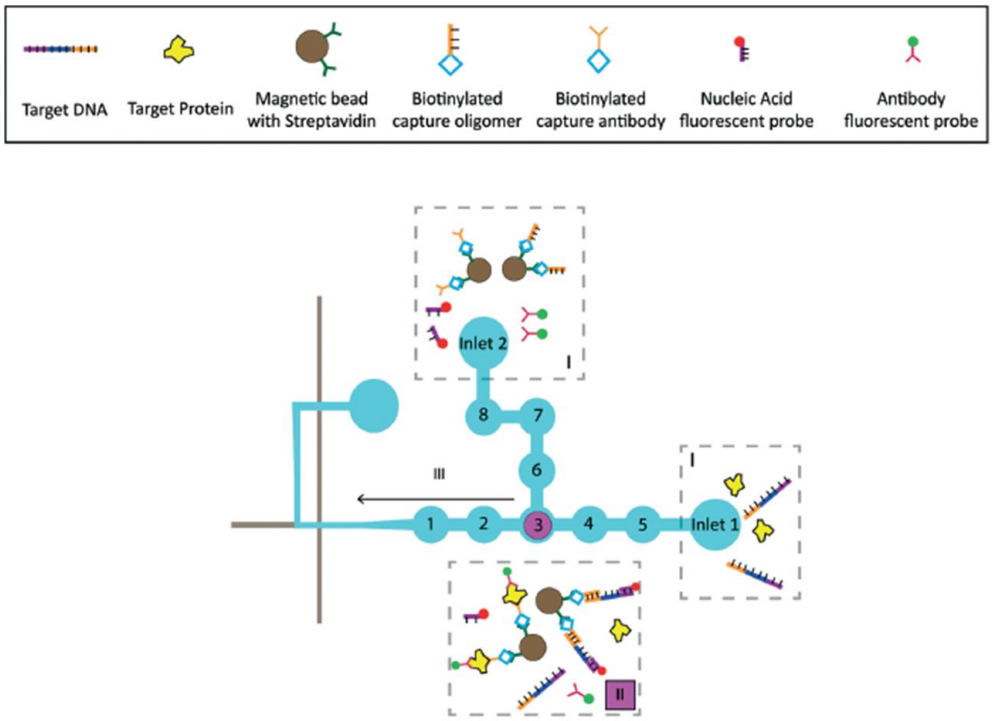


Fig 7.7 Schematic for preparation of magnetic bead-based assay. (I) Targets (nucleic acids and proteins) are introduced in Inlet 1 and the reagents such as the magnetic beads with capture probe and the fluorescent probes in inlet-2. (II) Analytes are mixed and incubated in valve “no 3”. (III) After wash steps, tagged targets are pumped for optical detection

Inlet-1 is used as the sample inlet and is filled with nucleic acids and proteins corresponding to ZIKV, spiked in human serum (Sigma-Aldrich) (Fig 7.7). A 100 base pair long single strand DNA oligomer corresponding to the capsid part of the Zika genome (KU321639.1, nt. 121-220) was chosen as the nucleic acid target for the experiments. For proteins, recombinant Zika NS1 antigen, obtained from East Coast Biologics Inc., is used as the target. 2 µL of DNA and 2 µL of protein targets were spiked in serum to yield an end concentration of 2 µM and 0.6 mg/mL of DNA and protein respectively. This is introduced in inlet-1 and is to be captured on magnetic

beads, fluorescently labelled and detected. Inlet-2 is used for the reagents. A mixture of magnetic capture beads ($2.5x10^8$ beads/mL) and nucleic acid and protein target specific fluorescent probes (2.5 µM and 0.25 mg/mL of nucleic acid and antibody fluorescent probes respectively) are introduced in the inlet-2 (Fig 7.7). A 25-mer oligonucleotide with an attached fluorophore (excitation: 633 nm), designed to be reverse complementary to a region of the above-mentioned target DNA (KU321639.1, nt. 187-211), is the target specific nucleic acid fluorescent probe. A 50-mer biotinylated oligonucleotide, designed to hybridize to a different part of the target sequence (KU321639.1, nt. 130-179), is used as the nucleic acid capture probe. Streptavidin coated magnetic beads (Thermofisher Scientific) were conjugated off chip with the biotinylated capture oligonucleotide and then introduced in inlet-2. Monoclonal antibodies specific to the Zika NS1 region were obtained from EastCoast Bio. One set of antibodies was labelled with the cyanine 3 (Cy-3) fluorophore (Lumiprobe, excitation: 556 nm) to act as the protein specific fluorescent probe. While another set of the antibodies was modified with biotin and subsequently conjugated with the magnetic beads in 1xPBS off chip and then introduced in inlet-2.

The device is programmed to do all the sample processing steps automatically. The valve arrays were used to bring the analytes from both the inlets and mix them, similar to the λ-DNA experiment. The mixed analytes where incubated at 40 ^{0}C for 5 min in valve “no 3”. The heating temperature is chosen to allow for uncoiling of the nucleic acids while also preventing the protein analytes from denaturing. After heating, the sample is cooled and incubated at room temperature for 45 min during which the nucleic acid and protein targets combine with the corresponding fluorescent probes and capture beads. During the incubation step, the inlets were washed and replaced with 1x PBS buffer. A magnet is kept below the chip to pull down the beads in the valve “no 3”. The human serum along with the unbound targets and probes were washed off by pumping the buffer from inlet-1 to inlet-2 leaving behind only the pulled down bead complexes in valve 3.

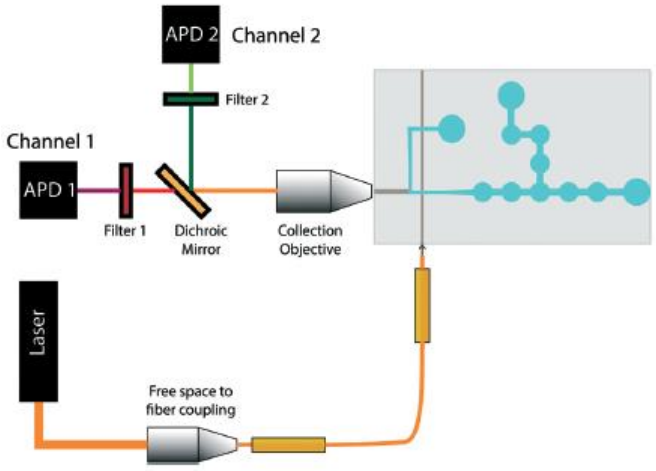


Fig 7.8 Schematic view of the optical set up for dual target detection. A dichroic mirror spectrally differentiates the signals from the nucleic acids and proteins and are couple to two APDs. The excitation light is blocked by optical filter kept in front of the APDs.

The magnet is removed from underneath the chip and the pulled down magnetic bead-based sample is resuspended by flutter mixing between valve no 3 and no 6. The assay is then pumped to the optical side of the chip. The PDMS waveguide is excited by both a He-Ne laser (633 nm) and solid-state laser (556 nm). The signal collected from the chip is spectrally decomposed off chip using a dichroic mirror and detected simultaneously by two synchronized APDs (Fig 7.8). The valves are programed to flush the analyte to the optical detection part 10 times to ensure that most of the beads pass through the excitation volume and are detected. Fig 7.9 shows the fluorescence traces obtained from the two APDs corresponding to nucleic acids (pink) and proteins (green), exhibiting fluorescence peaks form individual target containing beads. Both the nucleic acid and protein targets gave comparable signals with SNRs (defined as the ratio of average signal to the noise threshold for the particular target) of 2.8 and 2.5. A control with monovalent streptavidin and non-Zika specific nucleic acid targets (Zaire Ebola AY354458.1, nt. 6832-6931) at the same initial concentrations in serum gave no signal indicating the specificity of the assay (Fig 7.10).

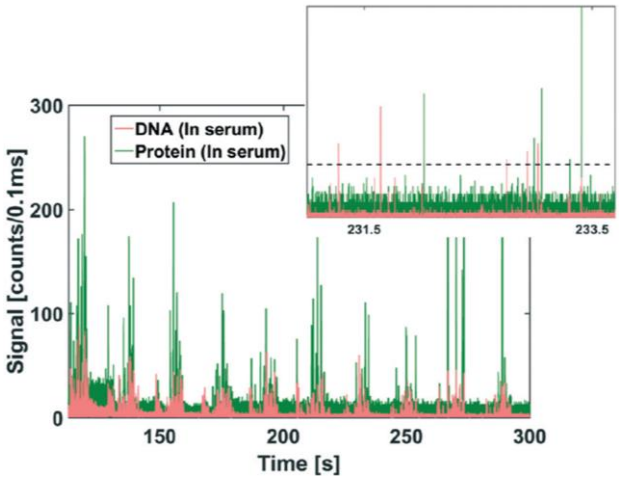


Fig 7.9 Fluorescence signal from magnetic beads with ZIKV nucleic acids (pink) and proteins (green) detected by the two APDs. Inset: Zoomed in 2 sec trace shows individual peaks above the set threshold. The protein signal trace had a higher noise threshold (shown in the inset as black dotted line) than the nucleic acid signals.

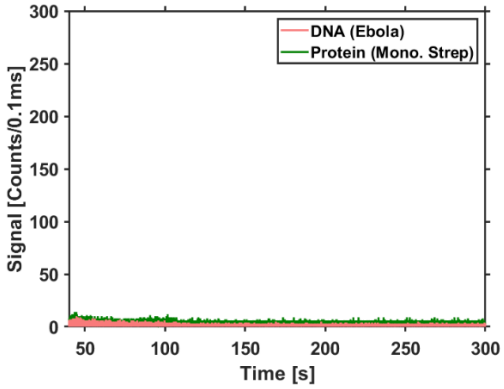


Fig 7.10 Fluorescence trace from the chip when using non-zika specific nucleic and protein targets in serum. The experiment yielded no signal indicating good specificity of the assay. The green excitation generally gave higher background than the red.

To determine the detection limits on nucleic acid and protein detection using bead-based assays, the above experiments where repeated with 100x lower dilution of the targets. Therefore, human serum spiked with 20 nM and 6 µg/mL of end concentration of nucleic acids and proteins respectively was used in inlet-1. The number of signals from the target reduced as expected. Fig 7.11 shows the histogram distribution of the peak heights of nucleic acid (top) and protein (bottom) assays obtained from the chip for the two concentrations. Each histogram is normalized by the total number of signals observed at the higher concentration of the

respective assays. The histogram shows that the signals from proteins have higher signal strength than nucleic acids. But both the targets have similar SNR due to the higher noise from the green excitation. Decreasing the concentration of the targets reduced the number of signals and the signal strength considerably. Given that the device is capable of detecting individual DNAs, this shows that the detection limit of the device is ultimately restricted by the type of assay used. Using lower concentration of targets limit the number of fluorophores attached to the magnetic bead. This could be addressed by labelling the targets with multiple fluorophores and then releasing them from the bead, thus detecting individual targets. For this purpose, specific labeling strategies like using single probes with multiple fluorophores attached such as Nanostrings (nCounter), quantum dots or fluorescent nanobeads described in chapter 5 can be implemented with this device for this purpose.

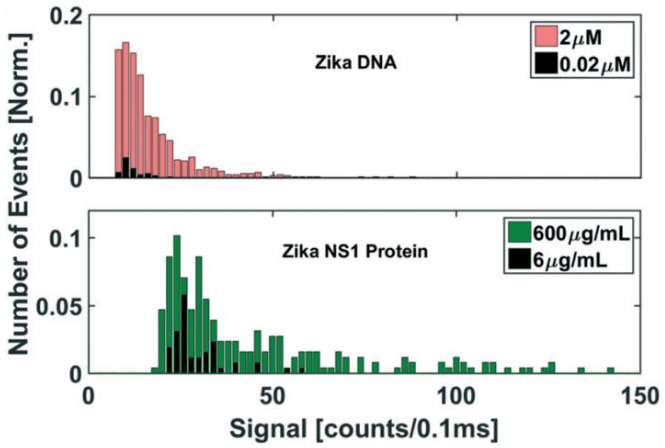


Fig 7.11 Distribution of signals from ZIKV specific nucleic acid (top) and protein (bottom) assays in human serum. Experiments for nucleic acids were done with 2 µM and 0.02 µM starting concentration and 600 µg/mL and 6 µg/mL for proteins.

7.4 Differential target detection

The ability to process and detect nucleic acids and proteins simultaneously can be employed for differential target detection. This advantage is demonstrated by differentiation of ZIKV from Dengue (DENV). The above described experiment is repeated with similar concentrations of non-Zika targets, especially Dengue. Fig 7.12 shows the normalized number of peaks detected

from nucleic acids and protein bead-based assays from each combination of target. The number of events is normalized by that observed when using Zika nucleic acid and protein targets. When Zika specific protein targets and non-Zika DNA targets were tested (Zair Ebola AY354458.1, nt. 6832-6931), the protein signal remained similar to that observed before but the DNA signal count reduced by more than two orders of magnitude compared to actual targets (Fig 7.12a & c). A similar observation is made when the wrong protein target (monovalent streptavidin) and the correct DNA target is used (Fig 7.12a & d). This shows that this system can be used to differentiate Zika targets from others. Finally, experiments are carried out with DENV targets (dengue NS1 protein and nucleic acids – KP188540.1, nt 186-281). Dengue NS1 proteins are known to have cross reactivity with corresponding zika antibodies [116]. As expected, a small but significant signal from the proteins is seen indicating a false positive. But due high specificity of the nucleic acid analytes to ZIKV, extremely low signals are seen from the DNA channel (0.02). This clearly indicates that the target under scrutiny is not zika specific.

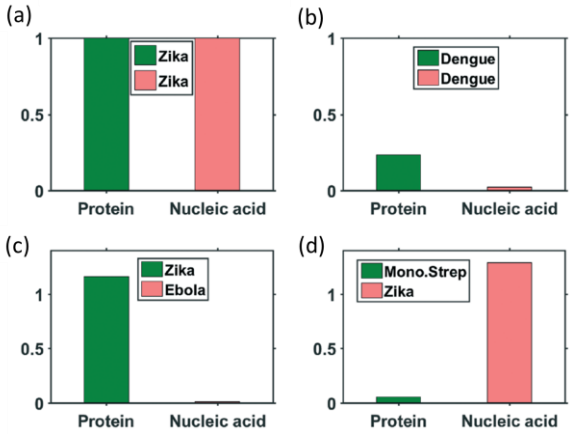


Fig 7.12 Target signal map for differential detection of Zika. The bar plots indicate the number of nucleic acid and protein signals for each target compared to that from zika specific targets.

Thus, processing and detecting the dual biomarker system in a single step using the PDMS device significantly reduces false positive identification of Zika targets due to cross reacting species such as dengue and allows successful diagnosis in a single platform. Monolithic

integration of optical ports into the sample preparation units enables to further expand the photonic capabilities of the device such as integrating on chip dye laser source [123] and multiplexed detection using MMI waveguides [122].

8 Conclusion

In conclusion, this work has produced four significant advances in the field of integrated biophotonics and optofluidics: improvement and optimization of the optical performance of ARROW waveguides, demonstration of multiplexed detection of biomolecules using spatial and spectral multiplexing, development of a new SiO_2 based biosensor architecture for enhanced fluorescence detection and development of an all PDMS based biosensor monolithically integrated with sample preparation system.

Protecting the ARROW biosensor using a buried low index oxide layer allowed the SC waveguides to support optical modes with 3x better confinement factor of 98% and narrow FWHM of 2.3 µm. This enabled better coupling of the optical mode with the LC channel and generate signals with 30x better SNR from fluorescent beads. By optimizing the length of the MMI waveguide for accounting to this change in the ARROW design, multi spot patterns with peak-to-valley ratios of 0.7 were generated in the LC channel.

The ARROW device with improved performance was used to demonstrate up to 7x multiplexed detection of nucleic acid targets. This was achieved by combining spectral multiplexing with combinatorial fluorescence labeling of the targets using three colors. An antibiotic resistance bacterial panel of three species and four mutations was chosen for this demonstration. This thesis also reported multiplexed detection with MMI waveguide using spatial multiplexing. An ARROW biosensor with three LCs excited by a single MMI waveguide was used to detect, without amplification, three antibiotic resistance plasmids simultaneously. Plasmids were detected with single molecule sensitivity by tagging them with multitudes of nucleic acid staining dye. Dual detection of SARS-CoV-2 RNA and antigen was demonstrated by combining spectral and spatial multiplexing. By using nucleic acid staining dye for RNA and a novel template DNA based bright fluorophore for the antigens, targets were sensed with single molecule sensitivity enabling amplification free detection. Thus, this research work has demonstrated the full power

of using multi-spot excitation of molecular biomarkers with MMI waveguides for multiplexed disease diagnostics.

A novel SiO_2 based biosensor following the same architecture as the ARROW biosensor chips but using index guided SC and LC waveguide for enhanced fluorescence detection was introduced in this thesis. The optical mode of the LC was optimized using high refractive index salt solution to detect fluorescent Nano-beads with 8x higher SNR and 45x increase in particle counts per unit volume reaching a low detection limit of 80 aM.

Finally, design and implementation of a PDMS based biosensor chip which combines sample preparation units with an in-flow optical detection was described. Pneumatically actuated microvalves were used to manipulate fluid flow for on chip preparation of biological fluorescence assays. PDMS based optical waveguides and LC channels were used for detection of the prepared targets. The device was used to fluorescently tag and detect λ-DNA with single molecule sensitivity with a detection limit of 8 fM. The sample preparation units are used to prepare a more complex magnetic bead-based assay for dual detection of ZIKV specific nucleic acids and proteins from from blood serum and their distinction cross reacting species like DENV.

9 Bibliography

1. World Health Organization: Values charter.
2. C. P. Price, BMJ **322**, 1285 (2001).
3. World Health Organization: Emergencies preparedness, response- Disease outbreaks by year.
4. D.Gu, N. Dong, Z. Zheng, D. Lin, M. Huang, L. Wang, E. W. C. Chan, L. Shu, J. Yu, R. Zhang and S. Chen, Lancet Infect. Dis. **18**, 37 (2018).
5. R. S. Singer, Lancet Infect. Dis. **3**, 47 (2003).
6. Vashist, S.K., Biosensors **7**, 62 (2017).
7. M. T. Osterholm, Science **353**, 1073 (2016).
8. G. Cuzon, C. Bentchouala, A. Vogel, M. Héry, A. Lezzar, F. Smati, L. Dortet and T. Naas, Int. J. Antimicrob. Agents **46**, 725 (2105).
9. C. Dincer, R. Bruch, A. Kling, P. S. Dittrich and G. A. Urban, Trends in Biotech. **35**, 728 (2017).
10. A. P. F. Turner, Chem. Soc. Rev. **42**, 3184 (2013).
11. X. Fan, Advanced photonic structures for biological and chemical detection, Springer (2009).
12. E. Luan, H. Shoman, D. M. Ratner, K. C. Cheung, and L.Chrostowski, Sensors **18**, 3519 (2018).
13. G. K. Geiss, R. E. Bumgarner, B. Birditt, T. Dahl, N. Dowidar, D. L. Dunaway, H. P. Fell, S. Ferree, R. D. George, T. Grogan, J. J. James, M. Maysuria, J. D. Mitton, P. Oliveri, J. L. Osborn, T. Peng, A. L. Ratcliffe, P. J. Webster, E. H. Davidson, L. Hood, and K. Dimitrov, Nat. Biotechnol. **26**, 317 (2008).
14. Y. Li, Y. Thi, H. Cu, and D. Luo, Nat. Biotechnol. **23**, 885 (2005).
15. N. Ganesh, W. Zhang, P. C. Mathias, E. Chow, J. A. N. T. Soares, V. Malyarchuk, A. D. Smith, and B. T. Cunningham, Nat. Nanotech. **2**, 515 (2007).

16. Y. Sun and X. Fan, Angew. Chemie Int. Ed. **51**, 1236 (2012).
17. M. T. Guo, A. Rotem, J. A. Heyman and D. A. Weitz, Lab Chip **12**, 2146 (2012).
18. K. J. Land, Paper-based diagnostics: Current status and future applications, Springer (2019).
19. R. Burger, L. Amato, and A. Boisen, Biosens. Bioelectron. **76**, 54 (2016).
20. J. Kim, M. Kang, E. C. Jensen and R. A. Mathies, Anal. Chem. **84**, 2067 (2012).
21. X. Fan and I. M. White, Nat. Photonics **5**, 591 (2011).
22. H. Schmidt and A. R. Hawkins, Nat.Photonics **5**, 598 (2011).
23. H. Schmidt and A. R. Hawkins, Microfluid. Nanofluidics **4**, 3 (2008).
24. H. Cai, J. W. Parks, T. A. Wall, M. A. Stott, A. Stambaugh, K. Alfson, A. Griffiths, R. A. Mathies, R.Carrion, J. L. Patterson, A. R. Hawkins, and H. Schmidt, Sci. Rep. **5**, 14494 (2015).
25. K. Du, H. Cai, M. Park, T. A. Wall, M. A. Stott, K. J. Alfson, A. Griffiths, R. Carrion, J. L. Patterson, A. R. Hawkins, H. Schmidt, and R. A. Mathies, Biosens. Bioelectron. **91**, 489 (2017).
26. D. Ozcelik, J. W. Parks, T. A. Wall, M. A. Stott, H. Cai, J. W. Parks, A. R. Hawkins, and H. Schmidt, Proc. Natl. Acad. Sci. U. S. A. **112**, 12933 (2015).
27. D. Ozcelik, A. Jain, A. Stambaugh, M. A. Stott, J. W. Parks, A. Hawkins, and H. Schmidt, Sci. Rep. **7**, 12199 (2017).
28. J. A. Black, V. Ganjalizadeh, J. W. Parks, and H. Schmidt, Optics Letters **43**, 4425 (2018).
29. H. Cai, M. A. Stott, D. Ozcelik, J. W. Parks, A. R. Hawkins, and H. Schmidt, Biomicrofluidics **10**, 064116 (2016).
30. R. Lowe, C. Barcellos, P. Brasil, O. G. Cruz, N. A. Honorio, H. Kuper and M. S. Carvalho, Int. J. Environ. Res. Public Health **15**, 96 (2018).
31. P. Yeh, Optical waves in layered media, Wiley (1998).

32. M. A. Duguay, Y. Kokubun, T. L. Koch and L. Pfeiffer, Appl. Phys. Lett. **49**, 13 (1986).

33. L. B. Soldano and E. C. M. Pennings, J. Light. Technol. **13**, 615 (1995).

34. A. R. Hawkins and H. Schmidt, Microfluidics and Nanofluidics **4**, 17 (2008).

35. J. W. Parks, T. A. Wall, H. Cai, A. R. Hawkins, H. Schmidt, IEEE JSTQE **22**, 4403106 (2016).

36. T. Wall, J. McMurray, G. G. Meena, V. Ganjalizadeh, H. Schmidt, A. R. Hawkins, Micromechines **8**, 252 (2017).

37. M. A. Stott, V. Ganjalizadeh, G. G. Meena, J. McMurray, M. Olsen, M. Orfila, H. Schmidt, A. R. Hawkins, IEEE PTL **30**, 1487 (2018).

38. M. A. Stott, V. Ganjalizadeh, M. H. Olsen, M. Orfila, J. McMurray, H. Schmidt, A. R. Hawkins, IEEE JQE **54**, 6200107 (2018).

39. C. Campos, J. Albiero, A. B. Ecker, C. M. Kuroda, L. E. F. Meirelles, A. Polato, M. C. B. Tognim, M. A. Wingeter and J. J. V. Teixeira, Am. J. Infect. Control **44**, 1374 (2016).

40. A. U. Khan, L. Maryam and R. Zarrilli, BMC Microbiol. **17**, 1 (2017).

41. L. Poirel and P. Nordmann, Clin. Microbiol. Infect. **12**, 826 (2006.

42. Antibiotic Resistance Threats in the United States, CDC, 2019.

43. G. G. Meena, T. A. Wall, M. A. Stott, O. Brown, R. Robison, A. R. Hawkins and H. Schmidt, Optics express (2020)

44. Y. Zheng, R. Fan, C. Qiu, Z. Liu, and D. Tian, Int. J. Mass Spectrom. **409**, 53 (2016).

45. P. Du, W. A. Kibbe, and S. M. Lin, Bioinformatics **22**, 2059 (2006).

46. CLSI, Performance Standards for Antimicrobial Susceptibility Testing, Clinical and Laboratory Standards Institute, 2020.

47. CDC, Detection of Enterobacteriaceae Isolates Carrying Metallo-Beta-Lactamase- United States, 59, 750 (2010).

48. J. H. Jorgensen and J. D. Turnidge, Manual of Clinical Microbiology, American Society of Microbiology, 11th edition, 1253 (2015).

49. J. Hudzicki, American Society for Microbiology, (2009)

50. A. Amjad, I. A. Mirza, S. A. Abbasi, U. Farwa, N. Malik and F. Zia, Iran. J. Microbiol. 3, 189 (2011).
51. F. Pasteran, L. J. Gonzalez, E. Albornoz, G. Bahr, A.J. Vila, A. Corso, Journal of Clinical Microbiology 54, 640 (2016).
52. P. Nordmann, M. Gniadkowski, C. G. Giske, L. Poirel, N. Woodford, V. Miriagou, M. Akova, T. Naas, H. Seifert, D. Livermore, P. Bogaerts, Y. Glupczynski, R. Canton, G. M. Rossolini, A. Adler, Y. Carmeli, S. Navon-Venezia, O. Samuelsen and G. Cornaglia, Clin. Microbiol. Infect. 18, 432 (2012).
53. H. Dickert, K. Machka and I. Braveny, Infection 9, 18 (1981).
54. C. G. Carvalhaes, R. C. Picão, A.G. Nicoletti, D. E. Xavier, A. C. Gales, Journal of Antimicrobial Chemotherapy 65, 249 (2010).
55. I. E. Robledo, E. E. Aquino and G. J. Vázquez, Antimicrob. Agents Chemother. 55, 2968 (2011).
56. A. Raghunathan, L. Samuel and R. J. Tibbetts, Am. J. Clin. Pathol. 135, 566 (2011).
57. K. A. Bauer, K. K. Perez, G. N. Forrest and D. A. Goff, Clin. Infect. Dis. 59, S134 (2014).
58. S. Y. Teh, R. Lin, L. H. Hung and A. P. Lee, Lab Chip 8, 198 (2008).
59. J. Kim, E. C. Jensen, A. M. Stockton and R. A. Mathies, Anal. Chem. 85, 7682 (2013).
60. W. G. Pitt, M. Alizadeh, G. A. Husseini, D. S. McClellan, C. M. Buchanan, C. G. Bledsoe, R. A. Robison, R. Blanco, B. L. Roeder, M. Melville and A. K. Hunter, Biotechnol. Prog. 32, 823 (2016).
61. W. G. Pitt, M. Alizadeh, R. Blanco, A. K. Hunter, C. G. Bledsoe, D. S. McClellan, M. E. Wood, R. L. Wood, T. V. Ravsten, C. L. Hickey, W. Cameron Beard, J. R. Stepan, A. Carter, G. A. Husseini, R. A. Robison, E. Welling, R. N. Torgesen and C. M. Anderson, Biotechnol. Prog. 36, e2892 (2020).

62. R. Knob, R. L. Hanson, O. B. Tateoka, R. L. Wood, I. Guerrero-Arguero, R. A. Robison, W. G. Pitt and A. T. Woolley, J. Chromatogr. A 1562, 12 (2018).
63. R. Knob, D. B. Nelson, R. A. Robison and A. T. Woolley, J. Chromatogr. A 1523, 309 (2017).
64. D. Ozcelik, A. Jain, A. Stambaugh, M. A. Stott, J. W. Parks, A. Hawkins and H. Schmidt, Sci. Rep. 7, 12199 (2017).
65. G. G. Meena, R. L. Hanson, R. L. Wood, O. T. Brown, M. A. Stott, R. A. Robison, W. G. Pitt, A. T. Woolley, A. R. Hawkins and H. Schmidt, Lab Chip 20, 3763 (2020).
66. E. Petersen, M. Koopmans, U. Go, D. H. Hamer, N. Petrosillo, F. Castelli, M. Storgaard, S. A. Khalili and L. Simonsen, Lancet Infect. Dis. 20, e238 (2020).
67. W. Yang, S. Kandula, M. Huynh, S. K. Greene, G. V. Wye, W. Li, H. T. Chan, E. McGibbon, A. Yeung, D. Olson, A. Fine and J. Shaman, Lancet Infect. Dis. (2020)
68. J. Anneser, Palliat. Support. Care 18, 382 (2020).
69. E. Dong, H. Du and L. Gardner, Lancet Infect. Dis. 20, 533 (2020).
70. N. C. Grassly, M. P. Salort, E. P. K. Parker, P. J. White and N. M. Ferguson, Lancet Infect. Dis. (2020).
71. I. Astuti and Ysrafil, Diabetes Metab. Syndr. Clin. Res. Rev. 14, 407 (2020).
72. M. Touma, Journal of Molecular Medicine 98, 947 (2020).
73. B. Udugama, P. Kadhiresan, H. N. Kozlowski, A. Malekjahani, M. Osborne, V. Y. C. Li, H. Chen, S. Mubareka, J. B. Gubbay, and W. C. W. Chan, ACS nano 14, 3822 (2020).
74. B. J. Tromberg, T. A. Schwetz, E. J. Pérez-Stable, R. J. Hodes, R. P. Woychik, R. A. Bright, R. L. Fleurence, and F. S. Collins, N. Engl. J. Med. 383, 1071 (2020).
75. N. Ravi, D. L. Cortade, E. Ng, and S. X. Wang, Biosens. Bioelectron. 165, 112454 (2020).
76. P. I. Kontou, G. G. Braliou, N. L. Dimou, G. Nikolopoulos, and P. G. Bagos, Diagnostics 10, 319 (2020).

77. Y. Hirotsu, M. Maejima, M. Shibusawa, Y. Nagakubo, K. Hosaka, K. Amemiya, H. Sueki, M. Hayakawa, H. Mochizuki, T. Tsutsui, Y. Kakizaki, Y. Miyashita, S. Yagi, S. Kojima, and M. Omatad, Int. J. Infect. Dis. 99, 397 (2020).
78. L. Liu, W. Liu, Y. Zheng, X. Jiang, G. Kou, J. Ding, Q. Wang, Q. Huang, Y. Ding, W. Ni, W. Wu, S. Tang, L. Tan, Z. Hu, W. Xu, Y. Zhang, B. Zhang, Z. Tang, X. Zhang, H. Li, Z. Rao, H. Jiang, X. Ren, S. Wang, S. Zheng, Microbes Infect. 22, 206 (2020).
79. M. L. Bastos, G. Tavaziva, S. K. Abidi, J. R Campbell, L. P. Haraoui, J. C. Johnston, Z. Lan, S. Law, E. MacLean, A. Trajman, D. Menzies, A. Benedetti, and F. A. Khan, BMJ 370, 2516 (2020).
80. B. Fung, A. Gopez, V. Servellita, S. Arevalo, C. Ho, A. Deucher, E. Thornborrow, C. Chiu and S. Miller, JCM 58, e01535 (2020).
81. Q. X. Long et al., Nat. Med. 26, 845 (2020).
82. R. Wölfel, V. M. Corman, W. Guggemos, M. Seilmaier, S. Zange, M. A. Müller, D. Niemeyer, T. C. Jones, P. Vollmar, C. Rothe, M. Hoelscher, T. Bleicker, S. Brünink, J. Schneider, R. Ehmann, K. Zwirglmaier, C. Drosten and C. Wendtner, Nature 581, 465 (2020).
83. A. P. Espejo, Y. Akgun, A. F. A. Mana, Y. Tjendra, N. C. Millan, C. G. Fernandez, and C. Cray, American journal of clinical pathology 154, 293 (2020).
84. P. Wang, J. Virol. Methods 283, 113919 (2020).
85. T. Kilic, R. Weissleder, and H. Lee, iScience 23, 101406 (2020).
86. M. M. Gibani et. al., The Lancet Microbe 1, e300 (2020).
87. A. Basu, T. Zinger, K. Inglima, K. Woo, O. Atie, L. Yurasits, B. See, M. E. A. Rosenfeld, J. Clin. Microbiol. 58, e01136 (2020).
88. G. Seo, G. Lee, M. J. Kim, S. H. Baek, M. Choi, K. B. Ku, C. S. Lee, S. Jun, D. Park, H. G. Kim, S. J. Kim, J. Lee, B. T. Kim, E. C. Park and S. Kim, ACS Nano 14, 5135 (2020).

89. M. Wang, A. Fu, B. Hu, Y. Tong, R. Liu, Z. Liu, J. Gu, B. Xiang, J. Liu, W. Jiang, G. Shen, W. D. Men, Z. Deng, L. Yu, W. Wei, Y. Li, T. Liu, Small 16, 2002169 (2020).
90. G. Qiu, Z. Gai, Y. Tao, J. Schmitt, G. A. Kullak-Ublick, and J. Wang, ACS Nano 14, 5268 (2020).
91. Z. Chen, Z. Zhang, X. Zhai, Y. Li, L. Lin, H. Zhao, L. Bian, P. Li, L. Yu, Y. Wu and G. Lin, Anal. Chem. 92, 7226 (2020).
92. Z. Li, Y. Yi, X. Luo, N. Xiong, Y. Liu, S. Li, R. Sun, Y. Wang, B. Hu, W. Chen, Y. Zhang, J. Wang, B. Huang, Y. Lin, J. Yang, W. Cai, X. Wang, J. Cheng, Z. Chen, K. Sun, W. Pan, Z. Zhan, L. Chen, F. Ye, J. Med. Virol. 92, 1518 (2020).
93. M. Rahman, M. Harrington, M. A. Stott, Y. Li, M. J. N. Sampad, T. D. Yuzvinsky, A. R. Hawkins, and H. Schmidt, Optica 6, 1130 (2019).
94. M. B. Duchamp, J. S. Casalegno, Y. Gillet, E. Frobert, E. Bernard, V. Escuret, G. Billaud, M. Valette, E. Javouhey, B. Lina, D. Floret and F. Morfin, Clinical Microbiology and Infection 16, 317 (2010).
95. R. Wölfel, V. M. Corman, W. Guggemos, M. Seilmaier, S. Zange, M. A. Müller, D. Niemeyer, T. C. Jones, P. Vollmar, C. Rothe, M. Hoelscher, T. Bleicker, S. Brünink, J. Schneider, R. Ehmann, K. Zwirglmaier, C. Drosten and C Wendtner, Nature 581, 465 (2020).
96. M. A. Duguay, Y. Kokubun and T. L. Koch, Applied Physics Letters 49, 13 (1986).
97. E. S. Hamilton, V. Ganjalizadeh, J. G. Wright, H. Schmidt and A. R. Hawkins, Micromachines 11, 349 (2020).
98. E. S. Hamilton, V. Ganjalizadeh, J. G. Wright, W. G. Pitt, H. Schmidt and A. R. Hawkins, Microfluidics and Nanofluidics 23, 122 (2019).
99. S. Seki, S. Tsuzuki, K. Hayamizu, Y. Umebayashi, N. Serizawa, K. Takei, and H. Miyashiro, J. Chem. Eng. Data 57, 2211 (2012).

100. N. Muhammad, M. I. Hossain, Z. Man, M. El-Harbawi, M. A. Bustam, Y. A. Noaman, N. B. Mohamed Alitheen, M. K. Ng, G. Hefter, and C. Y. Yin, J. Chem. Eng. Data 57, 2191 (2012).

101. R. Vijayaraghavan, A. Izgorodin, V. Ganesh, M. Surianarayanan, and D. R. MacFarlane, Angew. Chemie - Int. Ed. 49, 1631 (2010).

102. R. Alcalde, G. García, M. Atilhan, and S. Aparicio, Ind. Eng. Chem. Res. 54, 10918 (2015).

103. A. J. L. Costa, M. R. C. Soromenho, K. Shimizu, I. M. Marrucho, J. M. S. S. Esperança, J. N. C. Lopes, and L. P. N. Rebelo, ChemPhysChem 13, 1902 (2012).

104. M. E. Graham, B. I. Davis, and D. V. Keller, Appl. Opt. 4, 613 (1965).

105. R. H. French, V. Liberman, H. V. Tran, J. Feldman, D. J. Adelman, R. C. Wheland, W. Qiu, S. J. McLain, O. Nagao, M. Kaku, M. Mocella, M. K. Yang, M. F. Lemon, L. Brubaker, A. L. Shoe, B. Fones, B. E. Fischel, K. Krohn, D. Hardy, and C. Y. Chen, SPIE Optical Microlithography XX 6520, 65201 (2007).

106. G. G. A. Ivan D. Zaytsev, Properties of Aqueous Solutions of Electrolytes (CRC, 1992).

107. F. Hendriks and A. Aviram, Rev. Sci. Instrum. 53, 75 (1982).

108. K. Bai and J. Katz, Exp. Fluids 55, 1 (2014).

109. G. G. Meena, J. W. Wright, A. R. Hawkins, H. Schmidt, JSTQE, (2021).

110. L. E. Page, X. Zhang, C. M. Tyrakowski, C. T. Ho, and P. T. Snee, Analyst 141, 6251 (2016).

111. N. Melnychuk and A. S. Klymchenko, J. Am. Chem. Soc. 140, 10856 (2018)

112. M. Bao, E. Jensen, Y. Chang, G. Korensky, and K. Du, ACS Appl. Mater. Interfaces 12, 43435 (2020).

113. M. C. Brunner, C. A. Chambers, F. K. Chan, J. Hanke, A. Winoto and J. P. Allison, J. Immunol. 162, 5813 (1999).

114. W. Feng, A. M. Newbigging, C. Le, B. Pang, H. Peng, Y. Cao, J. Wu, G. Abbas, J. Song, D. B. Wang, M. Cui, J. Tao, D. L. Tyrrell, X. E. Zhang, H. Zhang, and X. C. Le, Anal. Chem. 92, 10196 (2020).

115. M. T. Osterholm, Science 353, 1073 (2016).

116. L. Priyamvada, W. Hudson, R. Ahmed and J. Wrammert, Emerging Microbes and Infections 6, e33 (2017).

117. I. B. Rabe, J. E. Staples, J. Villanueva, K. B. Hummel, J. A. Johnson, L. Rose, S. Hills, A. Wasley, M. Fischer and A. M. Powers, Morbidity and Mortality Weekly Report 65, 543 (2016).

118. K. Pabbaraju, S. Wong, K. Gill, K. Fonseca, G. A. Tipples and R. Tellier, J. Clin. Virol. 83, 66 (2016).

119. S. M. Prakadan, A. K. Shalek and D. A. Weitz, Nat. Rev. Genet., 18, 345 (2017).

120. J. Kim, M. Kang, E. C. Jensen and R. A. Mathies, Anal. Chem. 84, 2067 (2012).

121. J. W. Parks, M. A. Olson, J. Kim, D. Ozcelik, H. Cai, R. Carrion, J. L. Patterson, R. A. Mathies, A. R. Hawkins and H. Schmidt, Biomicrofluidics 8, 054111(2014).

122. J.W. Parks and H. Schmidt, Scientific Reports 6, 33008 (2016).

123. T. Sano, J. Black, S. Mitchell, H. Zhang, and H. Schmidt, Optics Letters 45, 5978 (2020).